

8-30-2011

Novel approaches to power scaling of single-frequency photonic crystal fiber amplifiers

Craig Robin

Follow this and additional works at: https://digitalrepository.unm.edu/ose_etds

Recommended Citation

Robin, Craig. "Novel approaches to power scaling of single-frequency photonic crystal fiber amplifiers." (2011).
https://digitalrepository.unm.edu/ose_etds/37

This Dissertation is brought to you for free and open access by the Engineering ETDs at UNM Digital Repository. It has been accepted for inclusion in Optical Science and Engineering ETDs by an authorized administrator of UNM Digital Repository. For more information, please contact disc@unm.edu.

Craig Andrew Robin

Candidate

Electrical and Computer Engineering

Department

This dissertation is approved, and it is acceptable in quality and form for publication:

Approved by the Dissertation Committee:

Dr. Luke Lester, Chairperson

Dr. Mansoor Sheik-Bahae

Dr. Jean-Claude Diels

Dr. Iyad Dajani

**NOVEL APPROACHES TO POWER SCALING OF SINGLE-
FREQUENCY PHOTONIC CRYSTAL FIBER AMPLIFIERS**

BY

CRAIG ANDREW ROBIN

B.S., Physics, Pacific University, 2003

M.S., Optical Sciences and Engineering, University of New Mexico, 2009

DISSERTATION

Submitted in Partial Fulfillment of the
Requirements for the Degree of

**Doctor of Philosophy
Optical Sciences and Engineering**

The University of New Mexico
Albuquerque, New Mexico

July, 2011

©2011, Craig Andrew Robin

DEDICATION

I dedicate this dissertation to my family; those who are with me now and those who have passed away. The work presented here is not only the culmination of work in my graduate career, but also representative of the opportunities they have afforded me.

To my parents, you are responsible for the drive and work ethic which has made me successful. I cannot express how grateful I am for the sacrifices you have made, without which, this achievement would not have been possible. Thank you. I love you.

ACKNOWLEDGMENTS

I would first recognize Dr. Iyad Dajani, my advisor, mentor, and friend. The personal interest and dedication you have demonstrated for my academic and professional career was neither required nor opportune. I would not be writing this acknowledgement if it were not for your efforts at every stage of this process. You have been a positive influence on my growth as a scientist and as a person. For this, you have my sincerest gratitude and respect.

I also thank my committee members, Dr. Luke Lester, Dr. Mansoor Sheik-Bahae, Dr. Jean-Claude Diels, for their time and advisement throughout my graduate career.

I thank all levels of management at the Air Force Research Laboratory, for creating an environment where I could pursue my academic goals while being gainfully employed. Additionally, I would like to thank the High Energy Laser Joint Technology Office and Air Force Office of Scientific Research for funding the work presented here. I also thank the following people for their contributions: Clint Zeringue, Chris Vergien, Art Lucero, Tim Newell, Ben Ward, Furqan Chiragh, Ben Pulford, Dane Hult, Ken Rowland Jr. Your expertise/friendship/creativity made the completion of this milestone possible.

Finally, to my love, Jenny: You entered into this deal in the concluding, but most difficult years. For this I am fortunate, as it has given me the opportunity to see what an amazing person you are. Your patience, encouragement, and love have and continue to make all the difference in my life.

NOVEL APPROACHES TO POWER SCALING OF SINGLE-FREQUENCY PHOTONIC CRYSTAL FIBER AMPLIFIERS

BY

CRAIG ANDREW ROBIN

ABSTRACT OF DISSERTATION

Submitted in Partial Fulfillment of the
Requirements for the Degree of

**Doctor of Philosophy
Optical Sciences and Engineering**

The University of New Mexico
Albuquerque, New Mexico

July, 2011

NOVEL APPROACHES TO POWER SCALING OF SINGLE-FREQUENCY PHOTONIC CRYSTAL FIBER AMPLIFIERS

by

Craig Andrew Robin

B.S., Physics, Pacific University, 2003

M.S., Optical Sciences and Engineering, University of New Mexico, 2009

Ph.D., Optical Sciences and Engineering, University of New Mexico, 2011

ABSTRACT

This dissertation presents experimental and theoretical studies of high power, single-frequency, ytterbium-doped photonic crystal fiber amplifiers. The objective of this effort is to identify issues which limit power scaling and develop novel techniques to overcome these limitations. Historically, stimulated Brillouin scattering (SBS) has been the primary obstacle in the realization of high power single-frequency fiber amplifiers. A novel acoustically tailored photonic crystal fiber design, having a reduced Brillouin gain coefficient of 1.2×10^{-11} m/W, is demonstrated. The fiber design is such that it may be used in conjunction with other SBS mitigation techniques, which increases the nonlinear threshold beyond the current state of the art. In the successful suppression of SBS, a new regime of single-frequency photonic crystal fiber amplifier power scaling is explored. Instabilities in the transverse mode is observed at increasing output powers. Mitigation of this effect is demonstrated experimentally. This empirical data is used as the basis for a theoretical treatment of the problem, which provides direction for future fiber amplifier designs. The culmination of this work results in the successful utilization of the acoustically tailored photonic crystal fiber in a single-frequency counter-pumped amplifier configuration, yielding close to 500 W output power and near diffraction-limited beam quality.

TABLE OF CONTENTS

LIST OF FIGURES	xi
LIST OF TABLES	xviii
CHAPTER 1	1
Introduction.....	1
1.1. Scope of Work	1
1.2. Background.....	2
1.3. Advances in Fiber Amplifier Technology	4
1.3.1. Polarization Maintaining Fiber.....	4
1.3.2. Double Clad Fiber	6
1.3.3. Diode Pumping.....	7
1.4. Early Development of the Yb-doped Fiber Amplifier	9
1.4.1. Power Scaling in Er-Doped Fibers.....	10
1.4.2. Yb ³⁺ Spectroscopy.....	13
1.4.3. Photodarkening.....	16
1.5. Single-Frequency Fiber Amplifier Power Scaling.....	20
1.5.1. Single-Frequency YDFA: Initial Demonstrations.....	20
1.6. Stimulated Brillouin Scattering Mitigation Techniques	22
1.6.1. Linewidth Broadening.....	25
1.6.2. Fiber Geometry	26
1.6.3. Temperature and Stress/Strain Gradients.....	29
1.6.4. Laser Gain Competition	31
1.6.5. Acoustically Tailored Fibers	33

1.7. Single-Frequency YDFA's: State of the Art.....	36
1.8. Summary of the Work.....	38
CHAPTER 2	39
Numerical Modeling for Single-Frequency Yb-Doped Fiber Amplifiers	39
2.1. Overview.....	39
2.2. Stimulated Brillouin Scattering.....	40
2.3. Numerical Modeling of Single-Frequency YDFA's.....	42
CHAPTER 3	55
Experimental Results and Analysis	55
3.1. Photonic Crystal Fiber	55
3.2. Fiber Processing.....	60
3.2.1. Fiber Cleaving.....	60
3.2.2. Fiber Polishing	61
3.2.3. Endcapping.....	61
3.3. PCF Amplifier Construction.....	63
3.3.1. Seed Amplifier	64
3.3.2. High Power 976 nm Diode Pump and Characterization	66
3.3.3. Free Space Photonic Crystal Fiber Amplifier Setup	69
3.3.4. Measurement Notes.....	70
3.4. PCF Amplifier Power Scaling	75
3.4.1. Single Frequency Power Scaling: First Result.....	76
3.4.2. Narrow Linewidth PCF Amplifier	81
3.5. Segmented Acoustically Tailored Fiber.....	87
3.5.1. SAT Doping Configuration.....	90
3.6. Brillouin Gain Spectrum Measurement	94
3.6.1. Pump-Probe Experimental Setup.....	96

3.6.2.	Brillouin Gain Spectrum: Experimental Results	99
3.6.3.	Weakly Guided Acoustic Mode Analysis	108
3.7.	SAT and Reference PCF Single-Frequency Fiber Amplifier	120
3.7.1.	Power Dependent Modal Instabilities	148
3.7.2.	Transverse Mode Hopping: Thermal Dependence.....	150
CHAPTER 4	155
Conclusion	155
4.1.	Summary of Results	155
4.2.	Future Work	156
REFERENCES	159

LIST OF FIGURES

Figure 1: End view of a PANDA fiber. The two dark circles are stress applying parts provide birefringence in one axis of the core. The core is centrally located between the stress applying parts.	5
Figure 2: Double-clad fiber where core is designed to guide signal light and cladding is designed to guide pump light. A polymer coating is used to protect the fiber.	7
Figure 3: Energy-transfer up-conversion between two Er^{3+} -ions. Transitions labeled (2,4a) represent non-radiative transitions. All other arrows represent radiative transitions.[24].	12
Figure 4: The Yb^{3+} energy level structure, consisting of two manifolds. Approximate energies in wavenumbers above ground energy are indicated. Label A indicates the characteristic pump wavelength. Label B indicates characteristic signal wavelength. Label C indicates characteristic peak amplified spontaneous emission for signal wavelength choice of 1064 nm.	14
Figure 5: Absorption (solid) and emission (dotted) cross sections of Yb-doped germanosilicate glass.[31].	15
Figure 6: The non-planar ring resonator design. Polarization selection takes place at A. Points B,C, and D, total internal reflection occurs. A magnetic field H is applied to establish unidirectional oscillation. The diode pump enters the crystal at A.[59].	21
Figure 7: Single-Frequency master oscillator power amplifier (MOPA), pumped by a fiber coupled diode laser at 976 nm. DM is a dichroic mirror used to separate 1064 nm signal light and 976 nm pump light.[60]	22
Figure 8: Stimulated Brillouin scattering. Input light at ω_L is scattered by refractive index variations (shown by modulated shading in background) associated with sound wave at Ω_B . The reflected Stokes light, ω_S , is frequency downshifted by Ω_B	23
Figure 9: (red) Co-pumping power evolution in the fiber exhibiting increased effective length (L_{eff}). (blue) Power evolution in a counter pumped fiber amplifier. A rapid increase in power near the end of the fiber results in smaller effective length (L_{eff}).	29
Figure 10: (red) The thermal gradient due to quantum defect heating associated with co-pumping configuration. (blue) The thermal gradient due to quantum defect heating associated with counter-pumping configuration.	30

Figure 11: (green) A broadband 1040nm seed is co-propagated with a (blue) single-frequency 1064 nm seed. The amplifier is co-pumped with a 976nm multi-mode (MM) diode. The 1040nm experiences gain from the 976nm pump, and then begins pumping the 1064nm single-frequency seed. (red) The output of a single-frequency co-pumped amplifier.[76].....	32
Figure 12: (left) The acoustic delta profile when the concentration of Al ₂ O ₃ is linearly ramped down from the center of the core to the edge of the core. (right) The schematic of a double clad fiber with Yb, Ge, and Al co-doped in the core.[82]	34
Figure 13: Microscope end-face view of various areas in large mode area (LMA) photonic crystal fiber. (left) The fused silica strut bridge defining the air clad used for guiding pump light. (center) Pump cladding dimensions range from 300-500μm. (right) Geometry of the Yb-doped core, stress applying parts, and air hole lattice used to guide the signal mode.	56
Figure 14: Modified chemical vapor deposition (MCVD) process, before the preform is collapsed. The term other dopants refers to index lower or raising dopants such as germanium, aluminum, and fluorine. The combination of gasses is heated, resulting in a chemical reaction which deposits the desired materials on the inside of the tube.....	58
Figure 15: Stack and draw process used for photonic crystal fiber construction.	59
Figure 16: (left) Thermally collapsed PCF. The clear section in the center has been collapsed by heating the fiber to the fused silica softening temperature. Sections on the right and left are un-collapsed regions, which were not subject to significant heat. (right) PCF with 560 μm diameter endcapped with 1.3mm pure fused silica.....	62
Figure 17: (top) Three stage MOPA configuration showing the progression of power amplification. (bottom) The final stage of amplification highlighting the relevant components used in monolithic amplifiers. The hot/cold spool imposes a step thermal gradient for SBS suppression.	64
Figure 18: Final stage amplifier of the seed system with ~30W of output power.....	66
Figure 19: Wavelength characterization of Laserline diode pump. The wavelength stabilization setting fixes center wavelength near the peak absorption for Yb-doped fiber. The FWHM is approximately the same size as the 976 nm absorption bandwidth of Yb-doped silica.....	67
Figure 20: Output power of Laserline diode laser as function of drive voltage.	68
Figure 21: Experimental setup for counter-pumped PCF amplifier.	69
Figure 22: Transmitted signal in a passive fiber measured beyond the stimulated Brillouin scattering threshold. A single-frequency laser is coupled to a	

single-mode. The coupled laser power is pushed well beyond the SBS threshold.[96].....	72
Figure 23: Reflectivity vs. signal output power for fiber amplifier near SBS threshold. The departure from linear increase in backward power occurs in a very narrow window of output power.....	74
Figure 24: Optical spectrum analyzer (OSA) data measured from backward traveling light of single-frequency fiber amplifier at three output power levels (65W, 115 W, 125 W). The OSA resolution limit is ~1GHz, the separation between the SBS and Rayleigh peaks is approximately 16 GHz (0.06nm).	75
Figure 25: Single-frequency PCF amplifier with output of 260 watts showing slope efficiency of 74%.....	78
Figure 26: Beam profile and measured M^2 value at 200 W output power.	78
Figure 27: Experimental set-up for optical heterodyne analysis.[89].....	79
Figure 28: Optical heterodyne power spectrum for a signal output power of 32 W.[89]	80
Figure 29: Photonic crystal fiber (PCF) amplifier output power with phase modulated, narrow linewidth seed.	82
Figure 30: Photonic crystal fiber (PCF) amplifier beam profile at power level above 400 W.....	83
Figure 31: Microscope end-face view of a commercial-of-the-shelf (COTS) large mode area photonic crystal fiber having a 40 μm Yb-doped core, stress applying parts and air hole lattice used to guide the signal mode. The air clad is 400 μm in diameter.....	84
Figure 32: (black) Output power of signal vs. launched pump power showing a slope efficiency of 77%.	85
Figure 33: Beam profile and M^2 measurement at 400 W output.	86
Figure 34: The core design of the segmented acoustic fiber. The Brillouin shift in the center region comprised of one hexagon is different than that in the outer region comprised of six hexagons. The acoustic velocity of each region is denoted by $v_{1,2}$, and the optical mode field diameter is overlaid to scale.	89
Figure 35: (left) Optical delta profile of a step index fiber with core doped with GeO_2 only. (right) Acoustic delta profile of a fiber with more Al_2O_3 , and subsequently, less GeO_2 doped in the inner region of the core.[82].....	91

Figure 36: Acoustic velocity profile of fiber preform for Corning fiber design given in Figure 12.[82]	92
Figure 37: Optical and acoustic refractive index profiles in the Segmented Acoustically Tailored (SAT) fiber design.....	93
Figure 38: Pump probe experimental setup showing two NPRO lasers labeled “SBS Seed” and ”SBS Pump”. The two lasers are sampled by fused fiber couplers for beat frequency measurements. The two signals are free space coupled into the test fiber in a counter propagating configuration. Thermal tuning of the SBS pump laser shifts the frequency through the Brillouin resonance of the test fiber. A power meter is used to measure scattered SBS pump light. The power and beat frequency are measured simultaneously with a computer controlled data acquisition card.	97
Figure 39: Frequency dependence of thermal tuning typical of a JDSU NPRO laser. The solid lines represent regions of continuous single axial mode tuning. The dashed segments at the end of these lines indicate the laser is near a mode hop. The heavy dashed line represents the average tuning coefficient for the laser as it passes through mode hops.[105].....	98
Figure 40: The Brillouin gain spectrum for a conventional step index 25/400 PM fiber. The experimental data, shown in blue, and a Lorentzian curve fit (red) overlays the measured data.	100
Figure 41: The Brillouin gain bandwidth as a function of pump power. A linear fit(solid blue) is applied to the measured data (black asterisk) give an estimate for the spontaneous Brillouin gain bandwidth at zero pump power of 59 MHz.	101
Figure 42: The Brillouin gain spectrum for a LMA photonic crystal fiber. The experimental data, shown in blue, and a Lorentzian curve fit (red) is overlays the measured data.	102
Figure 43: Brillouin gain spectrum fit with 8 Lorentzian functions, based on the assumption that the segmented core is acoustically inhomogeneous. The experimental data is almost perfectly overlaid with the fit. The individual Lorentzian functions used in the fitting function are also plotted.	105
Figure 44: Corning acoustically tailored fiber design used for single-frequency amplifier power scaling. The measured Brillouin gain bandwidth is approximately 480 MHz, which is 10 times larger than the standard Yb-doped LMA fiber.	107
Figure 45: Effective Brillouin gain for each acoustic mode, denoted by asterisk, is show for the shift frequency range of interest. A peak Brillouin gain, $g_B = 5 \times 10^{-11}$ m/W, is divided by the effective area for each mode.....	111

Figure 46: The Brillouin gain bandwidth as a function of pump power. A linear fit(solid blue) is applied to the measured data (black asterisk) give an estimate for the spontaneous Brillouin gain bandwidth at zero pump power of 58 MHz.....	112
Figure 47: Measured Brillouin gain spectrum of the reference photonic crystal fiber. The main peak is fit with a Lorentzian function giving a center shift frequency of 15.94 GHz and gain bandwidth of 47.74 MHz. The high shift frequency side shows an increased Brillouin gain, similar to previous photonic crystal fiber measurements.....	113
Figure 48: Numerical fit (solid line) obtained by solving the 2x2 coupled system of nonlinear equations overlays the experimental data (circles) for a range of pump powers.....	115
Figure 49: Brillouin gain spectrum for SAT fiber. Two Brillouin peak are shown with center shift frequency of 15.715 and 15.938 GHz, respectively. Each peak has a Brillouin gain bandwidth of ~50 MHz. The high shift frequency side shows an increased Brillouin gain, similar to previous PCF measurements.....	116
Figure 50: SAT(red) and reference PCF(blue) BGS comparison. The ratio of peaks in the reference and SAT fiber is approximately 1.8.....	117
Figure 51: (left) Experimental setup to study SBS mitigation of acoustically tailored fiber in conjunction with the thermal gradient. (right) The idealized temperature profile in the fiber for the experimental arrangement.....	118
Figure 52: BGS for acoustically segmented fiber with step temperature profile applied leading to four primary peaks. The differences in relative gain among the peaks are attributed to non-ideal heating conditions in the fiber oven.....	119
Figure 53: Microscope end view of the reference PCF. The two dark regions next to the core are stress applying parts for PM operation. The thin dark circle defines the pump clad region.....	120
Figure 54: Configuration of photonic crystal fiber in experimental setup. Seed laser is input from the left, where the fiber is held in a water-cooled chuck. Approximately 2-2.5 meters of fiber is left in air before it is spooled on the aluminum holding ring. Cold plates are affixed to the aluminum ring on the top and bottom to improved conductive cooling of the fiber. The end of the fiber comes off the aluminum ring and held in the pump input side water cooled chuck.....	122
Figure 55: (black) Output power vs. voltage for Laserline Diode pump. (red) Center wavelength of pump diode laser output, which has been thermally detuned from operation at 976 nm.....	123

Figure 56: (black asterisk) Experimental data for signal output power vs. launched pump power from the 10 meter reference photonic crystal fiber amplifier. (red circle) The numerical model's prediction for output power of the amplifier.....	124
Figure 57: (black asterisk) Experimental data for backward power as a function of output signal power, showing a departure from linear growth. (red circle) The numerical models prediction for backward power.	127
Figure 58: Optical spectrum analyzer data for reference PCF amplifier are three power levels. The peak associated with Rayleigh scattered light is indicated by the vertical dotted black line. The Stokes scattered light is indicated with the vertical solid black line. The peak separation is ~0.06 nm, corresponds to ~16 GHz at 1064 nm.	128
Figure 59: Optical spectrum analyzer data for reference PCF amplifier at 150 W output power. The single peak, at 1064 nm is over 40 dBm above the noise floor, indicating negligible amplified spontaneous emission.	129
Figure 60: Beam quality measurement at 150 W output power, including an image of the fiber output imaged onto a camera. The M^2 was measured to be less than 1.2 for both axes.....	130
Figure 61: Scanning Fabry-Perot output data captured with an oscilloscope. The Fabry-Perot is adjusted such that two signal resonances are achieved over one scan range. The known cavity free spectral range is used to scale temporal data, given by the oscilloscope, to units of frequency.	132
Figure 62: (black) Single Stokes peak as measured by the Fabry-Perot at an amplifier output of 50 W. (blue) The numerical model prediction of the Brillouin gain spectrum is in agreement with experimental data. A Gaussian fit best represents the data, thus it is used to characterize the Brillouin gain bandwidth at 20MHz.	133
Figure 63: (black asterisk) Experimental measurement of Brillouin gain spectrum as a function of signal power. (red circle) Numerical models prediction. (blue line) A fitting function, which estimates Brillouin gain bandwidth in the high gain regime is plotted to give the general trend of bandwidth narrowing.	134
Figure 64: (black) Experimental data for the Brillouin gain spectrum out of the amplifier operating at 110 W output, as measured by the Fabry-Perot. (blue) Numerical model prediction for the same output power.....	135
Figure 65: (black asterisk) Experimental data for signal output power vs. launched pump power from 10 meter reference photonic crystal fiber amplifier. (red circle) The numerical model prediction for output power of the amplifier.....	137

Figure 66: (black asterisk) Experimental data for backward power as a function of output signal power, showing a departure from linear growth. (red circle) The numerical model prediction for backward power.	139
Figure 67: Optical spectrum analyzer data for reference PCF amplifier at three power levels. The peak associated with Rayleigh scattered light is indicated by the vertical dotted black line. The Stokes scattered light is indicated with the vertical solid black line. The peak separation is ~ 0.06 nm, corresponds to ~ 16 GHz at 1064 nm.	140
Figure 68: (black) Experimental data for the Brillouin gain spectrum out of the amplifier operating at 110 W output, as measured by the Fabry-Perot. (blue) Numerical model prediction for the same output power.	141
Figure 69: Brillouin gain spectrum for the segmented acoustically tailored fiber at various power levels. Each spectrum is referenced to the Rayleigh light peak to show shift due to the thermal gradient established in the fiber.	144
Figure 70: Brillouin gain spectrum prediction by the numerical model after optimization of the effective cooling coefficient for the aluminum ring. A free convection cooling coefficient, $h \approx 5$ W/m ² K, was used for the fiber suspended in air. An effective cooling coefficient, $h_{\text{eff}} \approx 200$ W/m ² K, was used for the fiber held in the aluminum ring.	145
Figure 71: Average core temperature as a function of fiber length given by the numerical model. The fiber is cooled by free convection from 0-2.5 meters. The rest of the fiber, 2.5-10 meters, is cooled more efficiently by the aluminum ring.	146
Figure 72: Optical spectrum analyzer data for reference PCF amplifier at 350 W output power. The single peak, at 1064 nm is over 40 dBm above the noise floor, indicating negligible amplified spontaneous emission.	147
Figure 73: (left) Near field image of PCF amplifier operating at 300 W output power, leading to an $M^2 < 1.3$. (right) Near field image of PCF amplifier operating above 490 W, leading to $M^2 > 1.5$	148
Figure 74: Beam quality as a function of output power for a PCF amplifier which is (blue asterisk) conductively cooled and (red asterisk) left suspended in air, with no external cooling applied.	151

LIST OF TABLES

Table 1: Characteristic advantages found in rare-earth-doped fiber amplifiers. [1].....	3
Table 2: Peak Er^{3+} absorption and fiber amplifier quantum efficiency for various glass host compositions in core pumped EDFA.[26]	11
Table 3: Typical parameters for large mode area Yb-doped fused silica fiber at 1064nm.	25
Table 4: Common fused silica fiber dopants and the qualitative effect on acoustic and optical refractive index. [82]	34
Table 5: Summary of selected SBS mitigation techniques, including threshold improvement and compatibility with other schemes.	36
Table 6: Example doping configuration for Segmented Acoustically Tailored fiber core.....	93

CHAPTER 1

Introduction

1.1. Scope of Work

The scope of this dissertation will be limited to single-transverse mode, single-frequency, ytterbium (Yb-) doped, continuous wave (CW) fiber amplifiers operating at 1064 nm and associated nonlinear optical effects. The terms *fiber amplifier* and *fiber laser* are often used interchangeably. It is worthwhile to recognize two distinct architectures employing rare earth doped fiber as the gain media. Using a tacit definition for laser, a *fiber laser* is made when the doped fiber gain media is placed within an optical cavity. A *fiber amplifier* is made when a doped fiber provides gain to an injected optical signal in a single pass, i.e. no resonant cavity. The discussion to follow refers to fiber amplifiers and their development. The architecture of all fiber amplifiers presented is generally referred to as master oscillator power amplifier (MOPA). A low power seed laser having the desired spectral characteristics of the high power output is coupled to a fiber and amplified by the fiber gain media. The goal of this research is to investigate power scaling in single-frequency fiber amplifiers. It is well known that stimulated Brillouin scattering (SBS) is the primary limiting factor in scaling the output power of single-frequency fiber amplifiers. From this we will create a working definition for laser linewidth as it will become relevant in later sections. An amplifier will be considered *single-frequency* if the linewidth is less than the Brillouin gain bandwidth, (nominally

$\Delta\nu_B \sim 50$ MHz in optical fibers at $\lambda_L \sim 1064$ nm). An amplifier will be considered *narrow linewidth* if the laser linewidth is larger than $\Delta\nu_B$, but less than 30 GHz; else, for linewidths > 30 GHz, it is considered to be broadband.

The research presented here was performed at the Air Force Research Laboratory, Directed Energy Directorate, on Kirtland AFB. Funding for this effort was provided by the United States Air Force, High Energy Laser Joint Technology Office (HEL-JTO), and the Air Force Office of Scientific Research (AFOSR).

1.2. Background

Fiber amplifier technology has undergone a rapid progression in the past 10 years relative to bulk solid state lasers. Today, fiber amplifiers offer a viable alternative to canonical laser systems for applications such as frequency conversion, remote sensing, materials processing, beam combination, and gravitational wave detection. The impetus for such a large scale effort to push the technology is clear when one considers all the desirable qualities innate to the rare earth doped fiber amplifier architecture.

Table 1: Characteristic advantages found in rare-earth-doped fiber amplifiers. [1]

Fiber Amplifier Characteristic	Advantage
Robust Single-Transverse Mode Operation	Freedom from thermal mode distortions
Broad gain bandwidths (up to ~20 THz)	Allowing ultra short pulse and broad tunability
Availability of high gains	Enables MOPA configuration
High optical to optical efficiency	High efficiency
Monolithic (all fiber) architecture	Removes the need for free space components

While fiber laser technology seems to be a relatively new field of research, laser action in a glass waveguide was proposed by Snitzer only one year after the first experimental demonstration of the laser.[2] One year later Etzel, Grandy, and Ginther reported the first coherent radiation from a Yb-doped glass matrix, operating around 1 μm . [3] The first coherent source using an optical fiber as the gain media, demonstrated in 1964, was a flash-pumped neodymium-doped barium crown glass core surrounded by a lower index sodium lime silicate cladding.[4] At that time, passive loss in glass waveguides was significant, thus making long fiber amplifiers impractical. The following 25 years saw substantial growth in fiber optics technology, primarily motivated by its potential application to long haul communications systems. In 1966 Kao and Hockham proposed high purity silicon dioxide (SiO_2) (fused silica) as a suitable material for optical transmission. They also mathematically described the dielectric waveguide and predicted the transmission loss to be less than 20 dB/km.[5] That prediction was experimentally validated by Kapron, Keck, and Maurer in 1970.[6] By 1986, transmission loss in pure fused silica fibers was nominally 0.2 dB/km, very close the intrinsic material loss.[7]

1.3. Advances in Fiber Amplifier Technology

Twenty years of fiber development set the stage for the advent of fiber amplifiers. The first modern fiber amplifier was demonstrated in 1987 with an erbium-(Er-) doped single-transverse mode gain fiber amplifier (EDFA).[8] The amplifier was seeded with a GaInAsP laser diode operating at 1.54 μm , and pumped with a 4-dicyanomethylene-2-methyl-6-p-dimethylaminostyryl-4H-pyran (DCM) dye laser operating around 660 nm. The goal of this amplifier demonstration was to show fiber amplifiers could be an alternative to optical repeater technology used in telecommunications. The laser characteristics of the amplifier showed high gain, and low noise operation over a wide bandwidth (300 GHz) which were highly desirable qualities for the application. The architecture, however, was not ideal, as the seed and pump were free-space-coupled into the gain fiber.

The next 15 years saw an explosion of development in rare-earth-doped fibers and supporting fiber component technology. The primary advances which set the foundation for the research presented here are polarization-maintaining (PM) fibers, double clad fibers, and diode pumping. The following sections contain a brief discussion of these technologies, highlighting the features most relevant to the work presented in this dissertation.

1.3.1. Polarization Maintaining Fiber

Early in the development of optical fibers and fiber amplifiers the need for a stable polarization state in transmission was addressed.[9] The general concept behind

almost all PM fiber designs is to impart stress on the core thus creating birefringence. There have been countless demonstrations of novel methods for the preservation of polarization in a fiber.[10] Since it is not relevant to this work, a review of PM fiber designs will not be presented here. Instead, a description of the PM fiber design most commonly used in fiber amplifiers today will be given.

The polarization-maintaining and absorption-reducing (PANDA) fiber was first introduced in 1982.[11] The issue at the time was imparting sufficient birefringence in the core of the fiber to preserve polarization without adding loss to the signal. As the name suggests, the PANDA design solved this issue. However, Figure 1, taken from [12] identifies how apropos the name is.

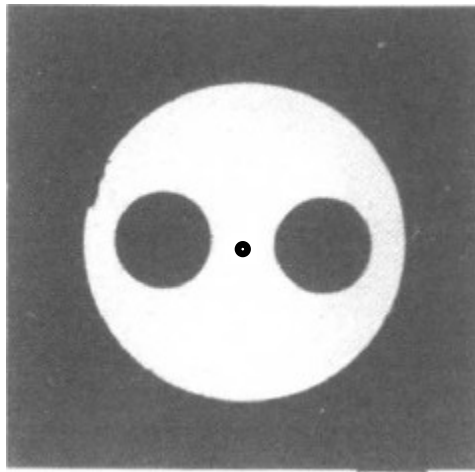


Figure 1: End view of a PANDA fiber. The two dark circles are stress applying parts provide birefringence in one axis of the core. The core is centrally located between the stress applying parts.

The two dark circles in Figure 1 are stress applying parts (SAP) which create a birefringence in one axis of the core. The core is not visible in the original photo, so a circle has been overlaid to show its approximate position. The SAP's are typically fused silica rods doped with a high concentration of boron oxide (B_2O_3). The high

concentration of B_2O_3 changes the softening temperature and thermal expansion coefficient of the SAP relative to the fused silica cladding. As the fiber cools, after it is drawn down, the SAP's tend to push against the surrounding cladding locking a permanent stress gradient along one transverse axis of the fiber.[10] The general design of the PANDA fiber is used in almost all commercially-available PM fibers today.

1.3.2. Double Clad Fiber

Researchers recognized the potential of fiber amplifiers in applications outside the telecommunications industry, but faced another fundamental limitation. Throughout the 1980's a major problem in the design of fiber amplifiers was the limitations associated with core pumping. If the fiber waveguide is single-transverse-mode, a single-transverse-mode pump source is required for efficient pump absorption. Since there will always be a loss in power conversion from pump to signal, end pumping into the core will cause the signal brightness to be less than the pump.[13] This problem was solved with the advent of the double clad fiber design.[14] As the name suggests, the double clad fiber has two concentric waveguides. One cladding is used for the confinement and propagation of the signal, while the second is used for the confinement and propagation of a multi transverse-mode pump. The multi-mode (MM) pump cladding is generally established by coating the fiber with a low index polymer. This polymer serves to protect the fiber, but is also easy to remove for fiber processing. In a rare earth doped double-clad fiber, only the core is doped with active ions. The cladding is generally pure fused silica. As the MM pump light propagates down the fiber it is absorbed by the core. Figure 2 shows the geometry of a standard step-index double-clad fiber.

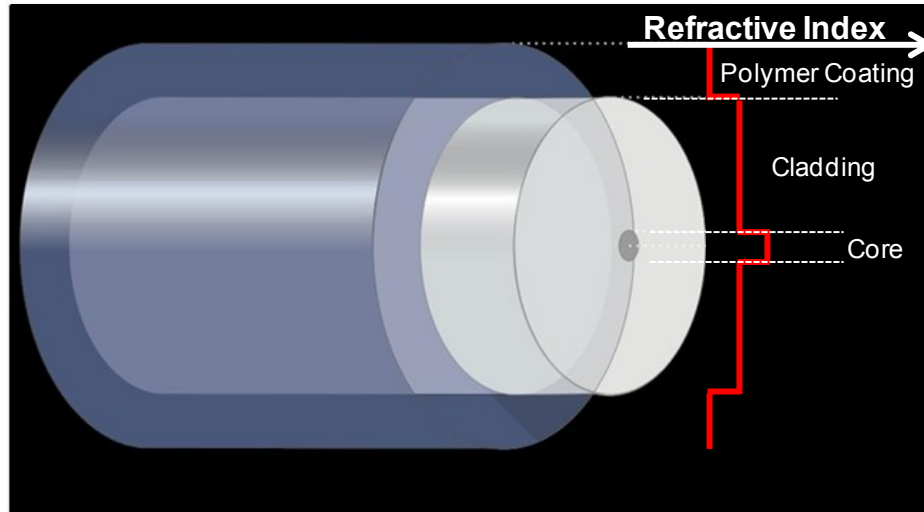


Figure 2: Double-clad fiber where core is designed to guide signal light and cladding is designed to guide pump light. A polymer coating is used to protect the fiber.

A low brightness diode array, composed of many individual emitters, could be used as the pump source while maintaining a single-transverse mode in the core. Furthermore, the fiber amplifier could now act as a brightness converter, by taking low brightness high power laser diode light in the cladding and transferring the energy into a high brightness signal in the core. This design coupled with the continually improving technology of high power multi-mode (MM) LD's[15] had a significant impact on the field of fiber amplifiers, and set the stage for large scale effort in power scaling.

1.3.3. Diode Pumping

Early in the development of fiber amplifiers, researches realized practical pump sources at the desired wavelengths were not readily available. Fortunately, laser diode technology was becoming more reliable offering CW or pulsed mode operation at room

temperature for 100s-1000s of hours.[16] Laser diodes (LD) proved to be ideal pump sources for the gain fiber since they were inexpensive and easy to implement relative to other pump sources e.g. argon ion/dye laser.[17] The first diode-pumped fiber amplifier was demonstrated in 1988.[18] The seed and pump were free space coupled into the core of an Er-doped gain fiber, which supplied 6 dB of single-pass gain. The facility in using diode lasers as pump sources is found in their ability to output significant powers in a broad range of wavelengths, provided efficient coupling between the diode and the fiber could be achieved. Thus, diode pumping became a standard in fiber amplifier architecture.

The Er-doped gain fiber received the most attention in the early development of fiber amplifiers. The spectroscopic properties of erbium fibers are such that they have high laser gain near 1.54 μm , and a low loss window in silica; thus enabling long distance communications.[8] By the early 1990's the industry had essentially solved most technical issues with the EDFA for the telecommunications application.[19] The use of single-clad, and single-mode pumps was sufficient for the telecommunications application. Applications which required higher powers were still out of reach for fiber amplifier technology, despite the introduction of the double clad fiber, primarily due to the lack of high power pump sources. The laser diode market would need approximately 10 years to catch up to advances made in fiber amplifiers. Consistent with a large focus on fiber amplifier power scaling, was an equally significant effort in scaling fiber coupled MM diodes.[15] Today, the fiber coupled diode market has actually overtaken the fiber power scaling effort. Multi-kilowatt fiber coupled diode pumps are commercially available from many vendors. The limiting factor now is the price of such a device.

Fundamentally, high power MM pump diodes and the double clad fiber are the most significant advances in fiber amplifier technology within the context of power scaling. A MM diode laser can efficiently pump a single mode fiber to produce single mode amplification. This simple configuration allows for a large enhancement in the fiber amplifier brightness, relative to the MM pump. Additionally, less stringent requirements on the diode laser mode quality dramatically increases achievable output powers. Since brightness and power are the figures of merit in many laser applications, these two advancements significantly increased the utility of fiber amplifier technology. Without either of these, fiber amplifiers would be limited to less than 10 W output power.

1.4. Early Development of the Yb-doped Fiber Amplifier

Before a history of Yb-doped fiber amplifier (YDFA) power scaling is given, an important question must be answered. Why Yb-doped glass would be preferred to other rare earth dopants? In general, rare earth ions exhibit characteristics that distinguish them from other optically active ions. They emit and absorb over narrow wavelength ranges. The wavelengths of the emission and absorption transitions are relatively insensitive to host materials. According to parity selection rules, optical transitions from the infrared to the ultraviolet are forbidden in rare earth ions. As such, the spontaneous lifetimes of metastable states are long allowing high population inversions to be obtained under steady-state conditions with modest pump powers.[20] Additionally, the non-radiative relaxation rates of rare earth doped glasses at room temperature are generally much smaller than the radiative transition rates resulting high quantum efficiencies.[21] All of

these characteristics are desirable in considering gain materials for lasers. This generalization, however, does not translate to experimental results in power scaling for all rare earth doped fiber amplifiers. Ion-ion interactions complicate optical transitions and reduce efficiency for many rare earth ions.

1.4.1. Power Scaling in Er-Doped Fibers

The Er-doped fiber amplifier (EDFA) dominated the field of fiber amplifiers throughout the 1980's and early 1990's, primarily due to its application in the telecommunication industry. The maturation of fiber technology opened new areas of interests that were not necessarily confined by the specific wavelength advantage of the EDFA. Additionally, researchers found power scaling in EDFA's difficult. As a point of reference, the highest reported power from a diode-pumped EDFA in 1989 was 13 mW.[22] The primary drawbacks are concentration quenching by interionic energy transfer and homogeneous up-conversion.[23,24] The latter process was well known for rare earth ions, and was named "addition de photon par transferts d'energie" (APTE) in 1966. [25]

Concentration quenching is the reduction in the quantum efficiency of an ion with increasing concentration. It can occur through a number of ion-ion interactions, e.g. cross-relaxation, up-conversion, and excited state absorption.[21] The impact of this effect for Er-doped silica is shown in Table 2.

Table 2: Peak Er^{3+} absorption and fiber amplifier quantum efficiency for various glass host compositions in core pumped EDFA.[26]

Host glass composition in SiO_2	Peak Er^{3+} absorption dB/m	% Quantum Efficiency
	20	9.5
GeO_2	6.3	21
	0.8	81
$GeO_2-P_2O_5$	4	55
	1.17	81
	0.74	80
Al_2O_3	8	76
$Al_2O_3-GeO_2$ (Al:Ge)		
1:2	7.5	87
1:2	6.1	88
1:2	5.5	85
1:10	3.1	87
1:33	4.9	74

The results presented in Table 2 show an inverse relationship between peak absorption of the pump laser and the quantum efficiency of the fiber amplifier.

Additionally, the quantum efficiency is improved when Er^{3+} is co-doped with Al_2O_3 . The explanation for this, described more rigorously in the section on photodarkening, is the tendency for Al-doping to reduce clustering of rare earth ions.

Researchers noted the fact that concentration quenching may be avoided by improving the fabrication process. However, homogeneous up-conversion (or APTE) set definite limits on the quantum efficiency of EDFA's.[24]. Homogeneous up-conversion, in Er-doped fibers, is a process by which energy is transferred between two excited ions. It is the major cause of inefficiency for Er^{3+} devices at 1550 nm.[21] Figure 3 below is an example of the process for a pair of Er^{3+} ions, pumped at 1480 nm.

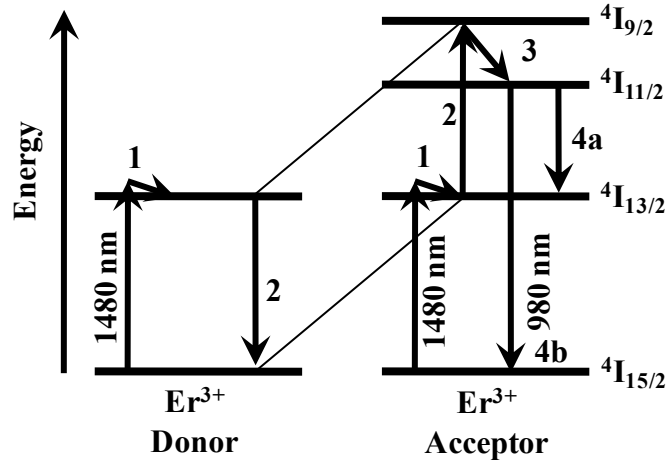


Figure 3: Energy-transfer up-conversion between two Er^{3+} -ions. Transitions labeled (2,4a) represent non-radiative transitions. All other arrows represent radiative transitions.[24]

The process in Figure 3 starts with two ions being excited to the state $4I_{13/2}$ (arrows marked “1” in Figure 3). Then, energy is transferred from one ion (the donor) to the other (the acceptor, arrows marked “2”). This relaxes the donor and up-converts the acceptor to state $4I_{9/2}$. Transition from the $4I_{9/2}$ state to the $4I_{11/2}$ state is on the order of nanoseconds. The transition marked “4a” is the most probable as it is a decay to the upper lasing level, but a small fraction undergoes the transition marked by “4b”, which is dictated by the branching ratio.[24]

The results found in Refs. [24,26] essentially removed the EDFA from the forefront of fiber amplifier power scaling technology, although work in the area continues. Researchers in the field have moved to more exotic fabrication processes in an effort to overcome the challenges described above. To date the highest power EDFA reported is 67 W, at 1570 nm.[27] A higher power, 151 W, was achieved with the use of Er:Yb co-doping.[28] While these powers represent a significant increase relative to the

state of the art in 1989, they pale in comparison to those obtained in Yb-doped fiber amplifiers

For the sake of brevity, only the issues involved in power scaling the EDFA will be discussed in any level of detail. The EDFA was chosen only because the focus of this section in the dissertation is to provide an historical perspective on fiber amplifier technology. Research into many rare earth doped fibers is on-going, with some showing great promise. However, in most cases other rare earth ions suffer from similar issues to those described above for Er^{3+} . The reader is referred to the literature for a more in-depth discussion regarding the subject.[1,21]

Suffice it to say, the YDFA has garnered the most interest within the field in the past 20 years. To answer the question posed above, within the context of the preceding section, we must investigate the spectroscopy of the Yb^{3+} ion.

1.4.2. Yb^{3+} Spectroscopy

The first demonstration of laser action in a Yb-doped glass matrix was reported in 1962.[3] Twenty-five years later, researchers at the University of Southampton revisited the subject and pioneered the study of Yb-doped silica.[29] The YDFA gained significant attention in the mid-90's with a detailed characterization of Yb-doped glass.[30] Subsequently, the same group published a more complete characterization, including a simple model highlighting the versatility of the YDFA operating in the 1 μm region.[31] This seminal paper described the advantages specific to YDFA's relative to other rare earth dopants in glass. The authors note YDFA's are not subject to the

complications described above, such as excited state absorption and concentration quenching. Furthermore, YDFA's exhibit the advantageous features characteristic of rare earth dopants, e.g. broad gain bandwidth, high efficiency, and high doping concentrations. The reason for this confluence of desirable characteristics is found in the spectroscopic properties of Yb-doped glass.

The spectroscopic properties of Yb^{3+} are simple compared to other rare earth ions. For all optical wavelengths, only two level manifolds are relevant: the ground-state $^2F_{7/2}$ (with four Stark levels labeled (a)-(d) in Figure 4) and a well-separated excited-state $^2F_{5/2}$ (with three Stark levels labeled (e)-(g) in Figure 4) spaced by approximately $10,000\text{cm}^{-1}$. [21,30]

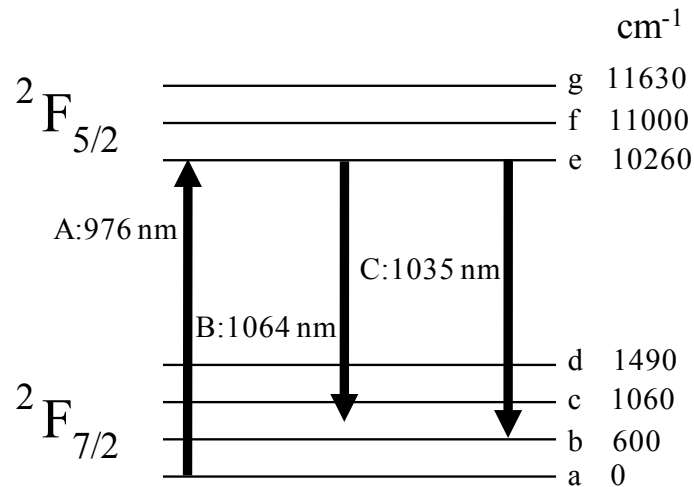


Figure 4: The Yb^{3+} energy level structure, consisting of two manifolds. Approximate energies in wavenumbers above ground energy are indicated. Label A indicates the characteristic pump wavelength. Label B indicates characteristic signal wavelength. Label C indicates characteristic peak amplified spontaneous emission for signal wavelength choice of 1064 nm.

The transitions between sublevels are not fully resolved in glass at room temperature because of strong homogeneous and slight inhomogeneous broadening correlated to pump wavelength. The large energy gap and absence of higher energy states mitigate issues such as concentration quenching, and excited state absorption. Additionally, these features allow for high doping concentrations, often over 10,000 ppm. To put that in perspective, the Er-doped fiber used in Ref. [27] had a doping concentration of ~ 700 ppm. The upper-state lifetime is ~ 0.8 ms, with a variation of 30% depending on co-dopants in the fiber.[31]

The resultant absorption (solid line in Figure 5) and emission (dotted line in Figure 5) cross-sections are shown below. The labels A-C correspond to the transitions highlighted in Figure 4. This was done only to identify the transitions most relevant to the work presented here.

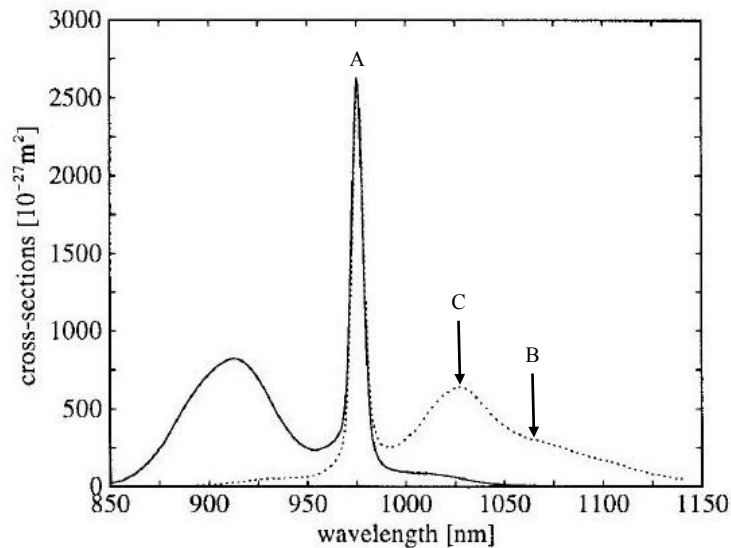


Figure 5: Absorption (solid) and emission (dotted) cross sections of Yb-doped germanosilicate glass.[31]

The spectroscopic information shown compositely in Figures [4-5], exposes the multitude of pumping and lasing possibilities in Yb-doped glass. From a visual inspection of Figure 5, it is clear the 910 nm pump region would provide the largest upper state population. However, the gain at 976 nm is strong; consequently gain at longer wavelengths is limited by amplified spontaneous emission (ASE) at 976 nm. A lasing wavelength of 976 nm is also problematic since the emission and absorption cross sections are nearly identical, thus the net gain for 976 nm is limited by re-absorption further down the fiber.[30] A choice of 976 nm pump and lasing wavelength of 1064 nm provides efficient pump absorption, while limiting re-absorption of the signal light. It is true that 1064 nm does not provide the most gain in the 976 nm pumping configuration, and will be limited by ASE in the 1035 nm region. However, as discussed in a later section this issue is easily resolved by saturating the amplifier with sufficient seed power and building multiple stages of amplification.

1.4.3. Photodarkening

The term photodarkening has been ascribed to the temporal increase in the transmission losses of rare earth doped glass.[32] Early work on the characterization of photodarkening was done on EDFAs. Reliability in long term operation of the EDFA was essential since the amplifiers served as signal repeaters in long distance fiber optics networks. The amplifiers were most commonly placed at intermediate points in fiber transmission lines under oceans. As such, repair or replacement was expensive.[33]

It was well-known that germanium (Ge-)doped optical fibers exposed to intense radiation in the visible spectrum exhibited an optical darkening effect.[34] The physical basis for the process is attributed to two-photon absorption which breaks molecular Si-Ge and Ge-Ge bonds, characteristic of oxygen-deficient germanosilicates.[35] The broken bonds release electrons with sufficient energy to drift through the glass matrix eventually recombining or becoming trapped at other Ge sites to form color centers. The color centers serve as points of absorption, thus increasing the passive loss of the fiber. [36] Similar experiments to those done in Ref. [36] were carried out for EDFAs.[37] The amplifier was pumped at 1480 nm and seeded with 1550 nm; the desired specifications for the telecommunications industry. The test was designed to investigate reliability issues related to photodarkening, specifically for the undersea transmission application. In two separate tests, including a one year continuous operation demonstration, the authors found no significant increase in passive loss due to photodarkening. Unfortunately, the same results were not found for fibers doped with other rare earth ions. Photodarkening effects have been reported in silica fiber doped with thulium (Tm^{3+}), terbium (Tb^{3+}), cerium (Ce^{3+}), praseodymium (Pr^{3+}), Europium (Eu^{3+}), and ytterbium, (Yb^{3+}).[38,39,40,41,42]

Photodarkening in Yb-doped fibers was not addressed in rigor until the early 2000's. In retrospect, this was most likely related to the power scaling trend for Yb-doped fiber sources. Significant powers ($>100\text{W}$) from Yb-doped fiber amplifiers and fiber lasers were not realized until the late 1990's.[43] A large field of research focused on power scaling called for manufacturers to draw fibers with increasing Yb concentration. High concentrations of Yb^{3+} are required for efficient pump absorption in

practical lengths of gain fiber. Nonlinear interactions, for example, scale with fiber length, and potentially limit output power. Previous work showed multi-component silicate glasses, such as aluminum oxide (Al_2O_3)-doped fused silica, improved the solubility of rare earth ions.[44,45] Recall from above, Er^{3+} concentration in EDFAs is limited by APTE. The spectroscopic properties of Yb^{3+} dictate this process is unlikely due to its lone $^2\text{F}_{5/2}$ excited state. Working from this theory, researchers proceeded to draw high concentration Yb-doped fibers. Coincidental with this drive for high dopant concentrations was the realization of reduced excited state lifetime quenching, leading to a “strong un-bleachable loss” (the term photodarkening had not yet been introduced).[42] The conclusions from this work were vague, and commented more on the need for improvements in fiber fabrication. This was essentially the same interpretation given for high concentration Er-doped fibers (The same research group provided Refs. [24,42]). These conclusions did not address the un-bleachable loss effect. As an explanation for this un-bleachable loss, materials scientists in France hypothesized two distinct classes of APTE mechanisms. One class characterized the interionic energy transfers shown to limit power scaling in Er-doped fiber. The other class describes the un-bleachable losses seen in high doping concentrations of rare earth ions.[46] The latter class is defined as cooperative luminescence. In Yb-doped glass, these ion-ion interactions result in the generation of green light, which corresponds to twice the energy of a single excited Yb-ion. (Recall the energy level diagram for Yb^{3+} in Figure 4). Furthermore, they show this effect is only significant if the Yb-Yb ion spacing is very small. Using the oxygen deficiency center (ODC) model presented in Ref. [35] as a basis, this indicated chemical clustering of Yb-ions could be related to photodarkening. Later work, with refined fiber

fabrication processes, would corroborate the French researchers' hypothesis showing higher Yb^{3+} concentrations continued to exacerbate the photodarkening problem.[47,48] However, the authors in both Refs. [47,48] indicate clustering of Yb-ions is only part of the problem. The existence of impurities neighboring the Yb-ions clusters could also provide a means for the creation of ODCs. [49]

Recall, Al co-doping was originally intended to increase Yb^{3+} solubility in glass. Researchers found, if used appropriately, Al co-doping improved the photodarkening problem.[50] The authors of Ref.[48] found Yb-doped fibers, co-doped with Al_2O_3 , showed significant photodarkening compared to a Yb-free aluminosilicate reference fiber. This test was performed to show that Yb-ion clusters contributed to photodarkening, not Al_2O_3 . They also noted, however, that an increase in Al-doping tended to mitigate photodarkening. The explanation for this, consistent with the ODC Ref. [35], was the creation of oxygen deficiency centers (ODC) in the form of ill-valenced bonds between cations such as Yb-Al or Yb-Yb. This explanation suggested Al-doping worked to fill ODC's, thus reducing photodarkening.

Today, the nature of the defects responsible for photodarkening is still under debate.[51] Most of the information we have comes from fiber amplifier studies. As such, the field is continually generating hypotheses on microscopic properties through macroscopic demonstrations.[52] As the commercial market for Yb-doped fibers has grown, fiber manufactures have become less likely to publish explanations or "recipes" for the reduction of photodarkening. The discussion above represents to the most commonly accepted explanation for the mitigation of photodarkening.

1.5. Single-Frequency Fiber Amplifier Power Scaling

The literature shows single-frequency laser operation as far back as 1962.[53] Initial applications for these types of lasers were generically stated in terms of “metrology” and “communications”.[54] The years to follow these initial demonstrations have provided applications for single-frequency radiation in a broad spectrum of research science. This dissertation is focused on the realization of high power, single-transverse mode, single-frequency, CW, YDFA’s. The primary applications for consideration are coherent beam combination (CBC)[55], inter-satellite communications[56], and gravitational wave detection.[57] As such, the qualifiers placed on the YDFA (e.g. single-frequency, single-mode) are dictated by the mutual requirements of these applications. The foregoing sections and discussion summarize a subset of advances in fiber amplifier technology enabling these specific endeavors. A brief review of the history regarding the subject will establish the challenges faced in that enterprise and identify the novelty of the work present in this dissertation.

1.5.1. Single-Frequency YDFA: Initial Demonstrations

The need for high power, low noise, single-frequency lasers in gravitational wave detection prompted researchers in Germany to build the first YDFA, having those characteristics.[58] Previous work in solid-state lasers provided an ideal seed source for the amplifier with the demonstration and eventual commercialization of the non-planar ring oscillator (NPRO).[59] The NPRO most commonly used in single-frequency YDFA’s are diode pumped unidirectional ring resonators entirely internal to a single

Nd:YAG crystal. Characteristics inherent to NPRO laser, such as low phase noise, spectral purity, and low frequency jitter, make it an ideal seed source for single frequency fiber amplifiers. Figure 6 is an example of the resonator design.

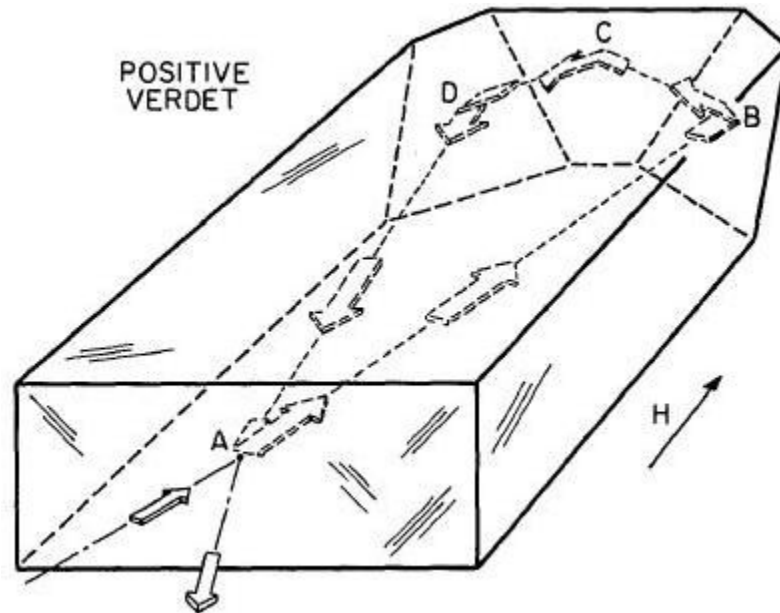


Figure 6: The non-planar ring resonator design. Polarization selection takes place at A. Points B,C, and D, total internal reflection occurs. A magnetic field H is applied to establish unidirectional oscillation. The diode pump enters the crystal at A.[59]

A unidirectional cavity eliminates spatial hole burning and frequency stability is enhanced by the monolithic structure.[59] The output power of such a laser, however, is limited to less than 10 Watts. To that point, the facility in using a YDFA is the ability to provide amplification while maintaining the desirable characteristics of the seed laser. The results from Ref. 58 proved promising. Approximately 20 W of single-frequency radiation with diffraction limited beam quality, limited by available pump power, was obtained. Two years later the same group achieved 100 W, with similar laser characteristics and an improved pumping scheme.[60] The simple amplifier

configuration, shown in Figure 7 below, is known as a master oscillator power amplifier (MOPA).

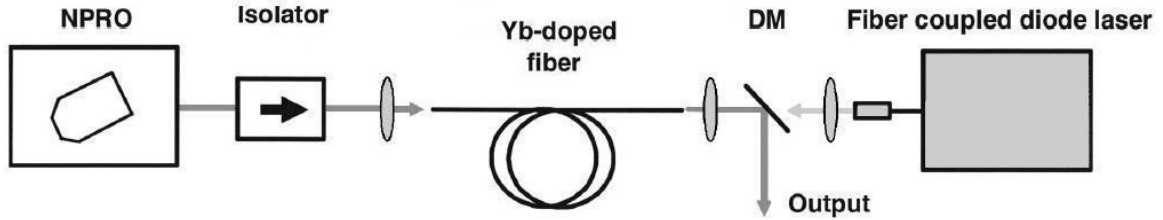


Figure 7: Single-Frequency master oscillator power amplifier (MOPA), pumped by a fiber coupled diode laser at 976 nm. DM is a dichroic mirror used to separate 1064 nm signal light and 976 nm pump light.[60]

A single-frequency NPRO was used to seed core of a double-clad Yb-doped fiber. A fiber coupled pump diode, operating at 976 nm, was injected into a multi-mode (MM) cladding waveguide in a counter-pumping configuration. The dichroic mirror was used to separate the output signal light from the injected pump light. Improvements in the pump laser allowed a significant increase in output power. Further power scaling was prevented by the onset of stimulated Brillouin scattering (SBS), the fundamental limiting factor in single-frequency fiber amplifiers.

1.6. Stimulated Brillouin Scattering Mitigation Techniques

Stimulated Brillouin scattering is a non-linear optical interaction between a pump (in this case the 1064 nm signal) wave and a counter-propagating Stokes wave mediated by an acoustic wave. Figure 8 shows an input laser at frequency ω_L scattering from the refractive index variation associated with an acoustic wave of frequency Ω_B . The

reflected Stokes light is frequency shifted downward since the acoustic wave front is co-propagating with the input laser.

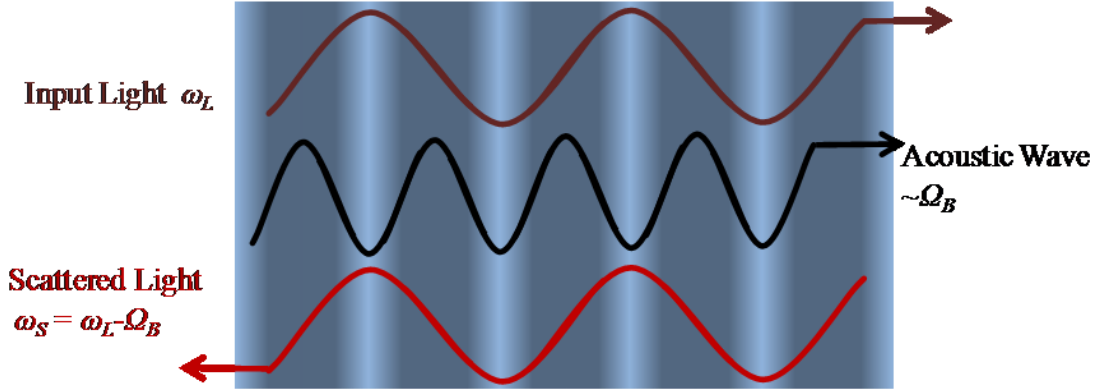


Figure 8: Stimulated Brillouin scattering. Input light at ω_L is scattered by refractive index variations (shown by modulated shading in background) associated with sound wave at Ω_B . The reflected Stokes light, ω_S , is frequency downshifted by Ω_B .

The process is initiated by thermal fluctuations in the fiber which manifest as spontaneous Brillouin scattering. In an optical fiber, the transition from spontaneous to stimulated scattering occurs when interference between the input laser and reflected Stokes light is sufficient to drive the acoustic wave through electrostriction.[61] The combination of single-frequency amplification, long interaction lengths, and tight confinement of the optical field result in the onset of SBS at low power levels.

The SBS process will be discussed in greater detail in the following chapter. For now, the following equations are introduced to provide a qualitative relationship between the quantities relevant to the SBS threshold, :

$$P_{Th} \sim \frac{A_{eff}}{g_{B,max} L_{eff}} \left(1 + \frac{\Delta \nu_l}{\Delta \nu_B} \right) \quad (1.1)$$

$$g_{B,eff}(z) = \frac{g_{B,max}}{1 + 4\left\{\left[\Omega_B + C_T \Delta T(z) - \omega_L - \omega_S\right]^2 / \Gamma_B^2\right\}} \quad (1.2)$$

$$\Omega_B = \frac{4\pi n_{eff} v_A}{\lambda_L} \quad (1.3)$$

Eq. (1.1) shows three of the primary factors dictating the power threshold for the onset of SBS in an optical fiber. Here, A_{eff} is the nonlinear effective area of the optical mode in the core, $g_{B,eff}$ is the effective Brillouin gain coefficient, L_{eff} is the non-linear effective length of the fiber, $\Delta\nu_L$, and $\Delta\nu_B$ are the laser and Brillouin gain linewidths respectively. Eq. (1.2) shows the Lorentzian line shape of the Brillouin gain spectrum as a function of the fiber length. In Eq. (1.2), $g_{B,max}$ is the peak Brillouin gain, Ω_B is the Brillouin frequency shift, C_T is a constant which characterizes how the peak Brillouin gain frequency shifts with temperature, ΔT is the longitudinal temperature difference, ω_L and ω_S are the laser and Stokes frequencies, respectively and Γ_B is the phonon lifetime of the acoustic wave in the medium. In Eq. (1.3), the Brillouin frequency shift is shown to depend on the effective index of refraction of the optical mode n_{eff} , at the laser wavelength λ_L , and the acoustic velocity v_A . Typical values for the parameters above are given in the table below.

Table 3: Typical parameters for large mode area Yb-doped fused silica fiber at 1064nm.

Parameter	Value	Units
A_{eff}	7×10^{-10}	m^2
g_B	2.5×10^{-11}	m/W
L_{eff}	5-15	m
Ω_B	1×10^{11}	rad/s
C_T	1.5-2.5	MHz/ $^{\circ}$ C
Γ_B	40-80	MHz
v_A	5900-6000	m/s

The relationships in the equations above are in not necessarily complete definitions; rather, they are intended as a heuristic guide for the review of SBS mitigation techniques in fiber amplifiers.

1.6.1. Linewidth Broadening

One of the most obvious SBS mitigation techniques is to simply broaden the linewidth of the signal laser. Eq. (1.1) shows that an increase in laser linewidth beyond the Brillouin gain bandwidth will increase the SBS threshold. A typical Brillouin gain spectrum bandwidth ($\Delta\nu_B$) is on the order of 50 MHz. Thus, it is trivial to defeat the SBS process in this way, in fact only a small subset of seed lasers are spectrally narrow enough to pump the process efficiently. Narrow linewidth fiber amplifiers, recall ($\Delta\nu_l > \Delta\nu_B$), have been demonstrated above 1 kW.[62,63] However, for many applications, e.g. nonlinear frequency conversion, gravitation wave detection, and coherent beam combination, increasing the linewidth may provide limitations. As such, this technique is considered an inadequate method of SBS mitigation.

1.6.2. Fiber Geometry

Increasing the optical mode area in the fiber is another method used for SBS mitigation. The term large mode area (LMA) is given to fibers with core dimensions larger than the standard single-mode fiber core. For example, at $\lambda_L \approx 1.06 \mu\text{m}$ a $6 \mu\text{m}$ core diameter supports only a single-transverse optical mode. Eq. (1.1) shows the SBS power threshold increases with the effective optical mode area (A_{eff}), i.e. increasing A_{eff} reduces the peak intensity. However, if single-transverse-mode operation is required, there are factors which limit core diameter scaling. Eq. (1.4) provides the V-number for a cylindrical step index waveguide. This parameter is used to characterize the waveguide by indicating the number of transverse modes supported.

$$V = a \frac{2\pi}{\lambda_L} \sqrt{n_{core}^2 - n_{clad}^2} \quad (1.4)$$

In the equation above, a is the core radius, λ_L is the laser wavelength, n_{core}/n_{clad} are the refractive index of the core and cladding, respectively. The number of transverse modes supported by the waveguide scales with the V-number. If the core diameter and laser wavelength are fixed, the index difference between the core and must be made sufficiently small for single-mode operation. In other words, the numerical aperture of the core must decrease as the core diameter increases. Typically, LMA cores support more than one transverse mode. This issue is largely mitigated by coiling the fiber. If applied appropriately, bending the fiber will induce significant loss for the higher order modes with minimal impact on the fundamental mode.[64] This technique only works

for “few-mode” fibers, generically defined as supporting less than 5 transverse modes. Additionally, bending the fiber may deform the fundamental mode field distribution and reduce the mode area.[65] Many novel techniques have been employed in an effort to decrease peak intensity while maintaining desirable modal characteristics in a fiber.[66] To date, the simple scheme described above has been the most successful.

At this point a distinction will be made between conventional step index fiber, shown qualitatively in Figure 2, and photonic crystal fibers. Current step index fiber manufacturing technology has a lower limit of numerical aperture (NA) $\sim .06$, which in turn limits single-mode operation, with induced bend loss, to core sizes $< 30 \mu\text{m}$.[67] The source of this limitation is related to variations in refractive index profile of the core. Photonic crystal fiber (PCF) manufacturers have produced core sizes of $100 \mu\text{m}$ with near single-mode operation.[68] Conversely, the ultra-large mode area PCF’s are made in rod-type fibers which restrict bending altogether. Rod-type PCF’s are generally used in pulsed amplifier configurations which require shorter interaction lengths. The gain fiber in a typical YDFA is 5-10 m, making unbendable rod-type PCF’s impractical. The standard LMA PCF used in CW YDFA’s has a $40 \mu\text{m}$ core diameter and $\text{NA} \sim .03$.[69] Unique waveguide design and manufacturing techniques allow for the increased core sizes in PCF’s while maintaining single-mode operation. Thus, spatial filtering requirements, in the form of bend loss, are relaxed. This topic will be discussed in a later section.

Another consideration in SBS mitigation is the fiber length. Eq. (1.1) is slightly more specific by dictating that the effective length (L_{eff}) be used. There are two considerations impacting the length of the gain fiber. First, as has been addressed in

previous sections, the pump light must be absorbed to provide amplification to the signal. A choice of 915 nm pump light would require a longer gain fiber for significant absorption, measured in (dB/m), compared to a 976 nm pump. The pump absorption also depends on the ratio of core and pump cladding areas. For example, the pump absorption of a fiber with a 20 μm core and 200 μm cladding (20/200) would be 4 times larger than a 20 μm core and 400 μm cladding (20/400). An additional nuance to the core/clad overlap is related to the pump cladding NA. A high NA pump cladding allows for tighter confinement of low brightness MM diode pumps. Thus, scaling the pump cladding NA allows for a reduction in pump cladding diameter, which leads to increased pump absorption.

The second consideration is related to the nonlinear effective length or, more appropriately, nonlinear interaction length. How the signal power grows in a Yb-doped gain fiber has a significant impact on Stokes light generation. Figure 9 shows the evolution of signal power in a co-pumped (pump and signal travel same direction) and counter-pumped (pump and signal travel opposite direction) configurations.

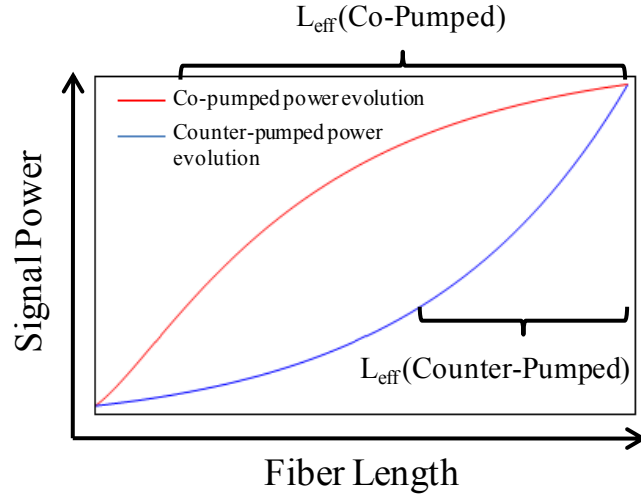


Figure 9: (red) Co-pumping power evolution in the fiber exhibiting increased effective length (L_{eff}). (blue) Power evolution in a counter pumped fiber amplifier. A rapid increase in power near the end of the fiber results in smaller effective length (L_{eff}).

In the counter-pumping configuration a reduction in L_{eff} is realized. The effective length is a qualitative metric used to describe the change in signal power over the length of the fiber. The change in signal power along the length of the fiber, $\Delta P/\Delta z$, is larger in the counter-pumped amplifier. Qualitatively, this tends to increase the SBS threshold because a shorter length of fiber core is subject to high signal power. This technique alone can increase the SBS threshold by a factor of 2.

1.6.3. Temperature and Stress/Strain Gradients

The final term in Eq. (1.1) to be examined is $g_{B,\text{eff}}$, the Brillouin gain coefficient. Eq. (1.2) shows the effective Brillouin peak gain frequency is temperature dependent. The mechanism by which this shift is achieved corresponds to a thermal dependence of the acoustic velocity in fused silica.[70] In other words, a longitudinal thermal gradient,

which tends to broaden the Brillouin gain spectrum, will simultaneously lower the effective Brillouin gain.[71] The thermal shift coefficient is typically $C_T \approx 2\text{MHz}/^\circ\text{C}$. Thus, a modest 50°C thermal gradient would double the effective Brillouin gain bandwidth to 100 MHz. This effect may also be thought of as a reduction in the nonlinear interaction length. The frequency of Stokes light generated at the “hot” end ($z = L$) of the fiber would be outside the bandwidth of the Brillouin gain spectrum at the “cold” end ($z = 0$). In many cases this thermal gradient is achieved naturally through the quantum defect heating associated with the pump absorption and subsequent stimulated emission process. Figure 10 shows the thermal gradients associated with the power evolution shown in Figure 9.

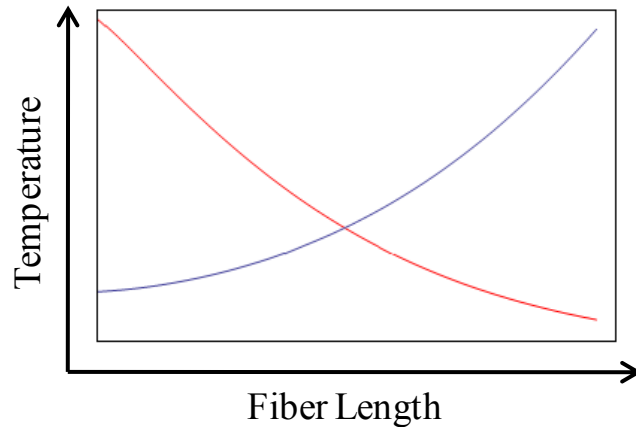


Figure 10: (red) The thermal gradient due to quantum defect heating associated with co-pumping configuration. (blue) The thermal gradient due to quantum defect heating associated with counter-pumping configuration.

The qualitative thermal profiles shown in Figure 10 are dependent on pump absorption and cooling conditions. Overall, the protective polymer cladding limits the thermal gradient. Degradation is typically seen in polymer claddings at temperatures above 150°C . The polymer coating in double-clad fibers, having a refractive index lower

than glass, is used to establish a waveguide for the pump light. Thermal degradation generally results in changes to the refractive index and absorption characteristics of the polymer. The net result is a reduction in guided pump light followed by absorption in the polymer coating and ultimately catastrophic damage to the fiber. Nonetheless, modeling and experimental demonstrations have shown reasonable thermal gradients, $T_{\max} < 150$ °C, can increase the SBS threshold by a factor of 3-4.[72]

Similarly, the Brillouin gain spectrum can be broadened by applying tensile strain or stress on the fiber.[73] Eq. (1.3) shows the peak Brillouin gain frequency depends on the acoustic velocity in the fiber core. Thus a modification to the acoustic velocity in the form of density variations due to stress or strain will tend to broaden the Brillouin gain spectrum, and reduce the effective Brillouin gain. There are few fiber amplifier results with the implementation of this technique. This is largely due to deleterious stress/strain effects on the guiding properties of the fiber. Researchers have demonstrated a 190 W single-frequency amplifier, with a 7-fold increase in SBS threshold over the non-stress/strain fiber.[74] However, beam quality results were not published, and the literature shows no continuation of the work.

1.6.4. Laser Gain Competition

The advantages of a counter-pumped fiber amplifier configuration are described as reducing the nonlinear interaction length by through dramatic growth of signal power in a short length of the gain fiber. Counter-pumping, however, it not always a practical choice for fiber amplifier design. A recently published design, based on laser gain

competition (LGC), is an elegant solution to the SBS threshold limitations imposed on co-pumped fiber amplifiers.[75] By seeding with co-propagating broadband and single-frequency signals possessing appropriate wavelengths and seed powers, the effective length of the amplifier is shortened as the single-frequency signal experiences a rapid rise at the output end of the fiber. An example of the laser gain competition scheme is shown in Figure 11.

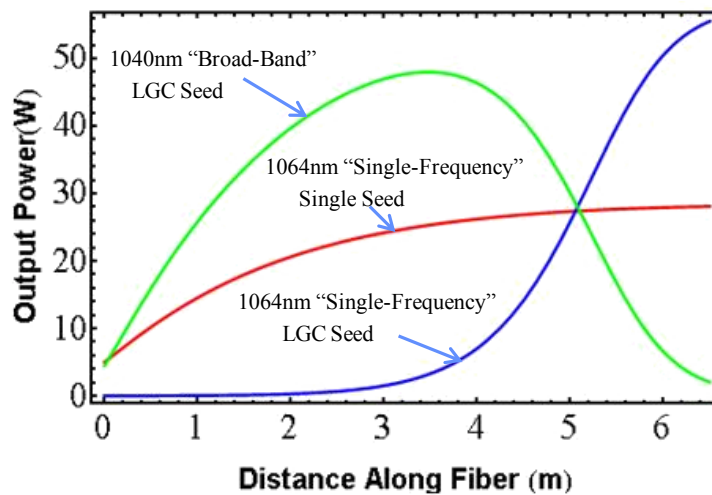


Figure 11: (green) A broadband 1040nm seed is co-propagated with a (blue) single-frequency 1064 nm seed. The amplifier is co-pumped with a 976nm multi-mode (MM) diode. The 1040nm experiences gain from the 976nm pump, and then begins pumping the 1064nm single-frequency seed. (red) The output of a single-frequency co-pumped amplifier.[76]

The single seed (red) curve and LGC seed (blue curve) are both SBS limited. The SBS suppression factor is comparable to that obtained from a counter-pumped configuration. This technique has provided a 200 W single-frequency result, limited by the available 976 nm pump power, which is the highest output power from a co-pumped fiber amplifier.[76]

1.6.5. Acoustically Tailored Fibers

The relationship between acoustic velocity and the peak Brillouin gain frequency shift (Ω_B) is shown in Eq. (1.3). Application of tensile stress or strain and temperature has been shown to broaden the Brillouin gain spectrum through a longitudinal variation in the acoustic velocity. Consider now a transverse variation in acoustic velocity. This too will tend to spread the Brillouin gain spectrum, and reduce the effective Brillouin gain through an increase in the nonlinear effective area.[77,87]. Thus the effective Brillouin gain in an acoustically tailored fiber is inherently lower than a fiber with uniform acoustic velocity. While this technique has received significant attention in the past few years, it was actually first described by Roger Stolen in 1979.[78] In that paper, Stolen posited the existence of an inhomogeneous transverse acoustic velocity profile as an explanation for increased SBS threshold measurements. SBS mitigation through the transverse manipulation of acoustic velocity received little attention for the next 25 years. Early work focused on creating longitudinal variations in the acoustic velocity profile. This was most successfully achieved by concatenating multiple fibers, having different acoustic indices, resulting in a broadened effective Brillouin gain bandwidth.[79,80] This technique is sufficient for low power delivery fibers, but reflections at splice points lead to temporal instabilities when employed in a gain fiber configuration.

The recent surge of high power narrow linewidth fiber amplifier technology brought the idea of transverse acoustic manipulation into the forefront of fiber design. Initially, work was focused on transverse acoustic profiles in single-mode cores.[81] Corning was the first group to employ this scheme in Yb-doped LMA step index fibers, in an attempt to increase the SBS threshold of single-frequency fiber amplifiers.[82]

The most challenging aspect of manufacturing acoustically tailored fibers is creating acoustic velocity gradients while maintaining optical homogeneity. This can be achieved through proper dopant selection. Table 4 shows the qualitative effect on acoustic and optical refractive index for common fiber dopants.

Table 4: Common fused silica fiber dopants and the qualitative effect on acoustic and optical refractive index. [82]

	GeO ₂	P ₂ O ₅	TiO ₂	B ₂ O ₃	F ₂	Al ₂ O ₃
Optical Refractive Index	↑	↑	↑	↓	↓	↑
Acoustic Refractive Index	↑	↑	↑	↑	↑	↓

In Table 4, note the similar effect GeO₂ and Al₂O₃ have on optical refractive index with opposite effect on acoustic refractive index. By counter-grading these two dopants Corning was able to create an acoustic gradient and maintain optical uniformity. An example of this doping profile is shown in Figure 12.

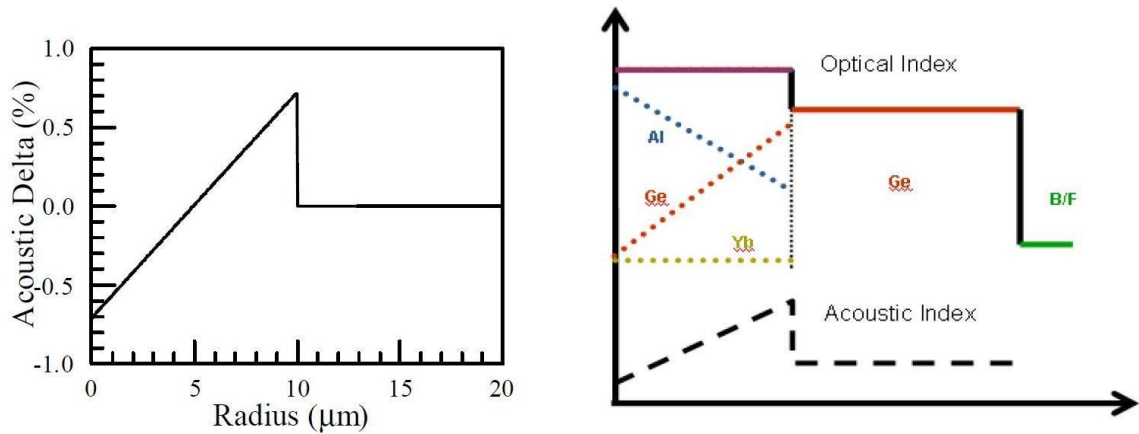


Figure 12: (left) The acoustic delta profile when the concentration of Al₂O₃ is linearly ramped down from the center of the core to the edge of the core. (right) The schematic of a double clad fiber with Yb, Ge, and Al co-doped in the core.[82]

Using this design Corning was able to achieve 500 W output power from a single-frequency fiber amplifier.[83] However, this result was obtained with a non-polarization maintaining fiber. The authors of Ref. [83] acknowledge this circumstance increased the SBS threshold, but do not attempt to quantify the improvement due to an unstable polarization state along the length of the fiber. The gain fiber was composed of a 39 μm core and 400 μm cladding (39/400). The measured numerical aperture in the core was found to be 0.05. The fiber was coiled to a diameter of 7 cm to remove higher order modes, which resulted in a beam quality of 1.4 times the diffraction limit. This beam quality result is unmatched for conventional step index fiber amplifiers with core sizes above 35 μm . Corning pushed this result to a 1 kW output power by manufacturing a fiber composed of a 50 μm core and 850 μm cladding (50/850).[84] The beam quality of this result, however, was 4.5 times diffraction limit. The authors fault an increased fiber diameter which limited minimum bend radius, thus limiting mode filtering, and inhomogeneity in the refractive index profile for the poor beam quality.

Unfortunately, Corning Inc. decided to abandon the high power single-frequency YDFA effort. Their work demonstrated increases in the SBS threshold of 3-6 dB. Other fiber manufactures have attempted to replicate the acoustically tailored designs in Yb-doped fibers, with marginal success. To date, successful results have only been achieved in fibers having core sizes less than 20 μm .[85]

1.7. Single-Frequency YDFA's: State of the Art

The power scaling results given in the previous sections were highlighted within the context of a specific method for SBS mitigation. Clearly, these results were achieved by implementing a combination of techniques. However, not all techniques work in conjunction to increase SBS suppression. The table below summarizes previous sections indicating experimentally observed suppression factors and compatibility with other suppression schemes.

Table 5: Summary of selected SBS mitigation techniques, including threshold improvement and compatibility with other schemes.

	SBS Mitigation Technique	SBS Threshold Increase (dB)	Compatibility	Notes and [Ref.]
1	Linewidth Broadening	>20	2,5	$\Delta\nu_1 \gg \Delta\nu_B$ [62,63,many]
2	Counter Pump	3	1,3,4,6	High Signal and Pump Power Localized
3	Thermal Gradient	6	2,4,5	Polymer cladding failure[86]
4	Stress/Strain Gradient	8	2,3,5	Negative effects on optical waveguide
5	Laser Gain Competition	3-4	1,3,4,6	Co-pumped Configuration only[75]
6	Acoustic Tailoring	6-11	2,5	LMA[82], 15 μm core[85]

It is difficult to generalize the compatibility and SBS threshold improvement of multiple mitigation techniques. The improvement factors are based largely on modeling correlated to experimental results. For example, it is relatively easy to “turn off” the

thermal gradient in a fiber amplifier model and characterize the improvement rendered by an individual mitigation technique. Generally speaking, it is much harder to create the experimental analog to that situation. We can, however, experimentally characterize the combination of mitigation techniques and feed this information to the model for validation. Additionally, a numerical model allows for commentary on mitigation schemes, which are not readily accessible. For example, the Corning acoustically tailored fiber is well published, but not commercially available. Note, Table 5 states the acoustically tailored fiber is incompatible with thermal or stress/strain gradients. The simple explanation for this is the Brillouin gain spectrum (BGS) bandwidth is wider than the shift achievable with a practical thermal gradient. The predicted and experimentally measured BGS full width half max (FWHM) of the fiber used in Ref. [83] is $\sim 480\text{MHz}$. [87] The maximum practical thermal gradient which may be applied to a fiber is $\Delta T \sim 150\text{ }^\circ\text{C}$. This would only provide $\sim 300\text{MHz}$ shift of the peak Brillouin gain frequency, and no significant improvement in SBS threshold.

Regardless of whether a thermal gradient improved the Corning result of 500W, it stands as the highest power ever reported for a single-frequency, single-mode, YDFA. Two comparable results were published simultaneously by a group from Southampton, UK. [88] A 402 W single-frequency, single-mode, linearly polarized YDFA was demonstrated with beam quality 1.1 times diffraction limit. Additionally, a 511 W, single-frequency, single-mode, YDFA was demonstrated with beam quality 1.6 times the diffraction limit. This 511 W result was achieved with a non-PM gain fiber, which provides an improvement in SBS threshold. Seeding an amplifier with circularly polarized light can reduce the Brillouin gain by a maximum factor of two. [78]

1.8. Summary of the Work

The results reported at the end of the last section establish the state of the art for high power, single-frequency Yb-doped fiber amplifiers, with near diffraction limited beam quality. Additionally, they serve as a benchmark by which the success of this work may be measured. The following sections of this dissertation will outline the construction and characterization of a multi-stage single-frequency photonic crystal fiber amplifier. A numerical model will be used to understand the amplifier operation, and improve its design.

Photonic crystal fiber offers two key advantages for single-frequency power scaling, when compared to conventional step index fibers: 1) core diameters beyond 30 μm , and 2) high numerical aperture pump claddings. The overall goal is to power scale this amplifier, while maintaining characteristics such as linear polarization and diffraction limited beam quality. Initially, the primary limiting factor in power scaling will be SBS. This will dictate the design, fabrication, and ultimately the successful demonstration of novel SBS suppressive fibers. In that success, new limitations on power scaling fiber amplifiers are found. A breakdown in the optical refractive index symmetry within the fiber core leads to transverse mode hopping. A power and, subsequently, temperature related threshold is experimentally demonstrated for this mode instability. Until recently, this phenomenon had not been reported in the literature. As such, a robust theoretical analysis of the issue has not been performed. To that end, a theoretical framework is presented through which the mechanisms driving the transverse mode hopping may be analyzed in future work.

CHAPTER 2

Numerical Modeling for Single-Frequency Yb-Doped Fiber Amplifiers

2.1. Overview

Fundamentally, the goal of this dissertation is the realization of high power single-frequency Yb-doped fiber amplifiers. Previous sections have proposed SBS as the primary limiting factor within the context of single-frequency fiber amplifier power scaling. The Brillouin gain coefficient is at least two orders of magnitude higher in fused silica than other relevant nonlinear optical processes, e.g. stimulated Raman scattering.[61] Thus, a successful single-frequency fiber amplifier power scaling effort requires the mitigation of SBS. To that end, an accurate theoretical description of the SBS process is required for understanding known mitigation schemes, and the development of novel techniques. Furthermore, it is of particular interest to study how multiple SBS mitigation strategies work in conjunction. Table 5 gives a generic description of compatibility between different mitigation techniques. However, upon close inspection, one can argue these compatibilities are only valid in specific fiber amplifier operation regimes. Stated more succinctly; the physical processes in fiber amplifiers, such as laser gain, temperature, stress/strain, and stimulated Brillouin scattering are interdependent.

To accurately describe the coupling between the various physical processes, a multi-physics treatment of the fiber amplifier operation is required. For the amplifiers described here, a model including, laser gain, temperature, and SBS is sufficient. The foundations for the numerical model presented here have previously been established in the literature.[75,89] A more complete theoretical treatment would be achieved by including the full treatment of wave propagation in the guided structure and would incorporate stress and strain. However, this would require a significant increase in the complexity of the model and computational time. The need for such a sophisticated treatment is avoided by assuming the fiber amplifier operates with a fundamental optical mode, which remains unchanged by stress inducing perturbations such as fiber coiling. Precedence for such an approximation has been set by previous fiber amplifier models validated with experimental results.[76] The experimental results presented in this dissertation will describe the onset of modal instabilities as the fiber amplifier output increases beyond 400 Watts. It should be pointed, however, that in order to analyze the modal instabilities, coupling to the higher order modes needs to be considered.

2.2. Stimulated Brillouin Scattering

The stimulated Brillouin scattering process, in an optical fiber begins, with the spontaneous scattering of light as it travels through the medium. The term spontaneous is applied to the scattering process under conditions such that the optical properties of the medium are not modified by the presence of the incident light.[61] In the case of Brillouin scattering, the process involves an incident photon interacting with the material resulting in the generation of a phonon and scattered photon. The forward Brillouin

scattering does not occur as it has zero frequency shift. Consequently in a fiber, only the Stokes light propagating in the opposite direction of the pump is considered. The scattering event is subject to conservation of energy and momentum, described by;

$$\Omega_B = \omega_L - \omega_S \quad (2.1)$$

$$\vec{k}_A = \vec{\beta}_L - \vec{\beta}_S \quad (2.2)$$

where ω_L and ω_S are the incident laser and scattered Stokes frequencies, respectively, and β_L and β_S are the corresponding propagation constants. The angular frequency Ω_B and the wave number k_A for the acoustic field are related via $\Omega_B = v_A k_A$, where v_A is the acoustic velocity of sound in the medium. As such, Eq. (2.1) and Eq. (2.2) can be combined to provide:

$$\Omega_B = \frac{v_A \omega_L (n_{eff,L} + n_{eff,S})}{c \left(1 + \frac{n_{eff,S} v_A}{c} \right)} \quad (2.3)$$

where $n_{eff,L}$ and $n_{eff,S}$ are the effective indices of refraction for the signal and Stokes waves, respectively. Since in the limit of weak dispersion and a weakly guiding fiber, $n_{eff,L} \cong n_{eff,S} \cong n_L$, the Brillouin shift can be approximated as $2nv_A\omega_L / c$. Using this relationship one finds the Brillouin shift at 1064 nm is approximately 16 GHz.

When the incident laser field increases in intensity, the spontaneous Brillouin scattered light grows accordingly. The incident and scattered light fields can then beat together, giving rise to density and pressure variations by means of electrostriction. This

process can be physically described by a forward travelling acoustic wave. The laser field will then scatter of the refractive index change due to the acoustic wave resulting in stimulated Stokes light. Consequently, the acoustic and Stokes waves reinforce each other and can both grow to large amplitudes. SBS is then a three-wave interaction process which requires three coupled nonlinear partial differential equations to describe it. At steady state certain simplifications are made leading to, in its simplest form, a 2×2 coupled nonlinear system of ordinary differential equations that describes the spatial evolution of the laser and the Stokes light.

2.3. Numerical Modeling of Single-Frequency YDFA's

In order to formulate this reduced system of coupled equation, one starts with the time-dependent coupled wave equations describing the photon and phonon fields. The acoustic wave is given by:

$$\frac{\partial^2 \tilde{\rho}}{\partial t^2} - \Gamma'_B \nabla^2 \frac{\partial \tilde{\rho}}{\partial t} - v_A^2 \nabla^2 \tilde{\rho} + \frac{-\gamma_e \epsilon_0}{2} \nabla^2 E_{tot}^2 \quad (2.4)$$

where $\tilde{\rho}$ is the material density, $\gamma_e = \tilde{\rho}(\partial \epsilon / \partial \tilde{\rho})$ is the electrostrictive constant, v_A is the speed of sound, and Γ'_B is a damping parameter. The right side of Eq. (2.4) accounts for the process of electrostriction. However, only the term containing the product of the laser and Stokes electric fields and oscillating at the difference frequency is pertinent to the process of SBS.

To describe the evolution of the electric fields of the laser and Stokes waves (E_L and E_S respectively), one begins with the nonlinear electromagnetic wave equations:

$$\nabla^2 E_L - \frac{n_L^2}{c^2} \frac{\partial^2}{\partial t^2} E_L = \frac{1}{\epsilon_0 c^2} \frac{\partial^2}{\partial t^2} P_L^{(nl)} \quad (2.5)$$

$$\nabla^2 E_S - \frac{n_S^2}{c^2} \frac{\partial^2}{\partial t^2} E_S = \frac{1}{\epsilon_0 c^2} \frac{\partial^2}{\partial t^2} P_S^{(nl)} \quad (2.6)$$

where $P_L^{(nl)}$ and $P_S^{(nl)}$ are the nonlinear polarizations for the laser and Stokes fields, respectively. The linear index of refraction for the laser and Stokes are n_L and n_S , respectively. Again, since the shift in frequency is ~ 16 GHz, one can make the simplification $n_L \approx n_S$ in the equations presented below.

The nonlinear polarization for the optical fields is due to the electrostriction process that drives SBS. Furthermore, these fields can undergo amplification or loss due to population inversion in a Yb-doped fiber core and this laser action can also be mathematically incorporated into the nonlinear polarization. Thus the nonlinear polarizations used in Eq. (2.5) and Eq. (2.6) are the sum of their respective SBS and laser gain polarizations.

The nonlinear polarization due to SBS can be formulated by considering the change in the dielectric constant of the medium, ϵ , as a result to the change in density. Subsequently,

$$P^{(SBS)} = \varepsilon_0 \frac{\gamma_e}{\rho_0} \tilde{\rho} E_{tot} \quad (2.7)$$

where $P^{(SBS)}$ is the nonlinear polarization due to SBS and ρ_0 is the background density.

It should be pointed out that only the terms oscillating at the laser and Stokes frequencies in the equation above are pertinent to the SBS process.

The SBS is initiated from noise, and thus the phonon field can oscillate over a range of frequencies. Furthermore, since the acoustic resonance frequency is dependent on temperature, the resonance Brillouin frequency can be a function of position. As a result, a multitude of Stokes waves oscillating at different frequencies is required to capture the SBS process in an actual high power fiber amplifier configuration. The nonlinear polarization for both laser and Stokes waves is much smaller than the corresponding linear polarizations. As such, the fields are expressed as follows:

$$E_L(\vec{r}, t) = \sum_j (1/2) A_{L,j}(z) \phi_{L,j}(x, y) \exp[i(\beta_{L,j}z - \omega_L t)] + c.c. \quad (2.8)$$

$$E_S(\vec{r}, t) = \sum_i \sum_j (1/2) A_{i,j}(z) \phi_{i,j}(x, y) \exp[i(\beta_{i,j}z - \omega_i t)] + c.c. \quad (2.9)$$

where $A_{i,j}$ represents the field amplitude of the Stokes wave oscillating at angular frequency ω_i and propagating in optical fiber mode j , $\beta_{i,j}$ is the corresponding propagation constant, and where $\phi_{i,j}$ is the corresponding transverse profile. $A_{L,j}$ represents the field amplitude of the laser propagating in optical fiber mode j , and $\beta_{L,j}$

and $\phi_{L,j}$ are the corresponding propagation constant and transverse field profile, respectively.

Large mode area fiber amplifiers operating near the diffraction limit are seeded in the lowest-order mode and are coiled to reduce excitation of the higher order modes as the wave propagates down the fiber. This is accomplished by inducing large bend losses for the higher-order modes through the proper choice of coiling radius. Thus, one can ignore coupling between the lowest-order mode and the higher-order modes. In the analysis that follows, focus will be placed on the nonlinear coupling of the laser and Stokes fields propagating in the lowest-order mode. Therefore, the subscript j is dropped from the subsequent equations, and recognized as a description of the lowest-order mode for each frequency component. Furthermore, since the wavelength separation among the waves is much smaller than the optical wavelength, the modal profiles of all waves are set to be equal, i.e. $\phi_i \cong \phi_L$.

The density can be expressed as the sum of the background density and the oscillatory part:

$$\tilde{\rho} = \rho_0 + \left[(1/2) \sum_i \rho_i(\vec{r}, t) e^{i[k_A z - (\omega_L - \omega_i)t]} + c.c \right] \quad (2.10)$$

Eq. (2.10) is now used in Eq. (2.4) in order to decouple the phonon field from the photon fields. The acoustic equation is treated in the plane wave limit wherein the diffractive term, ∇_{\perp}^2 , is neglected. Furthermore, using the slowly varying envelope approximation and $\Omega_B = k_A v_A$, one can obtain the following equation:

$$\left[\begin{aligned} & -2i(\omega_L - \omega_i) \frac{\partial \rho_i}{\partial t} - 2i v_A^2 k_A \frac{\partial \rho_i}{\partial z} + \\ & \left[\Omega_B^2(z) - (\omega_L - \omega_i)^2 - i\Gamma_B(\omega_L - \omega_i) \right] \rho_i \end{aligned} \right] = \frac{\gamma_e \epsilon_0 k_A^2}{2} |\phi|^2 A_L A_i^* \quad (2.11)$$

where $\Gamma_B = k_A^2 \Gamma'$. Since the phonons are highly damped, they propagate over short distances before being absorbed. This distance is much smaller than the distance over which the driving electrostrictive term varies significantly and consequently the term containing the spatial derivative in z is neglected. As a result the following equation is obtained at steady state:

$$\rho_i(\tilde{r}, t) = \epsilon_0 \gamma_e k_A^2 \frac{A_L A_i^* |\phi|^2}{\Omega_B^2 - (\omega_L - \omega_i)^2 - i(\omega_L - \omega_i) \Gamma_B} \quad (2.12)$$

One note concerning the neglect of the diffractive term in arriving at the equation above is that other works have included it in an attempt to formulate the SBS process in optical fibers. By doing so, guided acoustic modes are taken into account. A discussion of these modes is provided in section 3.6.3 of this dissertation.

The photon and phonon fields are decoupled by using this equation in Eqs. (2.5) and (2.6). One proceeds by applying the slowly-varying envelope approximation, $d^2 / dz^2 \ll 2i\beta(d/dz) \ll \beta_i^2$, and by using $c\beta \approx c\beta_i \approx n\omega_L$. By noting that the transverse optical profile satisfies the Helmholtz equation, the system of equations is reduced to a coupled nonlinear system of first order differential equation describing the spatial evolution of the amplitudes.

The field equations can be transformed to power equations through a multiplication with their respective field complex conjugates, A_L^* and A_i^* . It is straightforward to show that for the laser signal power, P_L , the following equation describing its evolution along the direction of propagation, z , is obtained:

$$\frac{dP_L}{dz} = \left[\tilde{g}_L(z) - \sum_i \tilde{g}_{B,i}(z)P_i \right] P_L \quad (2.13)$$

where P_i is the Stokes power, \tilde{g}_L and $\tilde{g}_{B,i}$ represent the laser and Brillouin gain, respectively. The laser gain and Brillouin gain are given by:

$$\tilde{g}_L(z) = \frac{\iint (\sigma^{(e)}N_2(x, y, z) - \sigma^{(a)}N_1(x, y, z))|\phi(x, y)|^2 dx dy}{\iint |\phi(x, y)|^2 dx dy} \quad (2.14)$$

$$\tilde{g}_{B,i}(z) = \frac{\iint g_{B,i}(x, y, z)|\phi(x, y)|^4 dx dy}{\left(\iint |\phi(x, y)|^2 dx dy\right)^2} \quad (2.15)$$

where $\sigma^{(e)}$ and $\sigma^{(a)}$ are the emission and absorption cross sections for the laser (and Stokes), respectively. N_2 and N_1 are the population densities of the upper and lower states, respectively. For a two-level system, steady state solutions for N_2 and N_1 can be readily obtained.[90] They are related to the absorption and emission cross sections, and the intensities of the pump, signal and Stokes waves through the following equations:

$$N_0 = N_1(x, y, z) + N_2(x, y, z) \quad (2.16)$$

$$N_2(x, y, z) = \frac{\frac{\omega_L}{\omega_p} \sigma_p^{(e)} I_p + \sigma^{(e)} \left(I_L + \sum_i I_i \right)}{\frac{\omega_L}{\omega_p} (\sigma_p^{(e)} + \sigma_p^{(a)}) I_p + (\sigma^{(e)} + \sigma^{(a)}) \left(I_L + \sum_i I_i \right) + \frac{\hbar \omega_L}{\tau}} N_0 \quad (2.17)$$

where $\sigma_p^{(e)}$ and $\sigma_p^{(a)}$ are the emission and absorption cross sections of the pump, respectively. N_0 represents the number density of Yb ions in the fiber core, τ is the lifetime of the upper laser level, and I_p , I_L and I_i represent the intensities of the pump, laser, and Stokes waves, respectively.

The dependence of the SBS gain on the temperature profile is dominated by the shift in the resonance frequency. It can be incorporated into $g_{B,i}(x, y, z)$ through:

$$g_{B,i}(x, y, z) = \frac{g_{B,\max}}{1 + 4 \left\{ [\Omega_B(T_0) + C_T \Delta T(x, y, z) - \omega_L + \omega_{S,i}]^2 / \Gamma_B^2 \right\}} \quad (2.18)$$

where $1/\Gamma_B$ represents the phonon lifetime, C_T is an empirical constant approximately equal to 2.0 MHz/C° that provides the shift in the center Brillouin frequency due to the temperature difference, and $\Omega_B(T_0)$ is the centerline Brillouin shift (resonance frequency) at a reference temperature, T_0 . The peak value of the Brillouin gain, $g_{B,\max}$, is given by:

$$g_{B,\max} = \frac{\gamma_e^2 \omega^2}{n v_A c^3 \rho_0 \Gamma_B} \quad (2.19)$$

Note that the variation of $g_{B,\max}$ with temperature is neglected in this analysis.

For the Stokes light which propagates counter to the signal, the evolution is given by:

$$\frac{dP_i}{dz} = -(\tilde{g}_L(z) + \tilde{g}_{B,i}(z)P_L)P_i \quad (2.20)$$

where the approximation $\tilde{g}_i(z) = \tilde{g}_L(z)$ has been made because the absorption and emission cross sections of the laser and Stokes frequencies are nearly identical.

As mentioned above, the SBS process is initiated by the spontaneous Brillouin scattering that occurs throughout the fiber. It was shown by Smith that SBS initiation from a distributed source can be approximated by injecting, near the output end of the fiber, one Stokes photon per mode multiplied by the thermal average of phonons in the orbital as described by the Bose-Einstein distribution function. [91] While the localized and distributed noise models are generally equivalent in a passive and homogeneous medium, the use of a localized noise to describe amplifiers with thermal gradients suffers from the drawback that the location of the noise is determined a priori and the dependence of the noise on temperature (and thus the position) is ill-defined. Consequently, a distributed noise source of the form $-\delta_i P_L$ is included on the right side of Eq. (2.13) and Eq. (2.20), where:

$$\delta_i(z) = \frac{\hbar\omega_{S,i}\Delta\omega \iint g_{B,i}(x,y,z)|\phi(x,y)|^4 \{\exp[\hbar(\omega_L - \omega_{S,i})/KT(x,y,z)] - 1\}^{-1} dx dy}{2\pi \left(\iint |\phi(x,y)|^2 dx dy \right)^2} \quad (2.21)$$

In the equation above, $\Delta\omega$ is the bin size defined by the difference in frequency between two adjacent Stokes frequencies. The overlap integral in the expression accounts for the spatial distribution of the optical fields.

After the inclusion of the noise, Eqs. (2.13) and (2.20) take the form:

$$\frac{dP_L}{dz} = \left[\tilde{g}_L(z) - \sum_i (\tilde{g}_{B,i}(z)P_i + \delta_i(z)) \right] P_L \quad (2.22)$$

$$\frac{dP_i}{dz} = -(\tilde{g}_L(z) + \tilde{g}_{B,i}(z)P_L)P_i - \delta_i(z)P_L \quad (2.23)$$

All amplifiers presented in this dissertation will employ a counter-propagating pumping scheme. The pump propagates in the inner cladding and is highly multi-mode. Consequently it can be treated in the plane wave limit. The spatial evolution of the pump power is given by:

$$\frac{dP_p}{dz} = -\frac{d_{core}^2}{d_{clad}^2} (\sigma_p^{(e)} \bar{N}_2(z) - \sigma_p^{(a)} \bar{N}_1(z)) P_p \quad (2.24)$$

where d_{core} and d_{clad} are the core and cladding diameters, respectively, and where \bar{N}_2 and \bar{N}_1 are the upper and lower population densities averaged in the transverse direction over the active core. The ratio d_{core}^2 / d_{clad}^2 takes into account the absorption occurs in the core only (i.e. where the Yb ions are present). The average upper population density is given by:

$$\bar{N}_2(z) = \frac{4}{\pi d_{core}^2} \iint N_2(x, y, z) dx dy \quad (2.25)$$

$$\bar{N}_1(z) = \frac{4}{\pi d_{core}^2} \iint N_1(x, y, z) dx dy \quad (2.26)$$

The number of Stokes waves (channels) launched is determined by two factors: 1) the spread in the resonant Brillouin frequency across the fiber due to the thermal gradient and 2) the resolution of the channels required to achieve numerical convergence. The former determines the range of Stokes frequencies considered. It is found that a range of $\Omega_{B,\min} - 4\Gamma_B \leq \omega_i \leq \Omega_{B,\max} + 4\Gamma_B$ and a resolution of approximately 5 MHz per channel is more than sufficient to capture the SBS process for the studies conducted in this work. As a result, approximately 100 channels were typically used for the Stokes light. Assuming the number of Stokes channels to be N , the system of equations as expressed by Eqs. (2.22), (2.23), and (2.24) is an $(N+2) \times (N+2)$ system of coupled nonlinear ordinary differential equations. This system of equations is coupled in itself to the algebraic equation for the upper state population density; i.e. Eq. (2.17). The system of equations represents a two-point boundary problem. In a counter-pumped configuration, the laser signal is known at the input end of the fiber, while the Stokes waves and the pump are known at the output end. For the Stokes waves, the value of the optical power at the output end is set to zero.

Quantum defect heating in the core provides the heat source. Assuming a negligible effect due to spontaneous emission on the amount of heat generated, the power balance equation in counter-propagating configuration takes the form:

$$Q(r \leq d_{core}/2, z) = \frac{4}{\pi d_{core}^2} \left(\frac{dP_p(z)}{dz} - \frac{dP_L(z)}{dz} \right) \quad (2.27)$$

where Q is the heat generated per unit volume. This equation neglects the effect of the Stokes light on heating. This approximation is fairly accurate as long as the ratio of Stokes light to signal light is on the order of a few percent or less. To determine the temperature as a function of position, the steady state heat equation in an isotropic medium is used. Noting that the variation of the temperature in the longitudinal direction is much smaller than that in the transverse direction, and assuming azimuthal symmetry, one can express the heat equation as:

$$-k_{th} \frac{1}{r} \frac{\partial}{\partial r} \left(r \frac{\partial T}{\partial r} \right) = Q(z) \quad (2.28)$$

The equation above is subject within the fiber to the boundary conditions of continuity of the temperature and heat flux, $-k_{th} \nabla T$, across the various regions of the fiber. The dimensions of these regions are provided in later sections. The effect of the silica bridge substructure is small and is neglected in our analysis. The following sections will show double-clad photonic crystal fibers are comprised of periodic air-hole structures which provide the basis for guiding the signal and pump light. The thermal conductivity of the air hole microstructure surrounding the core is estimated using a lumped-parameter method. [92] At the outer layer, both convective cooling subject to Newton's law of cooling and radiative cooling subject to Stefan's law are taken into account:

$$k_{th} \frac{\partial T(r=r_{outer})}{\partial r} = h[T_c - T(r=r_{outer})] + e\sigma_{st} [T_c^4 - T^4(r=r_{outer})] \quad (2.29)$$

where r_{outer} represents the outer radius of the fiber, T_c is the coolant temperature (air in most cases), h which lies in the range of 5-25 W/m²K for ambient conditions is the convective cooling coefficient (heat transfer coefficient), $\sigma_{st} = 5.67 \times 10^{-8}$ W/m²K⁴ is the Stefan-Boltzmann constant, and e is the emissivity which is approximately 0.9 for the acrylate coating. As can be inferred from the equation above, radiative cooling which is typically neglected in thermal analysis of fiber amplifiers becomes substantial as the temperature difference approaches 100 °K.

CHAPTER 3

Experimental Results and Analysis

This section is arranged chronologically, showing the development of a high power single-frequency photonic crystal fiber amplifier. The goal, aside from a presentation of novel work, is to show the deliberate and scientific approach used to address problems as they are encountered in the amplifier power scaling effort. When necessary, a theoretical analysis based on the numerical model presented in the previous section will be used to describe successful results and explain failures. The field of high power single-frequency fiber amplifiers is relatively small. Consequently, the body of literature on the subject is limited. Many of the results and subsequent analyses would most accurately be described as initial investigations. Like most initial investigations in science, the analysis may lack all of the relevant physics. When possible, attempts to provide a rigorous analysis are made. However, certain aspects of this work will require qualitative analysis based on empirical study.

3.1. Photonic Crystal Fiber

Photonic crystal fibers (PCFs) offer an attractive alternative to conventional LMA fibers for single-frequency fiber amplifier applications. Guiding in PCFs is achieved through the introduction of microstructures, typically air holes, which run parallel to the fiber axis. This leads to an ultra-low numerical aperture and exceptional guiding

properties as the effective index of the cladding can be controlled to within 10^{-5} through the proper choice of the size and arrangement of air holes. Intrinsically single mode operation PCFs with a $30\ \mu\text{m}$ mode field diameter (MFD) are commercially available. In addition, the segmented core design, which will be described later, provides a very flat optical index and gain profiles. Furthermore, very high pump cladding NAs can be achieved through the use of an air-cladding. The air-cladding is an air gap/silica strut bridge, which defines the MM pump waveguide. This air-clad design provides an effective NA ~ 0.5 - 0.6 . Figure 13 is an end-face view of a double clad LMA photonic crystal fiber.

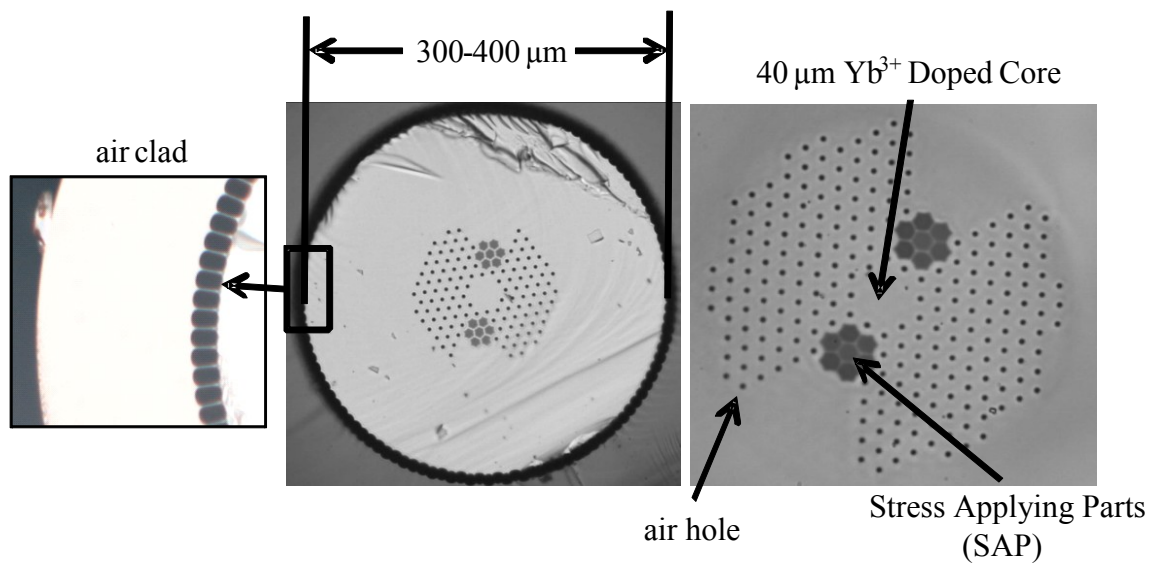


Figure 13: Microscope end-face view of various areas in large mode area (LMA) photonic crystal fiber. (left) The fused silica strut bridge defining the air clad used for guiding pump light. (center) Pump cladding dimensions range from 300-500 μm . (right) Geometry of the Yb-doped core, stress applying parts, and air hole lattice used to guide the signal mode.

In the figure, the small black dots represent an air-hole lattice, which modifies and lowers the refractive index around the core to provide guiding. The two segmented

hexagonal structures are stress inducing boron-doped glass rods for polarization maintaining operation. The black outer ring is the air-clad. Signal light is guided only in the core while the pump is confined to the larger waveguide defined by the air-clad. The core dimensions and air-hole lattice structure will be common to all PCFs presented here. The pump cladding will change within the range specified by Figure 13 (center). Additionally, the SAP's will change in successive versions of the fiber as the fiber manufacturer has modified this feature over time. The air-clad is embedded in a glass ring for protection. A polymer coating is applied to the fiber after it is drawn for protection. All fibers used in this work are made by NKT Photonics as they are the only commercial manufacturer of large mode area photonic crystal fiber in the world.

Unlike photonic band-gap fibers, the optical waveguide in photonic crystal fibers, like that shown in Figure 13, is achieved by the principle of total internal reflection. In that way, they are similar to conventional step index fibers. A primary difference between PCFs and conventional fibers is the method of fabrication. Generically speaking, conventional step index fibers are made with a process called modified chemical vapor deposition (MCVD). A preform, or large-geometry equivalent of the desired fiber, is created. In MCVD, shown in Figure 14, a silica tube rotating on a glassworking lathe is heated locally by an oxyhydrogen torch to promote reaction of SiCl_4 and, typically, GeCl_4 , POCl_3 and/or CCl_2F_2 with O_2 to produce particles of SiO_2 doped with germanium (Ge), phosphorus (P), or fluorine (F).

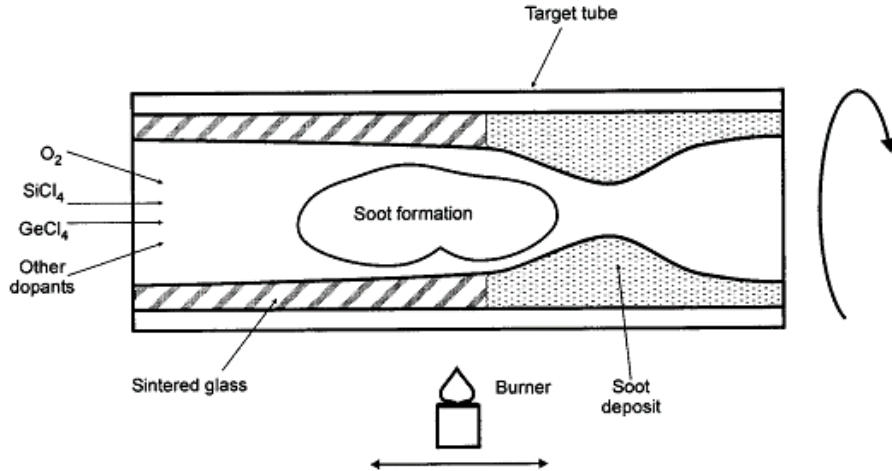


Figure 14: Modified chemical vapor deposition (MCVD) process, before the preform is collapsed. The term other dopants refers to index lower or raising dopants such as germanium, aluminum, and fluorine. The combination of gasses is heated, resulting in a chemical reaction which deposits the desired materials on the inside of the tube.

This "soot" deposits on the inner wall of the tube and is sintered into a pore-free, glassy layer as the torch traverses slowly down the tube. The result is the formation of a layer of glass of composition controlled by the composition of the gas stream. After multiple layers are deposited, the tube is collapsed to a solid rod and drawn into fiber.

[93]

Fabrication of PCF, shown in Figure 15, like in conventional fiber fabrication, starts with a fiber preform. PCF preforms are formed by stacking a number of capillary silica tubes and rods to form the desired air/silica structure. This way of creating the preform allows a high level of design flexibility. The core size and shape, as well as the index profile throughout the cladding region can be controlled. When the desired preform has been constructed, it is drawn to a fiber in a conventional high-temperature drawing tower and hair-thin photonic crystal fibers are readily produced in kilometer lengths. Through careful process control, the air holes retain their arrangement all

through the drawing process and even fibers with very complex designs and high air filling fraction can be produced. [94]

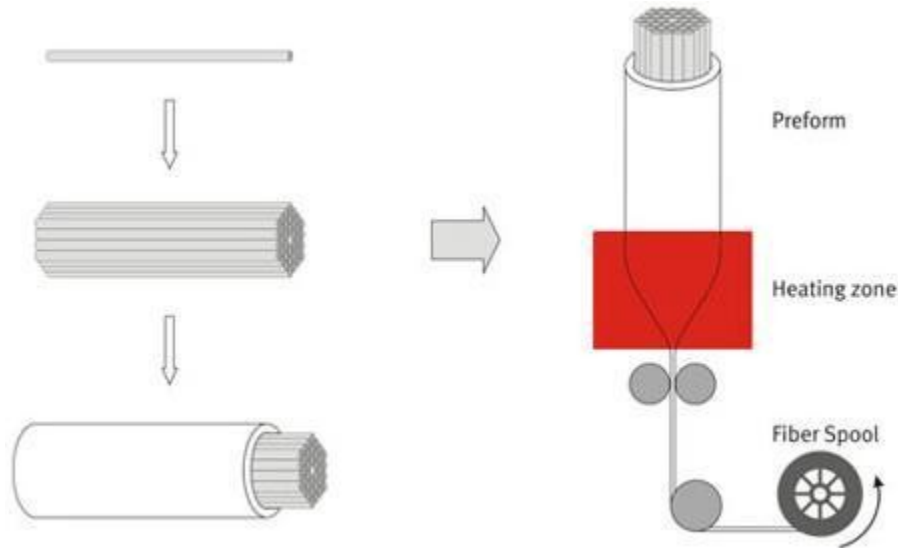


Figure 15: Stack and draw process used for photonic crystal fiber construction.

The LMA core used in this work is composed of 7 individually doped rods. The core and stress rods have cylindrical geometry in the preform but naturally take on a hexagonal symmetry when the fiber is heated and drawn, as this is the tightest arrangement. The 7 doped core rods are initially manufactured by the MCVD process. NKT photonics then takes a set of doped glass rods and homogenizes them with a proprietary technique. For example, if the goal fused silica core rod should contain 1.0 wt% germanium, 0.5 wt% ytterbium, and 0.3 wt% fluorine; individual fused silica samples, containing only one of the desired dopants, are combined to give the desired concentrations. In this way, NKT can create uniformity in doping profile and build a composite core.

3.2. Fiber Processing

All of the PCF amplifiers demonstrated in this work are “free-space-coupled”, meaning the seed and pump are coupled into the waveguide using free space optics. The fiber manufacture will provide a spool of fiber, which is generally much longer than needed for a single fiber amplifier. Subsequently, the fiber requires some preparation before it can be used as the gain medium for an amplifier. Typically these processing steps are performed on the ends of the fiber to create optical quality surfaces. The basic laboratory functions needed for this preparation are cleaving, polishing, and endcapping. The primary considerations for all end-face preparations are cleanliness and surface quality. The goal is to create fiber amplifiers generating hundreds of Watts of power, emitted from a 40 μm waveguide. A speck of dust can lead to catastrophic damage.

3.2.1. Fiber Cleaving

Cleaving is generally performed to create flat surface at the fiber face. This is achieved by placing a section of the fiber under tension and scribing the side of the fiber with a diamond or carbide blade. The tiny crack created by the blade induces a shock wave in the fiber, which is enhanced by the application of tensile stress. The result, if done properly, is a truly pristine surface, i.e. free of environmental contaminants, of excellent optical quality. In fiber amplifiers, it is generally undesirable to have a flat cleaved end-face as it increases the potential for Fresnel reflection back into the core. The preferred arrangement is to create an angled end-face, such that reflected light is not guided by the core. Angle cleaving the fiber is achieved by placing the fiber under

tension and rotating one end with respect to the other. This causes the crack, induced by the cleave blade, to follow the stress gradient created by twisting the fiber. Reasonable quality surfaces are achieved by this process if end-face angles do not exceed 10° .

3.2.2. Fiber Polishing

Often, cleaving is not an effective means for producing high quality end-face surfaces. For example, the air-hole structures used in the PCF significantly dampen cleave-induced shock waves. This leads to irregularities in the end-face surface, which are often not reproducible. Precise control of the end-face surface and angle can be achieved by polishing. This process begins by creating a facet with a large grit (e.g. 30 μm) aluminum oxide or diamond-coated lapping film. Diamond-coated lapping films have been found to provide the best quality surface, where the oxide leaves a residue that is difficult to remove. Once the facet is created, the lapping film grit is stepped down to $\sim 0.1 \mu\text{m}$. Of specific consideration in this process is the fact that PCF's contain air-holes which tend to wick polishing lubricants, or collect debris created during the polish. For this reason, the PCF must be endcapped in some way before the polishing process.

3.2.3. Endcapping

The conventional thought process behind endcapping is the reduction of energy density incident upon the fiber facet at the output of the amplifier. This is achieved by fusion splicing a piece of pure fused silica to the output of the amplifier. The endcap

allows a high power optical mode to diverge out of the fiber waveguide, and exit the amplifier with reduced intensity at the glass/air interface. Again, the difficulties in processing PCFs are realized in that heating the fiber to the melting temperature of fused silica causes the air-hole structures to collapse due to surface tension. Figure 16 shows examples of a thermally collapsed and endcapped PCF.

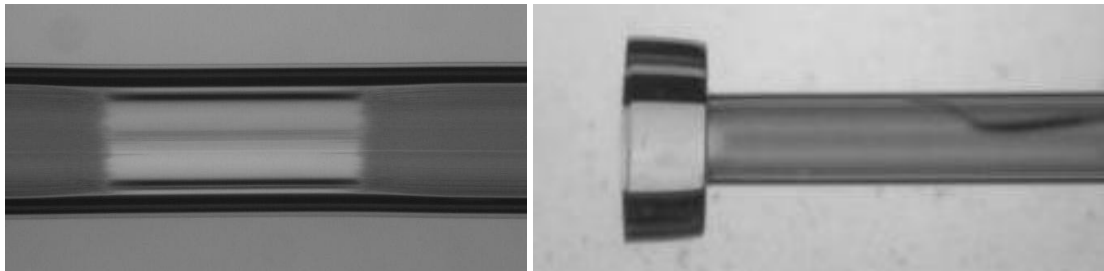


Figure 16: (left) Thermally collapsed PCF. The clear section in the center has been collapsed by heating the fiber to the fused silica softening temperature. Sections on the right and left are un-collapsed regions, which were not subject to significant heat. (right) PCF with 560 μm diameter endcapped with 1.3mm pure fused silica.

Fortunately, this collapsed region provides a solid fused silica structure which may be cleaved and/or polished. The collapsed region may be used as an endcap. It should be noted, however, that the best possible situation for endcapping a PCF is to limit the collapsed air hole region as much as possible. Figure 16 (left) shows a PCF that has been thermally collapsed. The air hole lattice in the PCF defines the seed laser signal waveguide similarly a thin ring of air holes defines the pump waveguide. Once the air hole lattice is gone the light refracts out of the core. If the air hole lattice is collapsed too far down the fiber the signal light will refract into the stress rods giving a poor beam quality (if on the output side) or poor seed coupling (if on the input side).

3.3. PCF Amplifier Construction

The high power single-frequency PCF amplifier is really the last of a multi-stage fiber amplifier system. While fiber amplifiers do provide significant gain, there are limiting factors. The most important consideration is mitigating amplified spontaneous emission (ASE). Section 1.4.2 shows the Yb-doped silica emission cross-section in the 1030-1040 nm region is much larger than the desired 1064nm operating wavelength. This imposes well known limitations on the amount of gain achievable in the amplifier while maintaining temporally stable output. ASE typically leads to self pulsation and ultimately catastrophic damage to the end-face of the fiber. An extreme scenario is pumping the fiber with 976nm light with no seed light to saturate the gain. Typically, 10-20 W of pump is sufficient to cause self-pulsations and blow the core out of the fiber end-face. For the sake of brevity, results from these types of experiments will not be discussed. Suffice it to say, the effect is easily reproducible. A “rule of thumb” linear gain factor G of 20-30 for robust operation is used, where $G \sim e^{gL}$. It should be noted however, larger gains have been reported. [88] This rule is specific to my work with photonic crystal fiber amplifiers, and based on my experiences. The seed source for these experiments is a NPRO with ~30 mW output power and linewidth less than 50 kHz. Using this thumb-rule, a 3-stage amplifier was constructed, to be used as a seed source for the PCF amplifier.

3.3.1. Seed Amplifier

The composite three stage seed amplifier is in a monolithic, co-pumped configuration. The term monolithic refers to the fact that all three stages are fusion spliced together, requiring no free space optics. Individual stages of amplification are separated by a fiber-coupled optical isolator. The isolator protects preceding stages from ASE or SBS travelling in the backward direction. A three-stage MOPA configuration and major components in the final stage of amplification are shown in Figure 17.

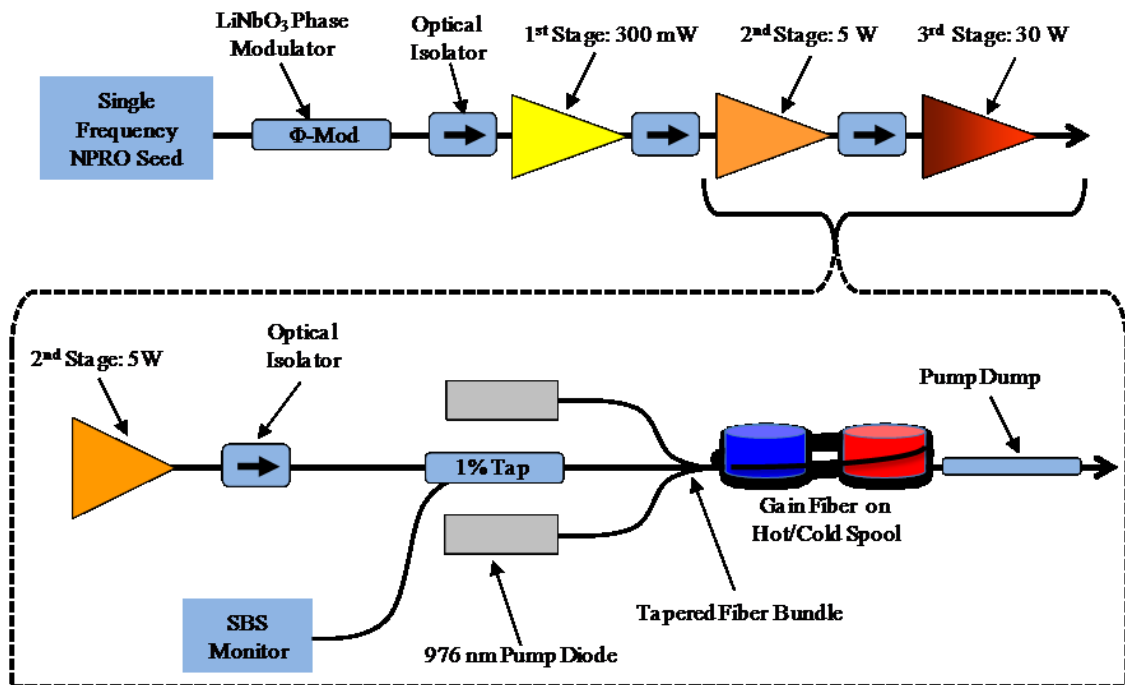


Figure 17: (top) Three stage MOPA configuration showing the progression of power amplification. (bottom) The final stage of amplification highlighting the relevant components used in monolithic amplifiers. The hot/cold spool imposes a step thermal gradient for SBS suppression.

The first two stages of amplification are similar in construction to the final stage shown in Figure 17. A LiNbO₃ electro-optic phase modulator is inserted into the system for linewidth broadening, if necessary. The 1% tap is an all fiber component which

samples the light traveling in the core. It is used to characterize forward and backward light. The tapered fiber bundle (TFB) is an all-fiber component which allows the combination of multiple fiber coupled pump diodes into a single fiber. Additionally, the TFB has a feed through double-clad fiber with similar geometry to the gain fiber. This component is spliced to the double-clad Yb-doped gain fiber. The two pump diodes produce a total output of ~70 W at 976 nm. In this configuration the seed and pump are co-propagating in the gain fiber. Power handling of the TFB precludes a counter-pumping configuration. This is a fundamental limitation inherent in the monolithic amplifier design. As such, SBS is a consideration in the final stage of amplification. A polarization maintaining, LMA, Yb-doped gain fiber ~5 meters in length is used. The fiber has a 25 μm core and 400 μm pump cladding. It is coiled to a 10 cm diameter for suppression of higher order transverse modes. Additionally, a simple step thermal gradient is used to reduce the nonlinear effective length of the fiber to half its value at a uniform temperature. The amount of fiber in the “hot” and “cold” spools is dictated by fiber length and signal power evolution along the length of the fiber. Typically, a ratio of 3:1 provides the best SBS suppression. This SBS suppression technique is only required for the final stage. Previous stages operate at power levels far below the nonlinear threshold. The final component is a pump dump, which removes unused pump power from the cladding. This is achieved by embedding the bare fiber in a UV cured epoxy. The epoxy has a larger refractive index than glass; thus light in the cladding is refracted out of the pump waveguide. A characterization of output power from the final stage amplifier of the seed system is shown in Figure 18.

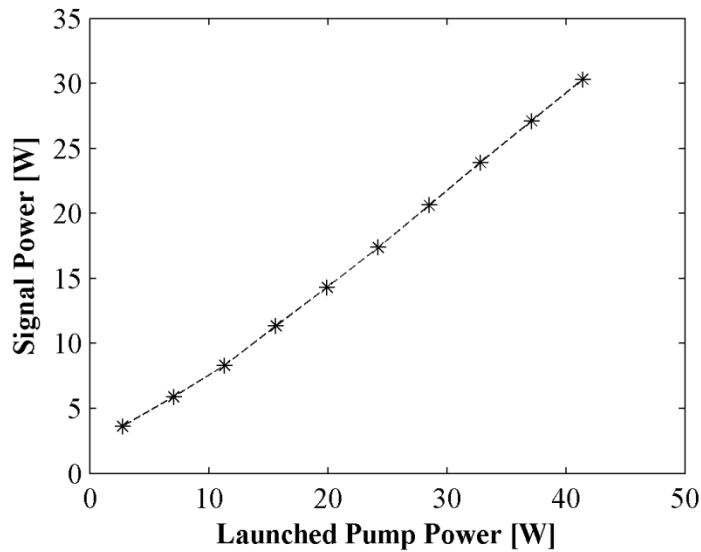


Figure 18: Final stage amplifier of the seed system with ~30W of output power.

The seed amplifier demonstrates approximately 70% optical to optical slope efficiency. Beam quality is measured to be 1.1 times the diffraction limit. The polarization extinction ratio (PER) is greater than 14 dB. These are the characteristics associated with the output of the amplifier before it is implemented in the high power PCF system.

3.3.2. High Power 976 nm Diode Pump and Characterization

The photonic crystal fiber amplifier is counter-pumped by an array of single emitter diodes coupled into a 600 μm MM delivery fiber, manufactured by Laserline GmbH. Maximum output power of the laser system is 1.5 kW. The laser is equipped with an internal cooling system, used for heat removal from the diode stack. An external water source, supplied by the user, removes waste heat from the internal cooling system via a plate heat exchanger. The external water flow is modulated by a solenoid, which

regulates heat removal from the internal cooling system. Two cooling conditions are available for the laser system. A fixed temperature can be set by the user, and the solenoid will automatically regulate external water flow in an attempt to maintain that setting. Alternatively, there is a thermally controlled wavelength stabilization option. Laserline characterizes the power, temperature, and wavelength at the factory. This information is used to dynamically control the diode temperature as a function of output power. The figure below shows how the shift in center wavelength is thermally tuned as a function of output power, obtained with an optical spectrum analyzer and power meter.

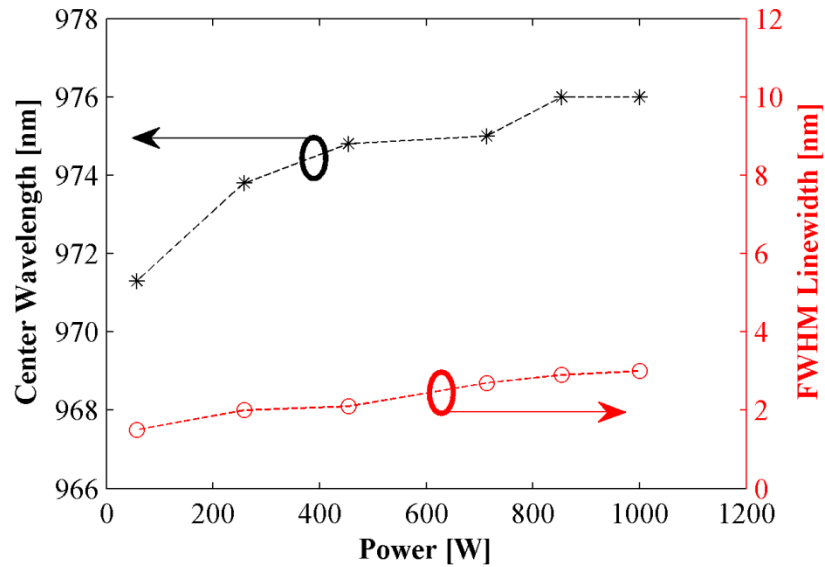


Figure 19: Wavelength characterization of Laserline diode pump. The wavelength stabilization setting fixes center wavelength near the peak absorption for Yb-doped fiber. The FWHM is approximately the same size as the 976 nm absorption bandwidth of Yb-doped silica.

The set temperature of the diode ranges from 40 °C at low power to 20 °C at high power. The set temperature changes automatically with drive current. The FWHM of the laser scales slightly with increasing power, but is on the order of the peak absorption bandwidth found in Yb-doped silica fibers. The central wavelength control and relatively

narrow spectral bandwidth allow for very efficient pump absorption in the fiber. Figure 20 shows a characterization of the output power.

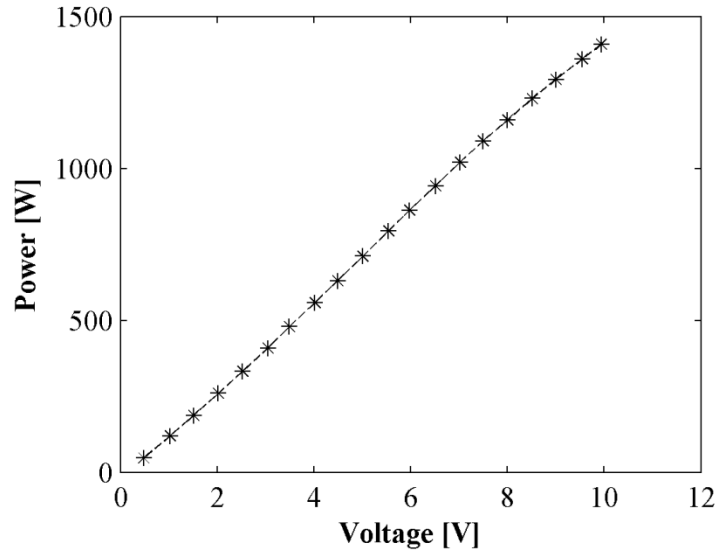


Figure 20: Output power of Laserline diode laser as function of drive voltage.

The output power shown above is limited to 1.4 kW. This is in part due to the optics used to couple the pump laser into the PCF amplifier. In an effort to exploit the high numerical aperture characteristic of air clad PCFs, coupling optics are chosen to give a $\sim 250 \mu\text{m}$ spot size. The $600 \mu\text{m}$, 0.2 NA, delivery fiber is collimated with a 100 mm focal length (FL) lens. The collimated beam travels through a dichroic mirror, used to reflect the counter-propagating 1064 nm signal light, and is focused with a 40 mm focal length (FL) lens. The lens separation is approximately 10 cm.

3.3.3. Free Space Photonic Crystal Fiber Amplifier Setup

The seed and pump establish the beginning and end of the high power PCF amplifier. Figure 21 shows the general experimental setup used.

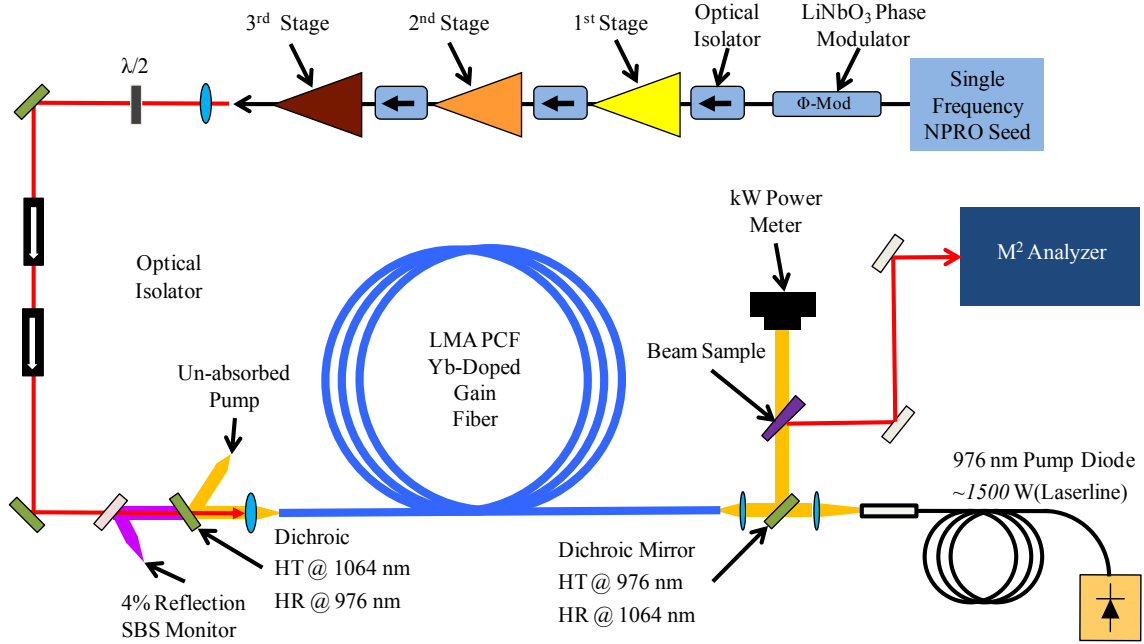


Figure 21: Experimental setup for counter-pumped PCF amplifier.

The output of the three-stage seed amplifier is collimated and then propagated through two free space optical isolators. These free space components impose ~ 1.4 dB loss to the seed amplifier output power. A lens is used to image the seed amplifier output core into the PCF core, and collimate un-absorbed pump light. Special care is taken to pick collimating and focusing lenses which will best mode match the seed core to the PCF core. A simple Gaussian beam optics model was written in Mathematica to find the best lens pairs. The seed amplifier core has a MFD $\sim 22\mu\text{m}$, and the PCF core has MFD $\sim 30\mu\text{m}$. Typical lens pairs are FL=40mm for collimation of the seed and FL=60mm for mode matching the PCF core. This configuration calls for a lens separation of ~ 3 m.

Coupling efficiencies of 80% are achievable with the appropriate lens configuration. The PCF amplifier output is collimated by the focusing lens used in the pump coupling optics and a dichroic mirror is used to separate the 1064 nm signal light. The beam is sampled for analysis, e.g., M^2 , linewidth measurements, PER, etc. The majority of signal power is measured with a thermopile power meter.

3.3.4. Measurement Notes

The SBS threshold and beam quality metric, M^2 , will be used often to characterize the performance of various amplifiers presented here. A brief description of each measurement will be given for clarification.

The M^2 factor is defined as the space-beamwidth product for a given laser beam divided by an ideal Gaussian space-beamwidth product.[95] While the fundamental mode of any cylindrical waveguide, including the PCF, is not characteristically Gaussian, it is a very good approximation. Additionally, the paraxial approximation is used when considering beam divergence. In simple terms, the space-beamwidth product is the minimum spot size (w_0) multiplied by the far field divergence of the beam. The two quantities are rigorously defined as the spatial variance (σ_{x0}) at the beam waist and spatial frequency variance (σ_s). Eqs. (3.1) and (3.2) show the variances for the ideal Gaussian beam and the resulting space-beamwidth product (BP_{ideal}).

$$\sigma_{x0}(z) = \frac{w_0}{2}, \sigma_s = \frac{1}{2\pi w_0} \quad (3.1)$$

$$BP_{ideal} = \sigma_{x0} \sigma_s = \frac{1}{4\pi} \quad (3.2)$$

Due to the Fourier transform relationship between spot size and divergence angle characteristic of Gaussian beams, a real laser space-beamwidth product (BP_{real}) can be written as,:

$$BP_{real} = \sigma_{x0} \sigma_{sx} = \frac{M_x^2}{4\pi} \quad (3.3)$$

The resulting spot-size propagation formula for the real laser beam is, [95]

$$w_x^2(z) = w_{x0}^2 + M_x^4 \left[\frac{\lambda^2}{\pi^2 w_{x0}^2} \right] (z - z_{x0})^2 \quad (3.4)$$

where z_{x0} is the position of the minimum spot size. The equations above describe measurement made in the x-axis. Typically, a composite value of M^2 is quoted which contains beam characteristics in two orthogonal directions. The experimental setup for such a measurement involves collimating the output of the laser and propagating the beam to a long focal length lens. Measurements of the beam waist are made at various positions (z) after the focusing lens. The M^2 parameter is optimized to fit a theoretical line to the beam waist vs. propagation direction (z) data. The International Organization for Standardizations ISO Standard 11146 requires at least 10 beam waist samples be

taken for an accurate M^2 measurement. A minimum of 5 samples are taken near the beam waist, and 5 taken beyond the Rayleigh range.

The SBS threshold is another metric which requires some discussion. In a passive optical fiber, it is relatively simple to define the SBS threshold experimentally. Consider a single-frequency CW laser coupled into a passive optical fiber with low intrinsic loss. As the laser power is increased, the fiber will continue to transmit the coupled light until a critical power is reached. Any laser power coupled into the fiber beyond that critical power will be reflected in the backward direction as Stokes shifted SBS light. Figure 22 is experimental data representative of this situation.

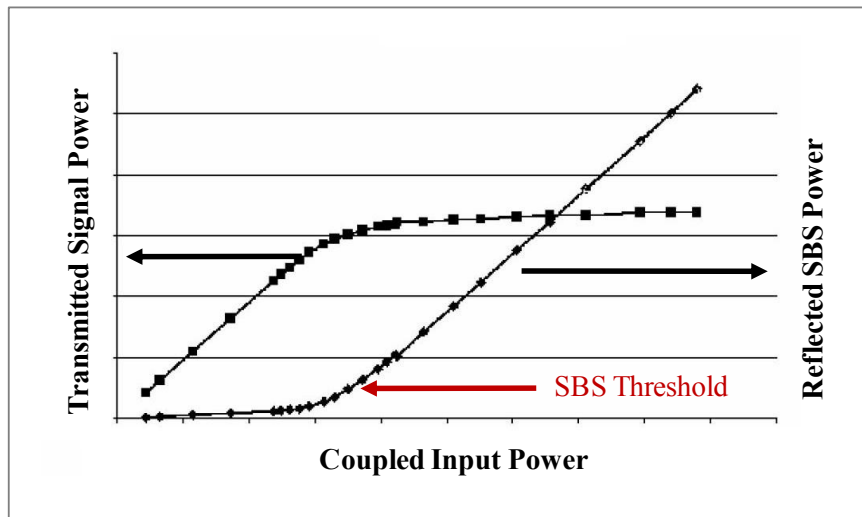


Figure 22: Transmitted signal in a passive fiber measured beyond the stimulated Brillouin scattering threshold. A single-frequency laser is coupled to a single-mode. The coupled laser power is pushed well beyond the SBS threshold.[96]

For purposes of discussion in this dissertation, the backward travelling power is considered to be composed only of Rayleigh scattered light and Brillouin scattered light. Realistically, there will always be other contributions to the backward travelling light,

e.g. Fresnel reflections from the fiber output and amplified spontaneous emission (ASE). In principal, these issues may be mitigated through proper fiber preparation and sufficient saturation of the gain media. Therefore, only contributions from Rayleigh and Brillouin scattered light are considered significant. Rayleigh scattering scales linearly with optical power, [97] while Brillouin scattering increases exponentially with optical power. This allows for a qualitative definition of the SBS threshold. The threshold is reached when the measured backward power departs from a linear relationship with increasing signal power.

Unfortunately, fiber amplifiers do not allow for experimental results such as those shown in Figure 22. The addition of laser gain makes the SBS process temporally dynamic. The backward travelling Stokes light is subject to Brillouin gain and laser gain. Near the SBS threshold, the Stokes light is comparable to the signal light. In this situation, the Stokes light tends to rob the forward traveling signal light of laser gain, leading to a reduction in signal output power. As a result, the generation of Stokes light is reduced. The consequence of this process is a relaxation oscillation in output power, occurring on a time scale comparable to the round-trip time in the fiber, and manifesting as a series of high energy pulses. Typically these pulses lead to catastrophic damage to the amplifier, and/or surrounding components. Therefore, it is of extreme importance to correctly characterize the backward power in single-frequency fiber amplifiers. A reflectivity (R) can be calculated if it is possible to estimate the total backward power, as shown in Figure 23. Reflectivity is defined as total backward power divided by total signal output power. In practice, a reflectivity of 0.01% is close to the SBS threshold.

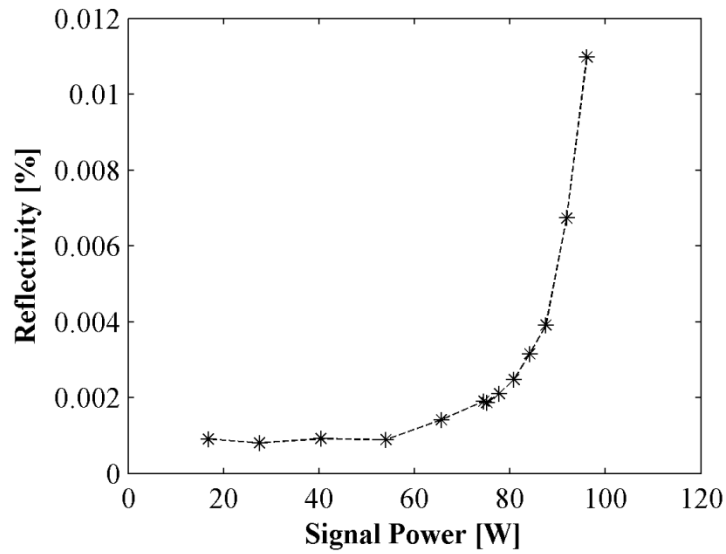


Figure 23: Reflectivity vs. signal output power for fiber amplifier near SBS threshold. The departure from linear increase in backward power occurs in a very narrow window of output power.

Additionally, a high resolution optical spectrum analyzer (OSA) can be used to compare the ratio of Rayleigh scattered light to Brillouin scattered light. The Rayleigh scattering light possesses the same frequency as the signal and the Stokes light is downshifted by approximately 16 GHz due to SBS. Figure 24 is an example of a backward power spectrum taken from an amplifier near SBS threshold.

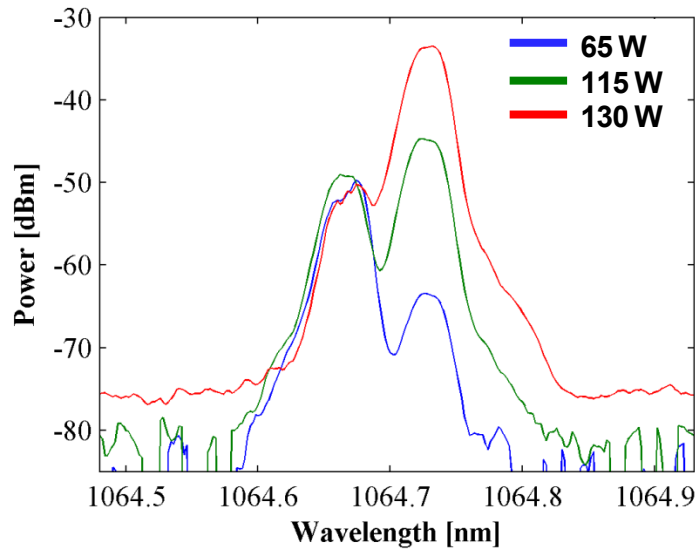


Figure 24: Optical spectrum analyzer (OSA) data measured from backward traveling light of single-frequency fiber amplifier at three output power levels (65 W, 115 W, 125 W). The OSA resolution limit is ~ 1 GHz, the separation between the SBS and Rayleigh peaks is approximately 16 GHz (0.06 nm).

The y-axis in Figure 24 is logarithmic, thus the Stokes light is dominating the backward power measurement at the highest signal output power of 125 W. This OSA spectrum would correspond to a departure from linearity in the backward power measurement. There are a number of ways to characterize the backward power from an amplifier. The combination of reflectivity and OSA measurements has proven to be sufficient for safe operation, while benchmarking improvements in SBS threshold.

3.4. PCF Amplifier Power Scaling

The experimental effort in PCF amplifier power scaling began with fiber and laser diode pumps inherited from a previous project at the Air Force Research Laboratory (AFRL). Fiber quality and laser diode reliability were an issue in the initial power

scaling demonstrations. Over time, a dialogue was developed with the fiber manufacturer which resulted in improved fiber designs. Refinement of the manufacturing process and novel SBS suppressive fiber designs allowed for further power scaling. The pump laser was also replaced with the system described in section (3.3.2).

3.4.1. Single Frequency Power Scaling: First Result

The fiber used in these experiments had a MFD $\sim 28 \mu\text{m}$, pump cladding $\sim 400 \mu\text{m}$, and outer diameter of $600 \mu\text{m}$. The pump absorption for this fiber was 2.5 dB/m at 976 nm . Researchers at AFRL worked with NKT Photonics in an attempt to design a fiber having a flattened optical mode. The design called for a modification to the air-hole lattice surrounding the core. The goal was to reduce SBS in the fiber by reducing peak intensity. Figure 13 is an end-face view of the fiber. At the time these results were achieved, the seed amplifier was composed of two stages, with a maximum output power of 10 W . Aside from the seed amplifier and available pump power, the basic design of the experimental setup is accurately described by Figure 21. A summary of results is presented below.[89]

The pump laser operated near 976 nm , with a 10 nm FWHM linewidth. The fiber was 6 meters in length and was coiled at a diameter of 40 cm . In order to evade thermal damage, a small portion of the fiber at the signal output end was inserted inside a water cooled chuck. Dichroic mirrors on both ends of the fibers were used to separate the pump and signal beams. The fiber ends were sealed by thermally collapsing the air holes and then polished to an angle of 8° to avoid parasitic oscillations. At a maximum launch

power of approximately 490 W, the signal was measured at 260 W with an ASE suppression of better than 35 dB. The broad linewidth of the pump laser provided very inefficient absorption, leading to the excessive pump power necessary for significant signal gain. The output signal power with respect to the launched pump power is shown in Figure 25. The slope efficiency, calculated by estimating absorbed pump power, was approximately 74%. The PER was measured with a half-wave plate and a polarizing beam splitter and was found to be better than 18 dB. However, PER wander was easily induced by external perturbation of the fiber. In order to characterize the SBS process in the fiber, we monitored the back-reflected light. An OSA was used to track the increase in the Rayleigh scattering light which possesses the same frequency as the signal and the Stokes light which is downshifted by approximately 16 GHz due to SBS. The Stokes light exhibited a linear increase as a function of the output signal throughout the measurements, which indicated that the amplifier was operating below threshold. The spectrum of the backward propagating light was also recorded at various powers. At the highest output power, the spectrum was dominated by Rayleigh scattering.

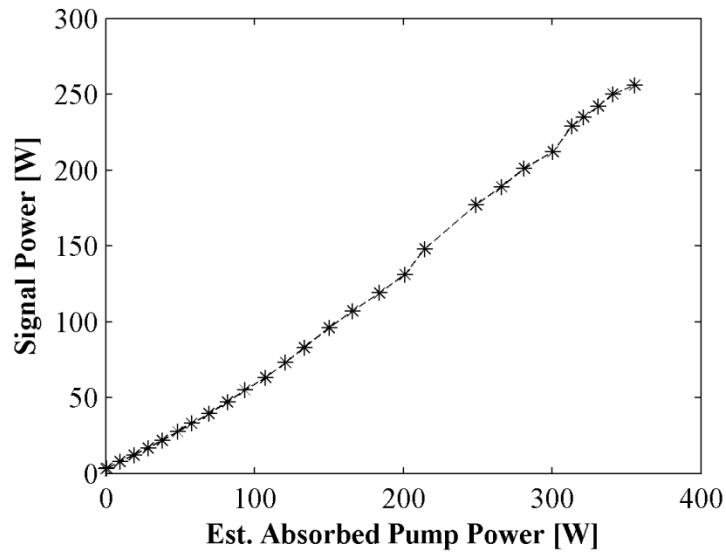


Figure 25: Single-frequency PCF amplifier with output of 260 watts showing slope efficiency of 74%.

Beam quality measurements were made using a Spiricon M^2 beam analyzer. The values of M^2 were measured to be in the range of 1.2 and 1.3 depending on the measuring axis and output power. A plot of the beam profile from one set of measurements is shown in Figure 26.

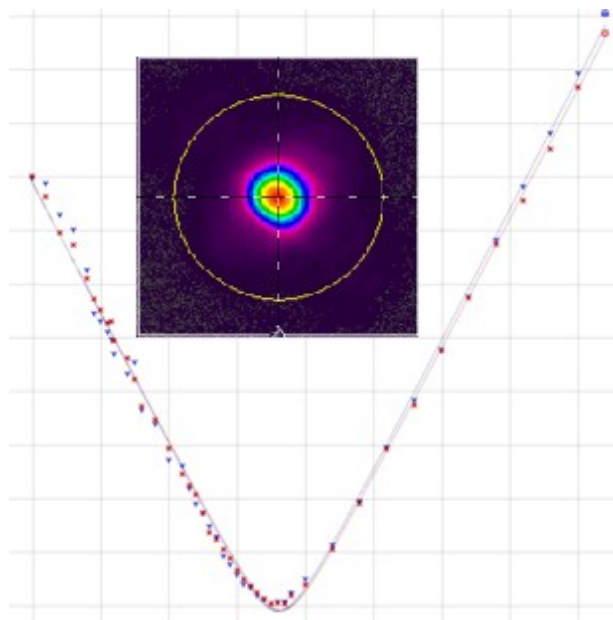


Figure 26: Beam profile and measured M^2 value at 200 W output power.

Measurements to determine the linewidth at output power levels of 32 W and 54 W were conducted. An optical heterodyne analysis, as shown in Figure 27, was used for these measurements. In the experimental setup, an NP Photonics single-frequency fiber laser with a nominal linewidth of approximately 1 kHz was used as a reference or local oscillator (LO), and was tuned appropriately. The signal from the PCF amplifier was combined with the reference beam using a 3dB fiber splitter that delivered the interference signals to two ports. One port was input to a photodetector that generated an electrical tone. The second port was input to an optical spectrum analyzer (OSA). Note that the frequency of the reference beam is tuned just lower than the average frequency of the signal in order to generate a beat frequency. The heterodyne mixing product is the convolution of the two lasers.

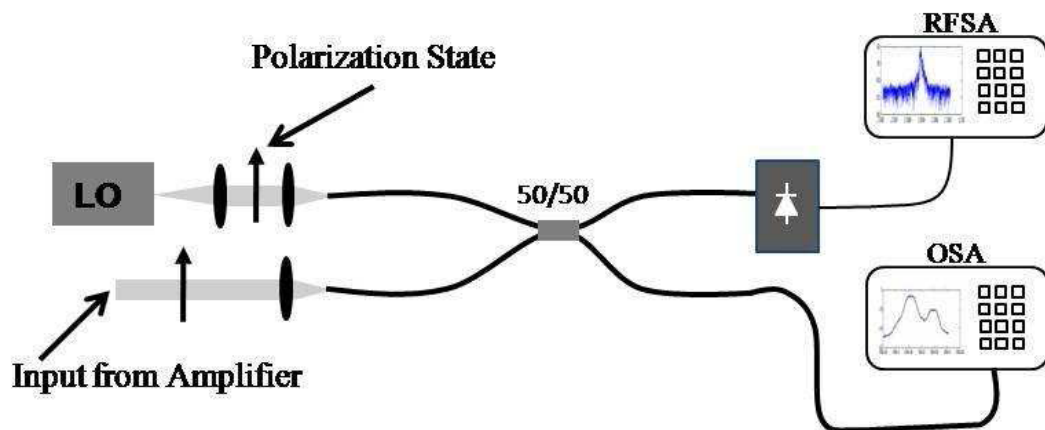


Figure 27: Experimental set-up for optical heterodyne analysis.[89]

The data for an optical heterodyne measurement is shown in Figure 28 for the 32 W output case. This data was taken in the dB scale. A Lorentzian was fit to this data as shown in the figure. The frequency scan range was approximately 300 MHz and thus the

data presented in Figure 28 zooms in on the most relevant region. Frequency jitter due to the random change in the frequency of the laser over time tends to increase the effective linewidth obtained through this technique.

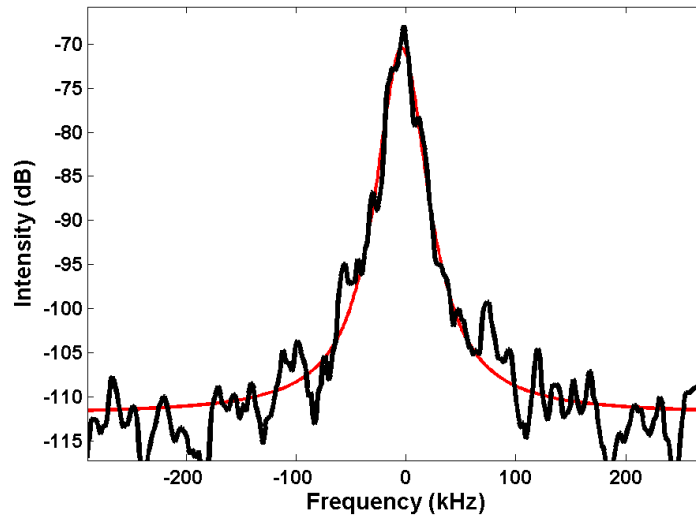


Figure 28: Optical heterodyne power spectrum for a signal output power of 32 W.[89]

One consideration with this measurement was the signal to noise ratio.

Measurements below -20 dB generated a fairly appreciable increase in the noise level. As a result, the linewidth is estimated by taking the average value of the corresponding linewidths at two measured full-width points of -10 dB and -20 dB.[98] This provided a linewidth value of 8.2 kHz. Because of the frequency jitter, this measurement was resolution limited and indicated a linewidth of <8.2 kHz. A similar analysis for the 54 W case, provided a linewidth of <6.8 kHz. Therefore, both measurements indicate single frequency operation.

The power scaling result above was pump limited, due primarily to the broad linewidth of the pump laser. At the highest power of 260 W, nearly 130 W of unused

pump light was measured. The absorption bandwidth of Yb-doped glass is ~ 2 nm at 976 nm, thus the broad pump laser bandwidth leads to extremely inefficient absorption. The pump laser described in section 3.3.2 was procured before progress in power scaling continued.

3.4.2. Narrow Linewidth PCF Amplifier

The same fiber used for single-frequency power scaling above was implemented in a narrow linewidth fiber amplifier. Improvements were made on the seed amplifier with the addition of a third stage, as shown in Figure 18. In an effort to de-couple nonlinear limitations from amplifier design issues, the single-frequency seed laser was phase-modulated to broaden the linewidth. A simple sine wave function was used to drive the LiNbO_3 phase modulator. The function generator produced a 1 GHz sine wave with ~ 1 V peak-to-peak amplitude. The voltage required for a 180° phase shift in the electro-optic modulator was ~ 1.7 V. Thus, the linewidth broadening was not ideal, but provided sufficient suppression of SBS.

The goal in this experiment was to investigate issues related to raw power scaling of PCF amplifiers. Since the intent is to build a high power single-frequency amplifier. An investigation of pure power handling capability is a logical first step. A typical result from the narrow linewidth PCF amplifier is shown below.

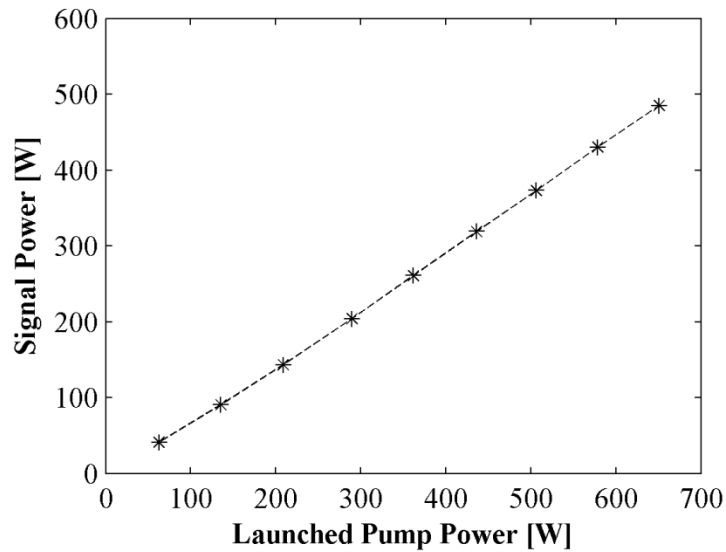


Figure 29: Photonic crystal fiber (PCF) amplifier output power with phase modulated, narrow linewidth seed.

The gain fiber length was 7 meters, coiled to a diameter of 50 cm. The total coupled seed power was approximately 12 W. The fiber was left suspended in air to maximize the thermal gradient potential of quantum defect heating, as this would be the preferred arrangement for the single-frequency amplifier. The slope efficiency was approximately 76%. It should be noted, the x-axis in Figure 29 is “Launched Pump Power” while the absorbed pump power is estimated in the result shown in Figure 25. Nearly all launched pump light was efficiently coupled, and subsequently absorbed by the fiber. While the output power is impressive, the mode quality degraded significantly above 400 W. Figure 30 is an example of the beam profile at high power.

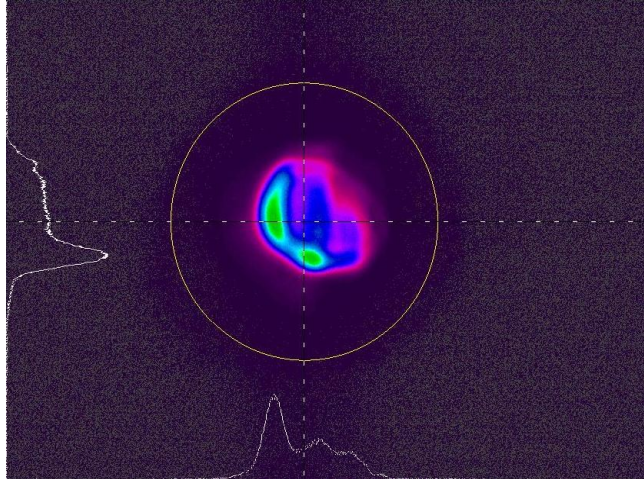


Figure 30: Photonic crystal fiber (PCF) amplifier beam profile at power level above 400 W.

The beam quality associated with Figure 30 is $M^2 \sim 4$. Clearly, there are beam quality issues as power is increased. At lower powers, the beam quality was found to be much closer to single-mode, with $M^2 < 1.3$. This was expected based on the previous single-frequency amplifier described above. The backward power grew significantly beyond 400 W output. As stated previously, the fiber used was a proprietary AFRL design modification based on the standard LMA PCF commercially available from NKT Photonics. At the time, this modification was believed to be the cause of mode quality issues, implying the waveguide design was not optimal. However, results presented in later sections will show this issue may not be solved by optimizing the waveguide structure.

As mentioned above, the previous fiber used suffered from polarization stability issues. Consequently, using a refined manufacturing process, NKT Photonics developed a PCF with superior polarization stability. A commercial off the shelf (COTS) fiber was

then employed in a new set of single-frequency power scaling experiments. The general fiber specifications of the COTS fiber were similar to the fiber used previously.

Figure 31 is an end-face view of the COTS fiber. A summary of single-frequency power scaling results with the COTS fiber follows.[72]

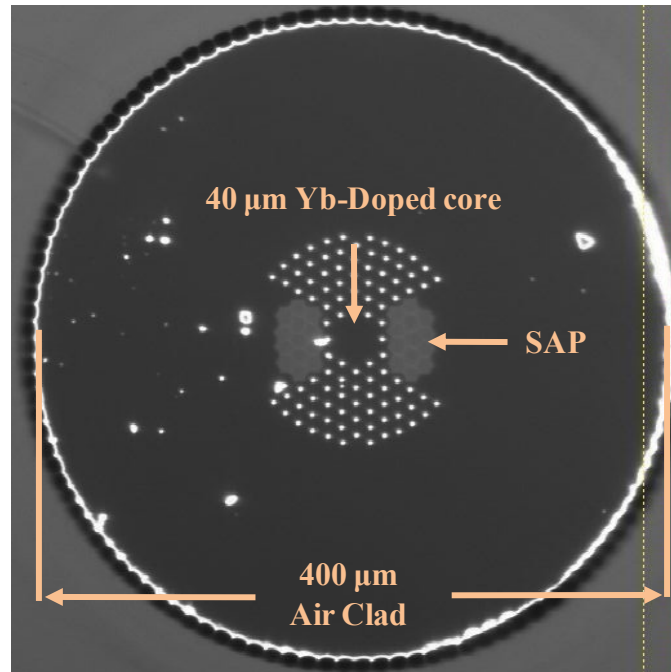


Figure 31: Microscope end-face view of a commercial-of-the-shelf (COTS) large mode area photonic crystal fiber having a 40 μm Yb-doped core, stress applying parts and air hole lattice used to guide the signal mode. The air clad is 400 μm in diameter.

The nominal core diameter and mode field diameter (MFD) of the fiber were 40 and 28 μm, respectively. The inner cladding had a diameter of 400 μm with a numerical aperture of 0.55. The diameter of the air holes in the cladding were approximately 2 μm with a pitch of 10 μm and extended to approximately 55 μm from the center of the fiber. The outer cladding was 617 μm in diameter and was surrounded by a high temperature acrylate that was approximately 52 μm in thickness. The absorption was measured to be

2.4 dB/m at a pump wavelength of 976 nm. The fiber used in the experiment was 6.5 meters in length and was coiled at a diameter of 40 cm. The fiber ends were angle cleaved to greater than 4 degrees to prevent parasitic oscillations. Approximately 15 W of seed light was coupled into the core of the PCF. At a maximum launched pump power of approximately 550 W, the signal was measured at 427 W with an amplified spontaneous emission (ASE) suppression of better than 35 dB. The output signal power with respect to the launched pump power is shown in Figure 32. The slope efficiency was approximately 77%. The slope efficiency calculation assumes 100% of the pump light was coupled to the fiber.

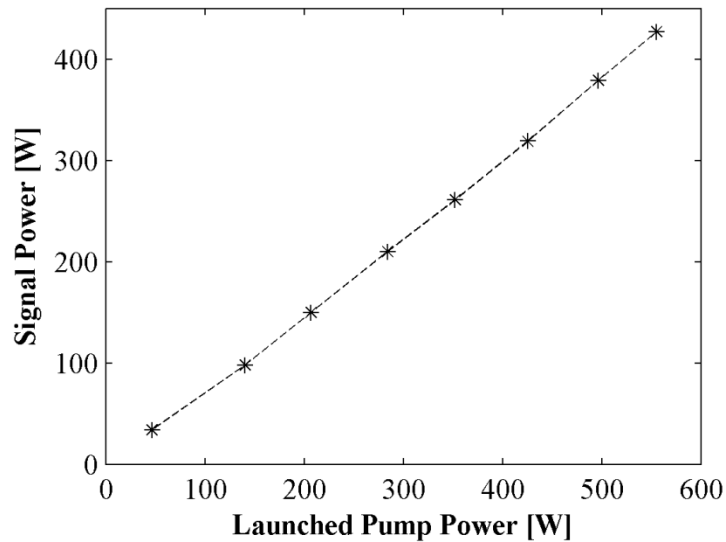


Figure 32: (black) Output power of signal vs. launched pump power showing a slope efficiency of 77%.

Attempts to scale beyond 450 W failed due to catastrophic damage to the fiber. Consistent with operating in this power regime was the onset of temporal pulsations which were monitored with a photodiode. Initially these pulsations were thought to be related to the onset of SBS. However, it was later found that the pulsations were caused

by inadequate preparation of the input and output fiber facets and poor seed coupling. As the pump power and fiber temperature increased, the input end of the fiber shifted slightly due to thermal expansion of aluminum fiber holding chuck. As a result, the seed coupling was modified throughout the power scaling experiment. This issue was mitigated by using a water-cooled chuck. It should also be noted the numerical model showed the SBS threshold for this amplifier to be at much higher power.

Beam quality measurements were made using a Spiricon M^2 beam analyzer. The values of M^2 were measured to be in the range of 1.2 and 1.4 depending on the measuring axis and output power. A plot of the beam profile from one set of measurements is shown in Figure 33.

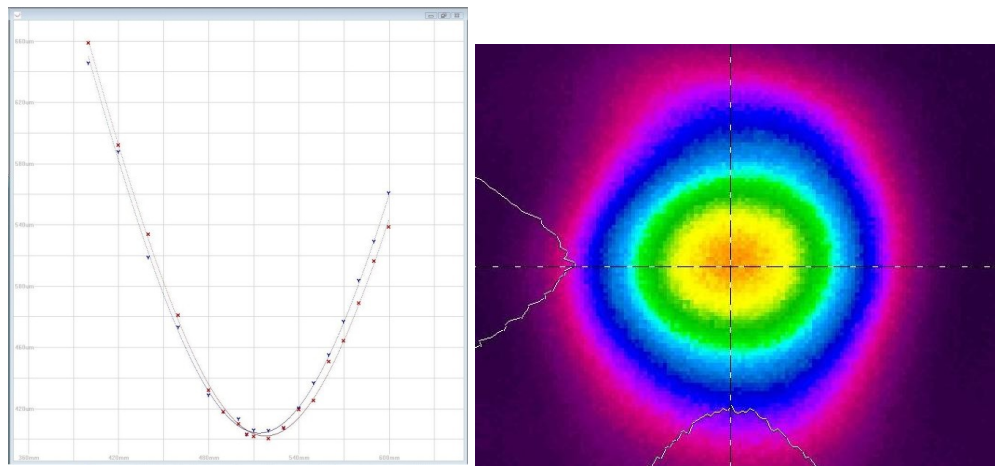


Figure 33: Beam profile and M^2 measurement at 400 W output.

A limited supply of the COTS PCF was purchased for this power scaling demonstration. As such, the investigation was concluded due to lack of gain fiber. However, concurrent with the investigation above, was the design and development of a novel SBS suppressive fiber.

3.5. Segmented Acoustically Tailored Fiber

The photonic crystal fibers used previously were all manufactured to be an analog to standard conventional LMA step index fiber. Typically, the conventional fibers used in high power amplifiers have a 25 μm core and 400 μm cladding. The cladding diameter is fixed in a trade space between the maximum brightness of the available high power pump diode systems and the maximum NA achievable in a step index fiber design. Since the air-clad in a photonic crystal fiber is not limited by these restrictions, it makes sense to decrease the cladding diameter. As previously stated, this will increase pump absorption and decrease required fiber length. The design of two photonic crystal fibers exploited this advantage. One fiber contained an acoustically tailored core, intended to suppress SBS, while the other contained a core similar to that found in the COTS fiber. The fiber dimensions were made exactly the same, having a mode field diameter of 30 μm , pump cladding diameter of 300 μm , and pump absorption of ~ 4 dB/m. The only difference between the two fibers was the acoustic tailoring.

Previously, it was shown the Brillouin angular frequency is given by $\Omega_B = 2n v_A \omega / c$, where ω is the angular frequency of the optical wave, n is the optical index of refraction, and v_A is the acoustic velocity. Both n and v_A can be manipulated through the proper choice of dopants in the core. However, in order to preserve the optical properties of the fiber, only a variation of the acoustic velocity can be utilized to introduce multiple transverse Brillouin frequencies. Therefore, a crucial consideration in the design is the proper choice of dopants and their concentrations.

The segmented acoustically tailored (SAT) fiber core, shown in Figure 34, was designed with a transverse acoustic profile to give two distinct Brillouin peaks. This design differs from the work by Corning, as their design called for a continuous change in acoustic profile in the transverse direction. It has been shown theoretically that marginal improvement is obtained by utilizing the thermal and continuous acoustic gradients in conjunction due to the overlap in the effective Brillouin gain bandwidth induced by these two effects.[89] Furthermore, a perfect match in optical index between the continuously changing compositional sections in the core region is, in practice, difficult to accomplish. As the result, strong light scattering occurring at the layer interface induces very high background loss. [84]

The stack and draw process was exploited to eliminate the development of an optical interface between the two acoustic regions. To accommodate further SBS suppression through the application of externally applied or optically induced thermal gradients, the peaks were designed to have a separation >200 MHz. Since the Brillouin shift is approximately $2 \text{ MHz}/^\circ\text{C}$, [99] this design would allow for the introduction of a temperature variation of $\sim 100^\circ\text{C}$ without any overlap in the Brillouin gain bandwidth.

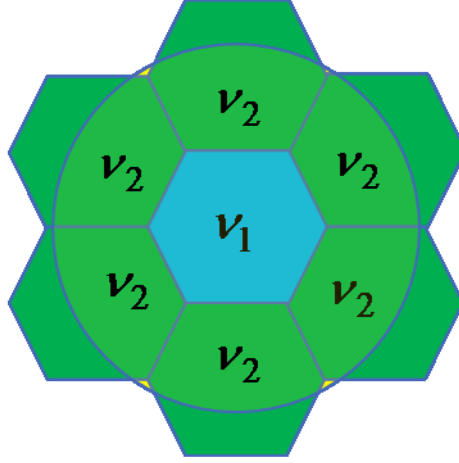


Figure 34: The core design of the segmented acoustic fiber. The Brillouin shift in the center region comprised of one hexagon is different than that in the outer region comprised of six hexagons. The acoustic velocity of each region is denoted by $v_{1,2}$, and the optical mode field diameter is overlaid to scale.

The fiber design was also approached from the point of view that the electrostriction source term is the dominant effect in determining the nonlinear effective area. Consequently, the effective nonlinear area, A_{eff} , is given by [100]:

$$A_{eff} = \frac{\left(\iint |\phi(x, y)|^2 dx dy \right)^2}{\iint |\phi(x, y)|^4} \quad (3.5)$$

where ϕ is the transverse optical profile. To optimize SBS suppression, it was important that A_{eff} for each of the two segments be approximately the same; lest one of the peak Stokes frequencies would run away with the gain and hit the SBS threshold prematurely. The geometric area of the outer ring is six times that of the central segment. However, due to the Gaussian profile of the lowest-order guiding mode, the two nonlinear effective areas are roughly the same.

3.5.1. SAT Doping Configuration

A combination of dopants comprised of fluorine, alumina and germania was used to achieve the acoustic tailoring. To accommodate >200 MHz separation, an acoustic velocity difference of approximately 70 m/s between the two regions is needed. Both fluorine and germania increase the acoustic index of refraction while alumina has the reverse effect. The optical index of refraction increases with germania and alumina content and decreases with that of fluorine. Of these dopants, fluorine has the largest effect on the acoustic velocity leading to an estimated decrease in acoustic velocity of 214 m/s/wt%. When considering variation in the concentration of alumina, the effect of ion clustering was taken into account. At the time the fiber was designed, there were a limited number of resources citing quantitative data for the effect of these dopants on the acoustic and optical refractive index. The values that were found in the literature differed rather significantly. The initial attempt at defining reasonable dopant concentrations was generated with data backed out of a paper published by Corning on acoustic tailoring.[82] The authors used delta profiles, e.g. Figure 35, to show relative changes in refractive index. For the optical field the refractive index of pure silica was chosen as the reference and for the longitudinal acoustic field, the acoustic index of the cladding is chosen to be reference. The definitions of the optical delta profile and acoustic delta profiles are shown below,

$$\Delta_i = \frac{n_i^2 - n_{ic}^2}{2n_i^2} \times 100\% \quad i = o, a \quad (3.6)$$

where ‘ i ’ can either be ‘ o ’ standing for optical field or be ‘ a ’ standing for acoustic field. n_i represents the index of the core, and n_{ic} stands for the index of the cladding. [82] An example fiber used from the Corning paper is shown in Figure 35.

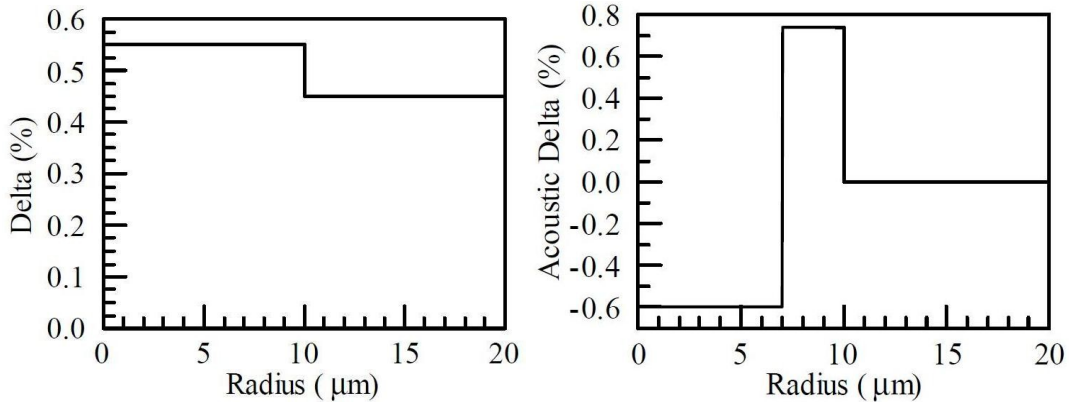


Figure 35: (left) Optical delta profile of a step index fiber with core doped with GeO_2 only. (right) Acoustic delta profile of a fiber with more Al_2O_3 , and subsequently, less GeO_2 doped in the inner region of the core.[82]

Two different fibers are described in figure above, each having a unique doping profile. For brevity, only a two index profiles are shown. The dopant profile in Figure 35 (left) is such that the optical and acoustic index of refraction is uniform. The dopant profile in Figure 35 (right) is such that the optical index profile is uniform, similar to Figure 35 (left), but the acoustic index profile has been modified. Optically, both fibers would operate the same. However, the acoustic profiles are such that the generation of Stokes light would be different due to the modification in radial acoustic velocity profile. Additionally, the paper contained a measurement of the acoustic velocity profile, shown in Figure 36, for the fiber described by Figure 12.

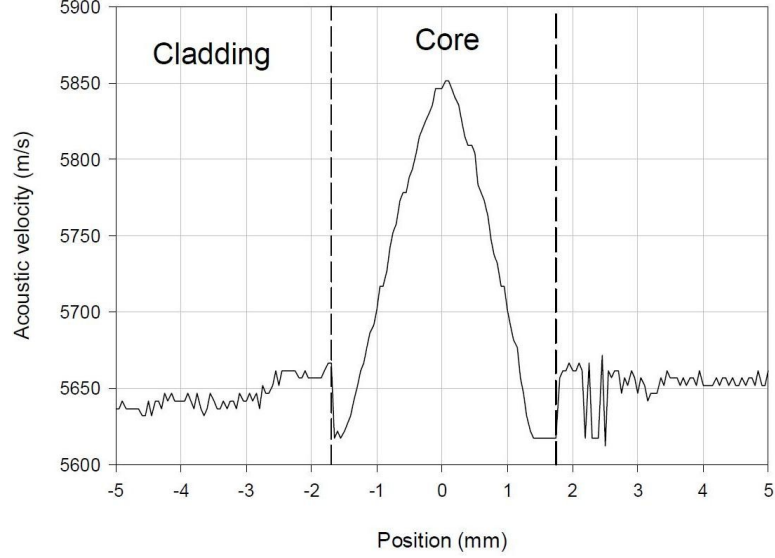


Figure 36: Acoustic velocity profile of fiber preform for Corning fiber design given in Figure 12.[82]

These examples, and a few others given in the paper, provided the following relationships for the optical index and Brillouin shift:

$$n = n_0 + 0.00146[\%mol GeO_2] + 0.00185[\%mol Al_2O_3] - 0.0107[\%mol F] \quad (3.7)$$

$$\nu_B = 16 GHz - 0.1356[\%mol GeO_2] + 0.1342[\%mol Al_2O_3] - 0.428[\%mol F] \quad (3.8)$$

where n_0 is the optical refractive index of fused silica at 1064 nm, and ν_B is the Brillouin frequency shift in Hz at 1064 nm. Note, $\nu_B = \Omega_B/2\pi$, where Ω_B is given by Eq. (1.3). The piece missing from these relationships is the effect of the Yb_2O_3 dopant. This was not significant because the Yb concentration would be kept uniform throughout the core.

The next step was to transition a specific doping recipe to the fiber manufacturer, NKT Photonics. The standard procedure for doping a PCF LMA core is to add the

desired index raising dopants, e.g. Al, Ge, Yb, and then reduce the refractive index with fluorine to that of pure fused silica. A sample dopant recipe is given below.

Table 6: Example doping configuration for Segmented Acoustically Tailored fiber core.

<i>Region</i>	<i>GeO₂[%mol]</i>	<i>Al₂O₃[%mol]</i>	<i>F [%mol]</i>	<i>SBS Shift [GHz]</i>	<i>Δn = n-n₀</i>
Center	0	1.63	0.2822	16.097	0
Outer	1.0	0.843	0.2822	15.857	0

The doping configuration given in Table 6 would produce the qualitative optical and acoustic index profiles shown in Figure 37 below.

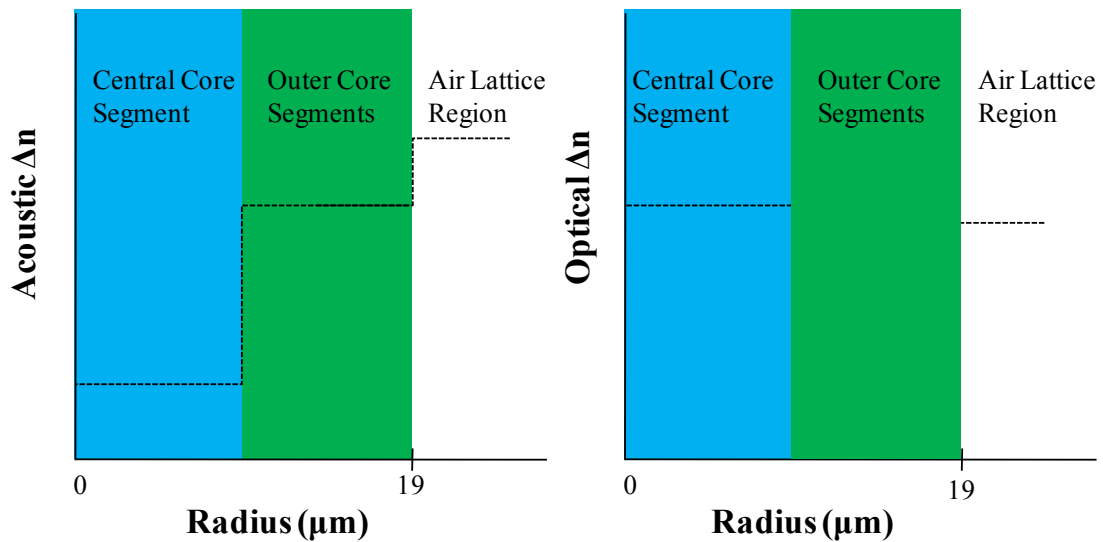


Figure 37: Optical and acoustic refractive index profiles in the Segmented Acoustically Tailored (SAT) fiber design.

NKT Photonics, like all commercial fiber manufacturers, have specific design requirements for the aluminum content of Yb-doped fibers. These considerations are largely related to the mitigation of photodarkening. Subsequently, the actual doping

profile for the SAT fiber design cannot be given, as it contains this proprietary information.

3.6. Brillouin Gain Spectrum Measurement

Regardless of the SAT doping profile, a true measure of the fiber design is found by characterizing the Brillouin gain spectrum (BGS). A number of methods have been implemented for Brillouin gain spectrum characterization of low-loss passive fibers.[101,102,103,104] In most cases, these techniques are performed on very long fibers having relatively small core diameters. In general, a laser having a linewidth considerably less than the Brillouin gain bandwidth is coupled to the fiber core. High resolution spectral measurements are made on the backward traveling light, which is composed of Rayleigh and Brillouin scattered frequencies. Precise measurements are also made on the forward or “SBS pump” power and the resulting back scattered power. This data, along with fiber characteristics such as length and core area can be used to calculate an effective Brillouin gain coefficient $g_{B,eff}$.

The intent in this investigation is to make the measurement in Yb-doped LMA fibers, in the absence of excitation due to 976 nm pump. Additionally, the measurement should be done at the signal wavelength of interest, 1064 nm. Recall, the Brillouin shift (Ω_B), Eq. (1.3), varies inversely with λ_p , the SBS pump wavelength. The Brillouin gain bandwidth, (Γ_B), is expected to obey a λ_p^{-2} dependence. However, the peak Brillouin gain ($g_{B,max}$) is known to be nearly independent of pump wavelength.[100] Therefore,

the choice of laser wavelength in this measurement is not critical for an estimation of the peak Brillouin gain. Conversely, the effective Brillouin gain ($g_{B,eff}$), Eq. (1.2), is modified by the Brillouin gain bandwidth which is wavelength dependent.[100] The efficacy of SBS mitigation techniques which tend to shift the peak Brillouin frequency, e.g. thermal gradient and stress/strain, are impacted greatly by the Brillouin gain bandwidth. Consequently, it is of interest to know the Brillouin gain bandwidth at the intended operational wavelength of the amplifier.

The choice to make BGS measurements on LMA Yb-doped fibers at 1064 nm is complicated by the absorption of the Yb-ions, and the reduction of intensity inherent to the LMA core. Fiber length restrictions are dictated by more practical limitations. Standard low-loss, passive, 6/125 single mode fibers cost ~\$15-20 per meter. In contrast, Yb-doped LMA fibers can range \$400-1000 per meter. Thus, relatively high SBS pump powers are required for accurate BGS measurements, to compensate for fiber length restrictions. For these reasons, measurements are made with a pump-probe technique, first demonstrated in Ref. [102]. Additionally, the pump-probe technique allows for BGS characterization in a low SBS gain regime where narrowing, due to the SBS process, has negligible impact on the Brillouin gain bandwidth. As such, the measurements made allow for an estimation of the spontaneous Brillouin gain bandwidth which can then be used in the numerical model for accurate fiber amplifier modeling.

3.6.1. Pump-Probe Experimental Setup

The BGS pump-probe experimental setup is shown in Figure 38. Two non-planar ring oscillators (NPRO) sources, operating at 1064 nm, were used as the pump and probe (Stokes) laser sources. These two signals are coupled to the test fiber, counter-propagating with respect to one another. In this method, the SBS process is seeded by the probe signal. This allows for an artificial SBS threshold to be reached in the fiber at very low power levels. One major drawback to this particular technique is the free space coupling of the pump and probe lasers. Repeatability of coupling efficiency into the test fiber requires considerable attention when quantitative measurements are made.

Each laser is protected from backward traveling light by an optical isolator before being free-space coupled to a polarization maintaining 6/125 delivery fiber. Fused fiber tap coupler/splitters were used to separate 1% of the signal to be later combined with a 50/50 coupler. The output of the 50/50 tap is coupled to a fast photodiode capable of resolving the beat frequency between the pump and probe signals. An RF spectrum analyzer (RFSA) provides high resolution measurement of the beat frequency. Most of the coupled pump and probe light is transmitted to the test fiber for BGS measurement. The probe light is propagated through an optical isolator, and free-space coupled into one end of the test fiber. A half-wave plate is used to align the probe light polarization to the appropriate axis of the PM test fiber. Special care must be taken when choosing the lens pair for mode matching to the test fiber core. A simple Gaussian beam optics model is used for lens pair calculations. The polarization of the probe signal exiting the fiber is rotated such that a polarization beam splitter (PBS) directs all SBS probe light toward the power meter. The pump signal provided by the NPRO is not sufficient to excite the

SBS process, thus it was necessary to build a small monolithic fiber amplifier to increase the SBS pump power. The pump signal was amplified up to 8 W by utilizing a single stage. The output of the amplifier is propagated through an optical isolator and the Faraday Rotator. It should be noted, all optical isolators shown can be generalized as Faraday Rotators. This distinction is made for the experimental setup to show the process by which the backward light is captured.

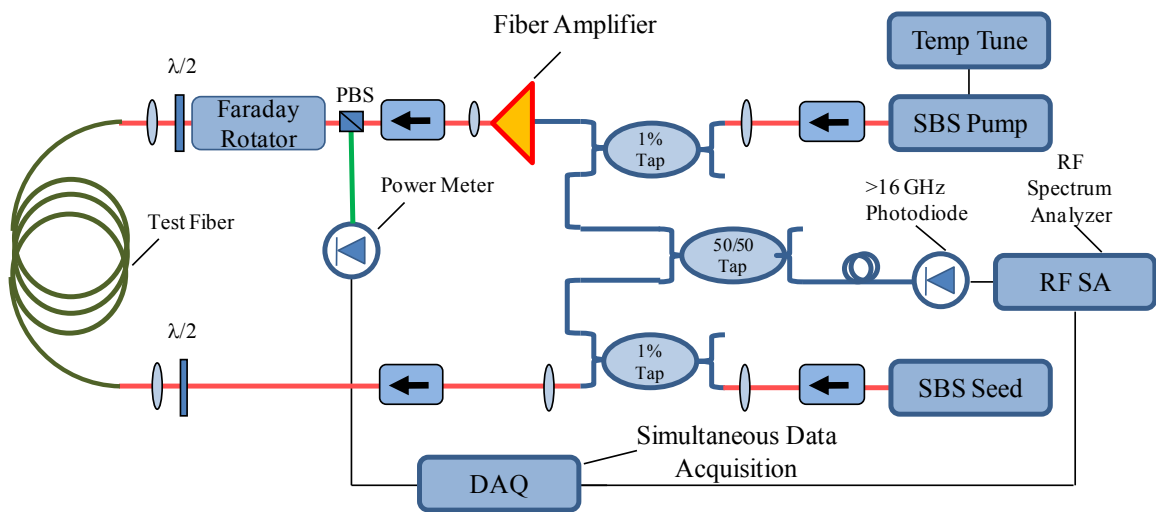


Figure 38: Pump probe experimental setup showing two NPRO lasers labeled “SBS Seed” and “SBS Pump”. The two lasers are sampled by fused fiber couplers for beat frequency measurements. The two signals are free space coupled into the test fiber in a counter propagating configuration. Thermal tuning of the SBS pump laser shifts the frequency through the Brillouin resonance of the test fiber. A power meter is used to measure scattered SBS pump light. The power and beat frequency are measured simultaneously with a computer controlled data acquisition card.

When the frequency difference between the probe and pump lasers is far from the Brillouin gain resonance, the power measured is that of the transmitted probe. The frequency of the SBS pump is tuned by slowly modulating the temperature of the Nd:YAG gain crystal. This is a standard feature on the JDSU NPRO-125 laser used. The pump laser was specifically chosen for temperature tuning because the gain of the

Nd:YAG crystal is temperature dependent. Thus, a modulation of the probe laser temperature would lead to non-uniform output power vs. frequency. This problem is mitigated in the pump signal because a fiber amplifier is used to increase the pump power. The gain fiber in the pump amplifier was saturated by coupling sufficient seed power. In this high seed power/low gain situation, small changes in the seed power produces similarly small changes in the pump amplifier output power. Another temperature related consideration is the occurrence of longitudinal mode hopping in the NPRO. Heating the Nd:YAG crystal causes a physical expansion and increase in refractive index. Both of these effects tend to increase the resonator optical path length (OPL), which decreases the frequency of the laser. As such, particular temperature regimes correspond to two resonant longitudinal modes.[105] This effect is shown in Figure 39.

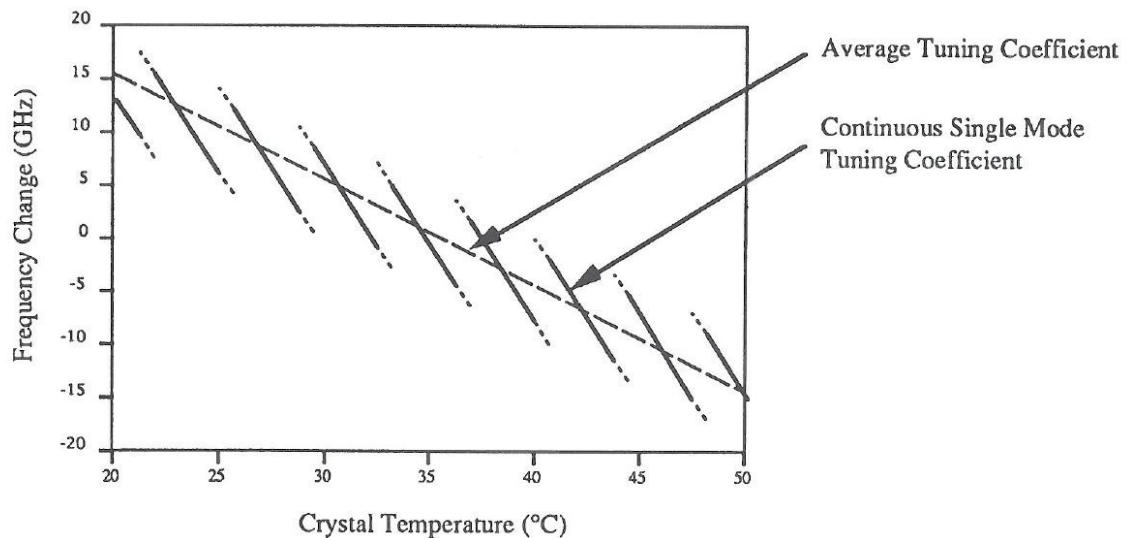


Figure 39: Frequency dependence of thermal tuning typical of a JDSU NPRO laser. The solid lines represent regions of continuous single axial mode tuning. The dashed segments at the end of these lines indicate the laser is near a mode hop. The heavy dashed line represents the average tuning coefficient for the laser as it passes through mode hops.[105]

Fortunately, the NPRO frequency tuning range of $\sim 25\text{-}30$ GHz allows for the pump and probe lasers to be shifted 16 GHz from one another. The continuous single axial mode tuning range of a single laser is $\sim 5\text{-}10$ GHz, while a typical BGS measurement in this work will call for a tuning range of only 1 GHz. A rough estimate for the temperatures is achieved by coupling the output of the 50/50 tap in Figure 38 to a high resolution optical spectrum analyzer. The lasers are tuned such that they are ~ 16 GHz apart, and in the appropriate configuration. The SBS probe must be downshifted by 16 GHz from the SBS pump. The 50/50 tap output is then coupled to the fast photodiode and monitored with the RFSA. The free spectral range of the Nd:YAG crystal resonator is ~ 8 GHz, which is easily characterized with the RFSA. A suitable frequency, locating the crystal temperature in the middle of the continuous single axial mode tuning range, is found for each laser.

Once the appropriate temperatures for the pump and probe are set, the frequency difference is set to a place believed to be off resonance. The pump and probe powers are set, and thermal tuning begins. A data acquisition device, controlled by a simple Labview program, simultaneously records the beat frequency and backward power. That data is plotted in real time for efficient inspection of data quality.

3.6.2. Brillouin Gain Spectrum: Experimental Results

Initial measurements were made with a Yb-doped LMA conventional step index test fiber. The fiber possessed a geometry typically used in power scaling

demonstrations, having a core diameter of 25 μm and a cladding diameter of 400 μm . A characteristic Brillouin gain spectrum result for this type of fiber is shown in Figure 40.

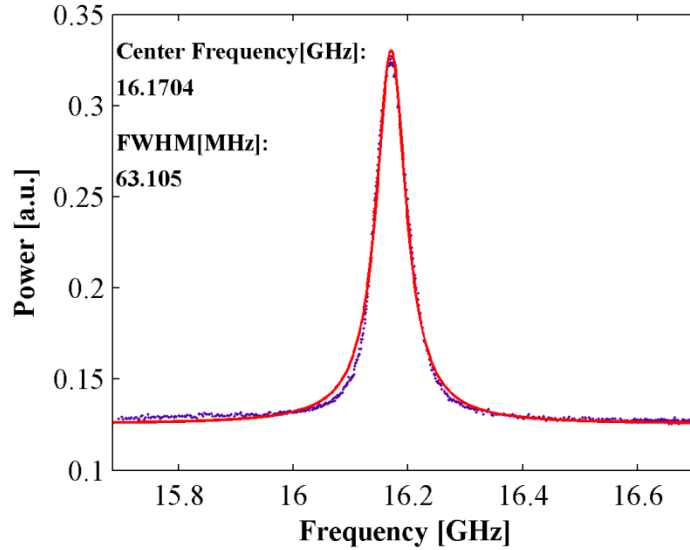


Figure 40: The Brillouin gain spectrum for a conventional step index 25/400 PM fiber. The experimental data, shown in blue, and a Lorentzian curve fit (red) overlays the measured data.

Approximately 4 W of pump light and 100 mW of probe light were coupled into a 7 meter test fiber. The BGS is fit with a Lorentzian function of the form shown in Eq. (1.2). This is the expected behavior for the acoustic resonance since the excited phonon decays as $\exp(-\Gamma_B t)$. The fit gives a center frequency shift, $\nu_B = 16.17$ GHz, and Brillouin gain bandwidth, $\Gamma_B = 63.1$ MHz. Gain narrowing from the SBS process and absorption result in a minor discrepancy between the data and the Lorentzian fit. The off-resonance power on the low shift frequency side (~ 15.8 GHz) of the curve is slightly higher than the high shift frequency (16.6 GHz). This is due to minor variations in output power of the probe laser over the measurement time (~ 30 seconds). There are few published BGS characterizations of LMA Yb-doped fibers. However, the data above is in very good

agreement with those results.[99] As this measurement was consistent with previous work, attention turned to the scarcely studied BGS characterization of LMA photonic crystal fibers.

The first PCF used in BGS measurements was the older fiber, used in the initial power scaling results, described above. For all measurements, the probe input power was approximately 100 mW, and the coupled pump power varied from 1 W to 6 W. The gain bandwidth at different pump powers was estimated by fitting the spectrum to a Lorentzian and determining the FWHM. Narrowing of the Brillouin gain bandwidth is expected with increasing pump power. Absorption in the fiber precluded low pump power measurements. Thus, an estimate for the spontaneous Brillouin gain bandwidth is found by fitting the change in gain bandwidth with respect to pump power, as shown in Figure 41.

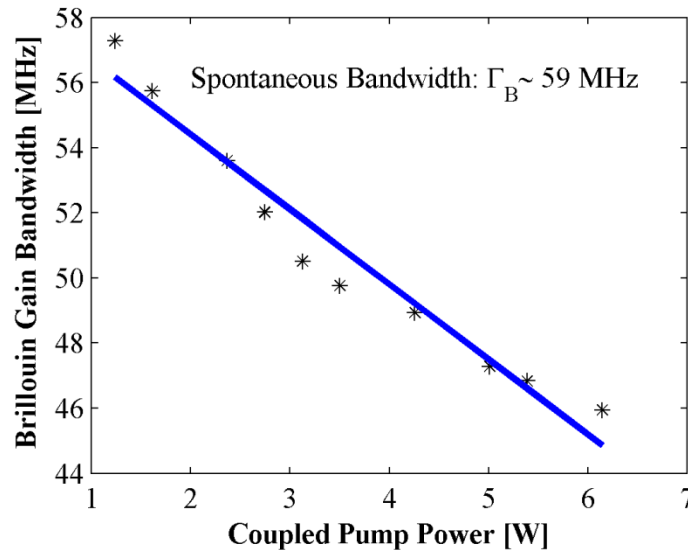


Figure 41: The Brillouin gain bandwidth as a function of pump power. A linear fit (solid blue) is applied to the measured data (black asterisk) give an estimate for the spontaneous Brillouin gain bandwidth at zero pump power of 59 MHz.

A linear fit is applied to the measured Brillouin gain bandwidth data, which estimates a spontaneous bandwidth of 59 MHz at zero pump power. An example BGS measurement of this fiber is shown in Figure 42. This result was achieved at a pump power of approximately 5 W and fiber length of 8 meters. As shown, the Brillouin shift is approximately 15.98 GHz and the gain bandwidth is approximately 46.8 MHz.

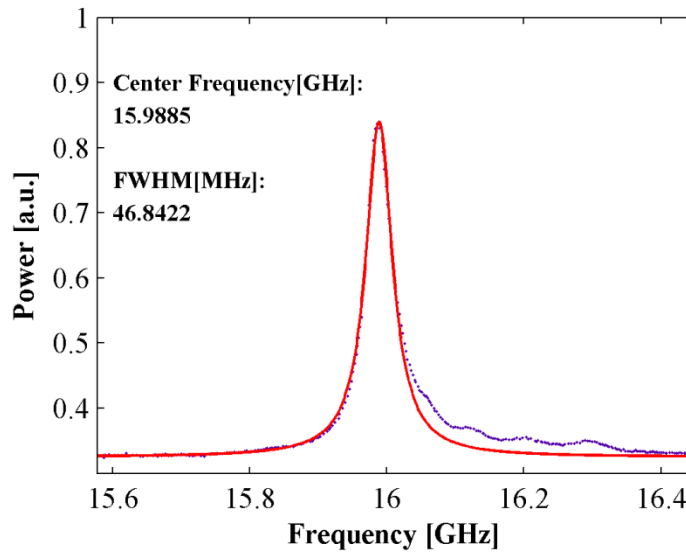


Figure 42: The Brillouin gain spectrum for a LMA photonic crystal fiber. The experimental data, shown in blue, and a Lorentzian curve fit (red) is overlays the measured data.

Immediately one can see the BGS from the PCF consists of features not found in the conventional step index fiber. The secondary (satellite) peaks appearing to the right (high-shift frequency side) of the maximum peak were consistently obtained in all measurements and did not appear to be due to noise or any other systematic error in the experiment.

One possibility is that these secondary peaks are due to the Brillouin scattering interactions of higher order transverse optical modes in the PCF. However, both pump

and probe beams were operating near the diffraction limit. Also, from (1.3) above, the Brillouin shift is given by $v_B = 2n_{eff} v_A/\lambda_L$. Based on the numerical aperture of the core (NA ~ 0.03), the separation between these peaks would be much smaller than what was obtained experimentally. Furthermore, since the higher order optical modes possess a lower effective index of refraction, one would expect these peaks to be on the low shift frequency side of the primary Brillouin gain peak. Another possible reason for these observations could be variations in the polarizations of the pump and probe beams. This seems plausible given issues noted above regarding the polarization characteristics of this fiber. However, upon close examination, these polarizations were found to be oriented along the slow axis and stable throughout the measurements. Additionally, measurements were taken with different fiber lengths and different coil diameters. If unperturbed, the fiber produced consistent BGS results. Dainese et al. have shown that a multi-peaked BGS is obtained in subwavelength-scale PCFs.[106] This phenomenon was attributed to the existence of several families of guided acoustic modes; each with different proportions of longitudinal and shear strain. However, the authors of that work reported that this phenomenon was not observed in PCFs having core diameters above 9 μm . A study by Beugnot et al. using a PCF with a diameter of 5 μm described the co-existence of two strongly coupled acoustic waves as a result of the stress applied through the winding of the fiber.[107] While variations in the stress (or perhaps other structural variations) along the length of the 35 μm core fiber is a possible explanation, another possibility is variations in the acoustic velocity in the transverse direction. It is well known that dispersion-shifted conventional fibers, as well as dispersion-shifted PCFs possessing relatively small core sizes, exhibit secondary BGS peaks. These additional

peaks are generally attributed to the structure of the core.[108] Recall, this PCF was fabricated using the stack and draw technique with the core consisting of 7 hexagonal segments. Although the optical index of refraction is matched to an excellent degree of tolerance among the various segments through the manipulation of the dopant levels, it is conceivable that small transverse variations in the acoustic velocity are present. Previous work, including that shown here, has found common fiber dopants can have drastically different effects on the acoustic and optical properties of fused silica. For example, the addition of 0.1% Mol GeO_2 to pure fused silica would increase the optical index of a fiber core by roughly 0.02%, but reduce the acoustic velocity by 0.19%. To put this in perspective, the fiber used here has an $\text{NA} \sim .03$ corresponding to a core/clad optical index difference of 0.04%. Significant variations in the core refractive index are a well know issue in LMA fibers. In fact, the reason single-mode operation conventional LMA step index fibers are limited to 25 μm diameters is the lack of control in refractive index profile variation. The stack and draw technique allows for some tailoring of the refractive index profile variation. Since each of the seven core segments may be independently scrutinized for the desired refractive index profile before the fiber is drawn. Fiber manufacturers, however, may only concern themselves with optical refractive index. As has been shown above, it is relatively easy to maintain optical uniformity, while modifying the acoustic index of refraction. Working from this hypothesis, one could attempt to fit the BGS shown in Figure 42 with a summation of Lorentzian functions, e.g. one for each segment of the core.

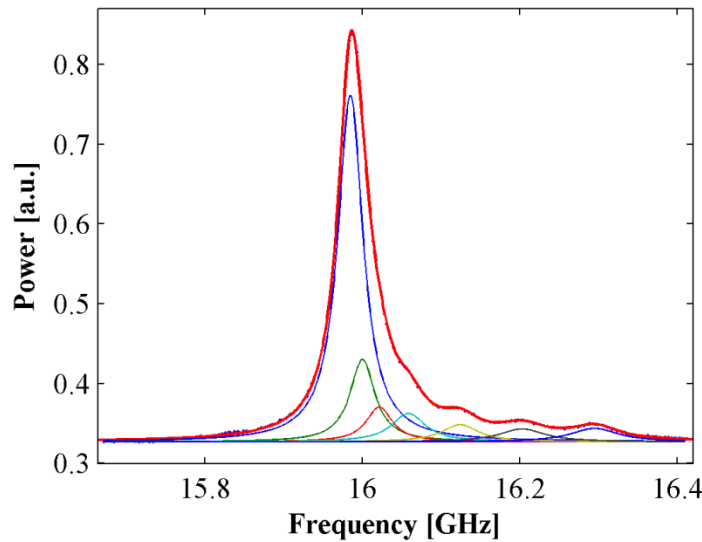


Figure 43: Brillouin gain spectrum fit with 8 Lorentzian functions, based on the assumption that the segmented core is acoustically inhomogeneous. The experimental data is almost perfectly overlaid with the fit. The individual Lorentzian functions used in the fitting function are also plotted.

The composite fit shown in Figure 43 is in excellent agreement with the experimental data. The fit is composed of 8 Lorentzian functions, 7 for the core segments and a 1 for the cladding. It is common to see contributions to the BGS from an interaction between the guided optical mode and the cladding. Clearly, any data could be fit with a sufficient summation of functions. However, the fit does contain some interesting features worth noting. The result above was achieved systematically by increasing the number of Lorentzians used in the fitting function, followed by optimization for best fit. The individual functions show bandwidth narrowing as they come closer to the main peak resonance, shown by the blue curve, which is expected since the SBS gain is increasing. Additionally, it was found that fitting functions which contained less than 8 Lorentzians decreased the accuracy of fit parameters. Increasing the number of Lorentzian tended to degrade the fit quality. However, the parameter

space becomes intractable as the fitting function becomes more complex. It is unreasonable, therefore, to use this as sole justification for the original hypothesis of variations in acoustic velocity. Regardless, the result does supply a sufficiently intriguing commentary to be considered a possibility.

The most commonly accepted explanation for the result in Figure 43 goes back to the existence of multiple acoustic modes in the fiber. However, there have been no experimental or theoretical treatments showing LMA fibers may exhibit acoustic resonances which could explain the satellite peaks. In an attempt to understand this problem more clearly, a sample acoustically tailored fiber was obtained from Corning. The core design of this fiber was used in their 500 W single-frequency amplifier. Acoustically tailored fibers have recently come into the limelight, due largely to Corning's success. Interpretation of the SBS process and acousto-optical interactions in fibers has received similar attention. Depending on the treatment, those who subscribe to the acoustic mode theory would expect the Corning fiber BGS, shown in Figure 44, to have characteristics ranging from many discrete peaks to an individual Lorentzian with significantly reduced gain. The acoustic velocity measurement, shown in Figure 36 qualitatively, describes the acoustic velocity profile of the fiber. Based on the acoustic velocity measurement, it is clear the acoustic index of refraction is lowest in the center of the core and highest in the cladding. Thus, the fiber would be considered an acoustic anti-waveguide. While, the increased SBS threshold for this acoustically tailored fiber is well published, there are no experimental characterizations of the Brillouin gain spectrum aside from that shown here.

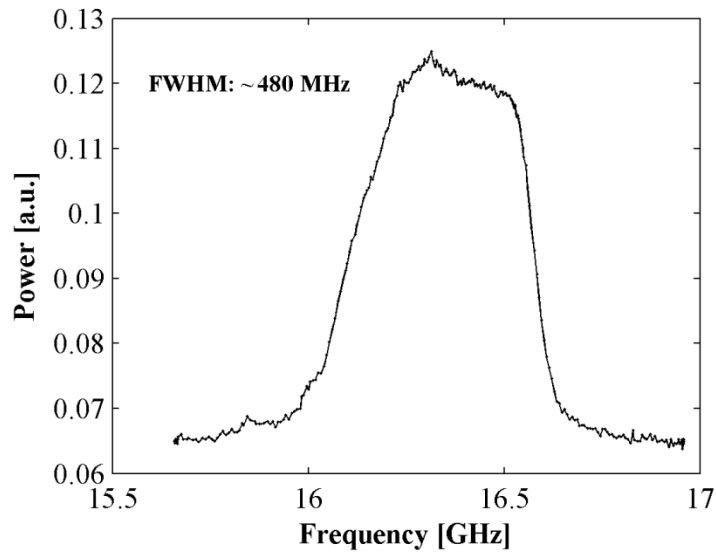


Figure 44: Corning acoustically tailored fiber design used for single-frequency amplifier power scaling. The measured Brillouin gain bandwidth is approximately 480 MHz, which is 10 times larger than the standard Yb-doped LMA fiber.

The fiber used in the result above was polarization maintaining with a 30 μm core, 400 μm cladding, and 7 meter length. Coupled probe and pump laser powers were 100 mW and 8 W, respectively. The interpretation of the SBS process developed in this dissertation dictates this fiber should show a significant broadening of the Brillouin gain bandwidth due to the transverse variation of acoustic velocity in the core. As expected, the fiber shows a Brillouin gain bandwidth approximately 10 times that of a standard LMA fiber. Qualitatively, the Brillouin gain was much lower than previous fibers measured. This estimation is based on the pump power required to achieve a sufficient signal to noise ratio for the measurement. No attempt to quantify the Brillouin gain was made, as it would require a cut-back experiment to estimate the loss due to Yb-ion absorption. A cut-back experiment involves measuring the loss through the fiber at decreasing fiber lengths. The fiber is not a commercial item, thus availability is limited.

Additionally, the peak Brillouin gain was not as important as the qualitative description of the BGS. The measurement lends credibility to the interpretation of the SBS process developed here, but certainly does not discount an acoustic mode interpretation.

3.6.3. Weakly Guided Acoustic Mode Analysis

A simple acousto-optical analysis of weakly guiding acoustic waveguides was performed to investigate the possibility of these satellite peaks being driven by higher order acoustic modes. The acoustic mode solver was taken from a recent theoretical treatment, which was successfully tied to BGS measurements in smaller core fibers.[109] This analysis assumes longitudinal acoustic waves dominate over transverse or shear acoustic waves, thus the displacement vector, $\boldsymbol{\mu}$, must satisfy,

$$\boldsymbol{\mu} = \text{grad}(\varphi) \quad (3.9)$$

In this approximation, the scalar potential, φ , of the displacement vector must satisfy the following:[109]

$$r^2 \frac{\partial^2}{\partial r^2} \varphi + r \frac{\partial}{\partial r} \varphi + r^2 \left(\frac{\Omega^2}{v_i^2} - \beta^2 \right) \varphi = 0 \quad (3.10)$$

where, v_i is the acoustic velocity in the fiber core or cladding, β is the propagation constant of the acoustic mode, and Ω is the Brillouin resonance frequency. In order for guided modes to exist, the acoustic velocity in the core, v_c , must be greater than the

acoustic velocity in the cladding, v_{cl} . This gives rise to solutions for the acoustic mode in the core of the form:

$$u_z = A_0 J_0(U_a r) \quad (3.11)$$

where

$$U_a^2 = \frac{\Omega^2}{v_c^2} - \beta_m^2 \quad (3.12)$$

and J_0 is the Bessel function of the first kind. Solutions in the cladding are of the form:

$$u_z = B_0 K_0(W_a r) \quad (3.13)$$

where

$$W_a^2 = \beta_m^2 - \frac{\Omega^2}{v_{cl}^2} \quad (3.14)$$

and K_0 is the modified Bessel function of the second kind. The optical power is assumed to be in the fundamental mode, thus the assumptions above provide solutions for longitudinal modes, i.e. all solutions are azimuthally symmetric.

The solutions above and their derivatives are continuous at the core/cladding interface, thus the following eigenvalue equation is obtained when these boundary condition are imposed.

$$U_a R \frac{J_1(U_a R)}{J_0(U_a R)} = W_a R \frac{K_1(W_a R)}{K_0(W_a R)} \quad (3.15)$$

The eigenvalue equation above was solved for the PCF used in Figure 42. Estimations were made for the acoustic velocities input to the mode solver. The acoustic velocity of the core is based on the BGS main peak resonance shift of 15.9885 GHz. Similarly, the acoustic velocity of the cladding is calculated from the frequency where the satellite peaks end, ~16.32 GHz. Using Eq. (1.3), the acoustic velocities are $v_c = 5867$ m/s and $v_{cl} = 5989$ m/s. The core diameter and optical mode field diameter are well known at 19 μm and 30 μm , respectively. Since it is of interest to know where in shift frequency these acoustic modes occur, solutions to the eigenvalue equation were found by varying the shift frequency Ω . The propagation constant, $\beta = 4\pi n_{eff}/\lambda_L$, is defined by the requirement of momentum conservation. These input parameters give 21 guided acoustic modes for the PCF. Aside from where the acoustics modes occur in shift frequency, it is also relevant to calculate the acousto-optical interaction with the fundamental optical mode. This interaction is represented by an overlap integral with the optical mode and each acoustic mode, given by:[110]

$$A_{eff}^{a-o} = \frac{\left| \iint |\phi(r)|^2 dA \right|^2 \iint |\psi(r)|^2 dA}{\left| \iint |\phi(r)|^2 \psi(r)^* dA \right|^2} \quad (3.16)$$

The effective area calculation modifies the peak Brillouin gain as shown in Eq. (2.15). The relative strength of each acoustic mode found for the PCF is shown in Figure 45.

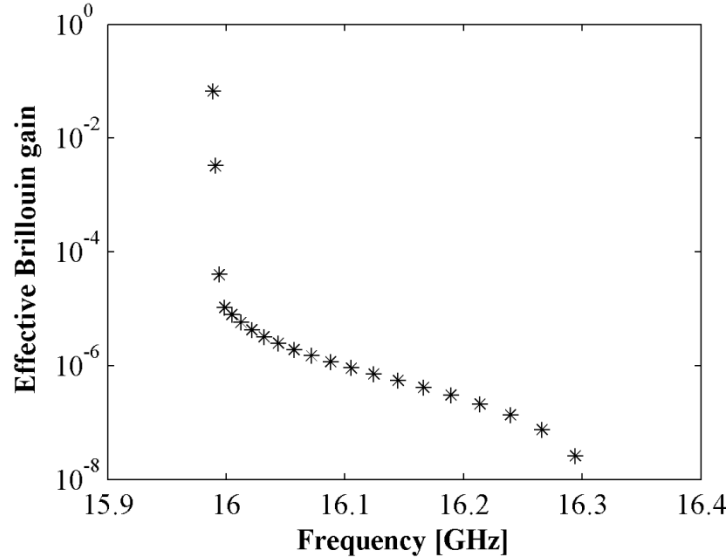


Figure 45: Effective Brillouin gain for each acoustic mode, denoted by asterisk, is show for the shift frequency range of interest. A peak Brillouin gain, $g_B = 5 \times 10^{-11}$ m/W, is divided by the effective area for each mode.

In this analysis, the number of acoustic modes and their relative strength do not seem to account for the existence of the satellite peaks seen in Figure 42. The fundamental acoustic mode is roughly twenty times stronger than the next higher order mode. The effect of this interaction would be undetectable, given the signal to noise ratio of the BGS measurement. The author of Ref. [109] cites the existence of leaky acoustic modes, having a complex propagation constant in the core, giving rise to features qualitatively similar to the satellite peaks. In that paper, however, no leaky modes were found for a fiber with characteristics similar to the PCF shown here.

The theoretical and experimental data presented thus far is inconsistent with an acoustic mode interpretation of the SBS process. Transverse variations in acoustic velocity, due manufacturing non-uniformities, appear to be a more plausible explanation for the unexpected structure in the Brillouin gain spectrum of the PCF. The results,

shown below, for the SAT fiber and reference fiber are also consistent with the preceding discussion. However, of immediate interest is the SBS suppressive nature of the SAT fiber. Regardless of which SBS interpretation is used, all agree, the BGS peak will dictate the SBS threshold of a fiber amplifier.

The reference PCF, designed as a benchmark for the SAT fiber, was characterized with the pump probe Brillouin gain spectrum setup first. The probe input power was approximately 100 mW, and the coupled pump power varied from 4 W to 6.5 W. Figure 46 shows the estimated gain bandwidth at different pump powers found by fitting each spectrum to a Lorentzian and determining the FWHM. The linear fit estimates the spontaneous Brillouin gain bandwidth is 58 MHz at zero pump power.

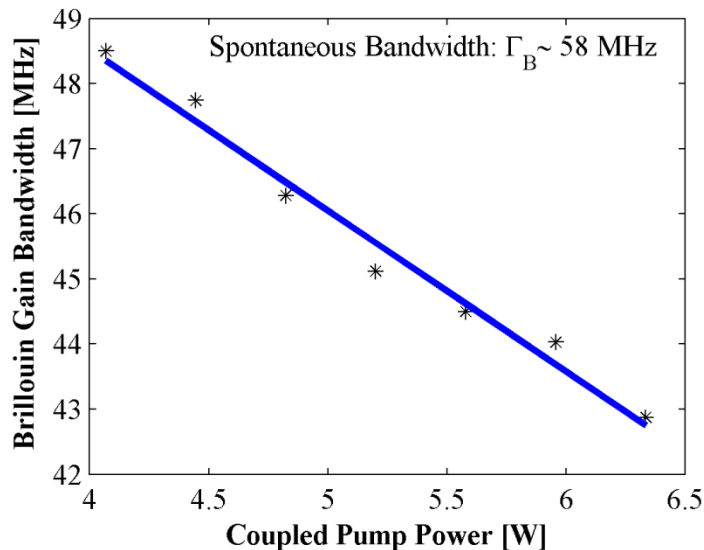


Figure 46: The Brillouin gain bandwidth as a function of pump power. A linear fit (solid blue) is applied to the measured data (black asterisk) give an estimate for the spontaneous Brillouin gain bandwidth at zero pump power of 58 MHz.

The BGS shown in Figure 47 was achieved with a probe power of 100 mW and pump power of 4.5 W. The satellite peaks seen in earlier PCF measurements are not seen

in the new reference fiber. However, there is still increased SBS gain on the high shift frequency side of the main Brillouin peak.

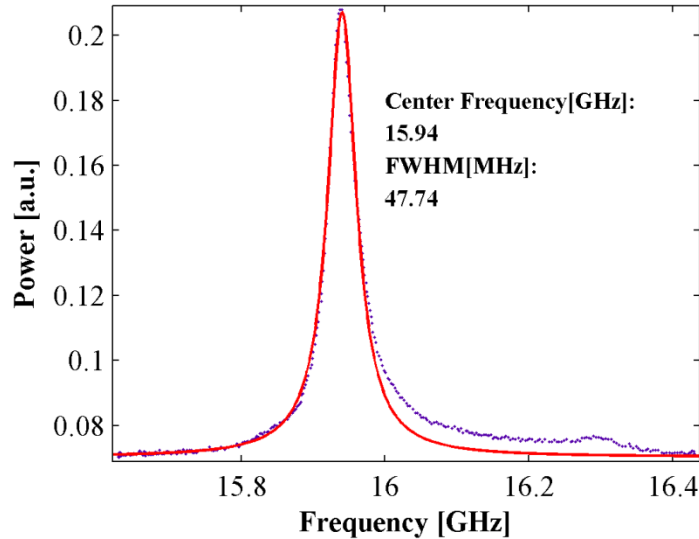


Figure 47: Measured Brillouin gain spectrum of the reference photonic crystal fiber. The main peak is fit with a Lorentzian function giving a center shift frequency of 15.94 GHz and gain bandwidth of 47.74 MHz. The high shift frequency side shows an increased Brillouin gain, similar to previous photonic crystal fiber measurements.

The center frequency and Brillouin gain bandwidth of the reference fiber are similar to the previous PCF. The increased Brillouin gain on the high shift frequency side, without the existence of distinct peaks, suggests a slightly different transverse variation in acoustic velocity. The core dimensions and optical mode field diameter are identical for the two fibers. The primary difference may be slight differences in how the fibers were constructed.

The pump probe experiment was used to obtain a rough estimate of the Brillouin gain coefficient g_B , of the reference fiber. In order to achieve reliable results coupling efficiency for both pump and probe was estimated to be 80% and monitored throughout

this study. Absorption, due to the presence of Yb-ions, of the SBS pump and SBS probe was estimated by performing a cutback experiment. The amount of signal light through the fiber was measured at decreasing lengths. This absorption followed an exponential dependence with length and was nearly constant ($\sim 0.04/\text{m}$) across the range of pump power levels used in the experiment. A fiber length of 10 m was used, and the SBS probe power as a function of input SBS pump power at the peak Brillouin gain was recorded. The results are shown in Figure 48. A theoretical fit based on solving the standard two point boundary problem of a 2×2 coupled system of nonlinear differential equations describing the seeded SBS process was then conducted:

$$\frac{dP_1}{dz} = -\frac{g_B}{A_{eff}} P_1 P_2 - \alpha P_1 \quad (3.17)$$

$$\frac{dP_2}{dz} = -\frac{g_B}{A_{eff}} P_2 P_1 - \alpha P_2 \quad (3.18)$$

were P_1 and P_2 are the SBS pump and SBS seed powers, g_B is the peak Brillouin gain coefficient, A_{eff} is the nonlinear effective area, and α is the absorption due to Yb-ion doping. The Brillouin gain coefficient was varied in the simulations until a best fit was obtained with the experimental results yielding a rough estimate for g_B of 2.3×10^{-11} m/W.

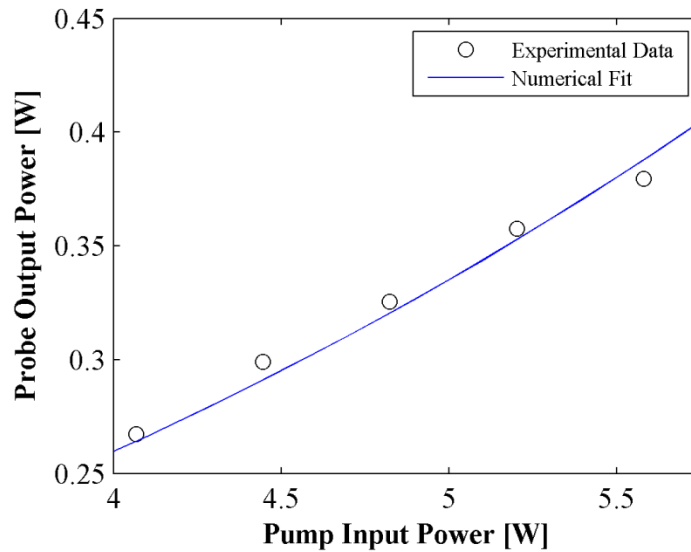


Figure 48: Numerical fit (solid line) obtained by solving the 2x2 coupled system of nonlinear equations overlays the experimental data (circles) for a range of pump powers.

The numerical fit gives a reasonable estimate for the effective Brillouin gain compared to previously measured LMA Yb-doped fibers.[99] This number may then be used to estimate the Brillouin gain coefficient for the SAT fiber.

The experimental conditions for BGS characterization of the SAT fiber were made to be exactly the same as the reference fiber for a direct comparison. The probe input power was approximately 100 mW, and the coupled pump power varied from 4 W to 6.5 W. The BGS shown in Figure 49 was achieved with a probe power of 100 mW and pump power of 4.5 W.

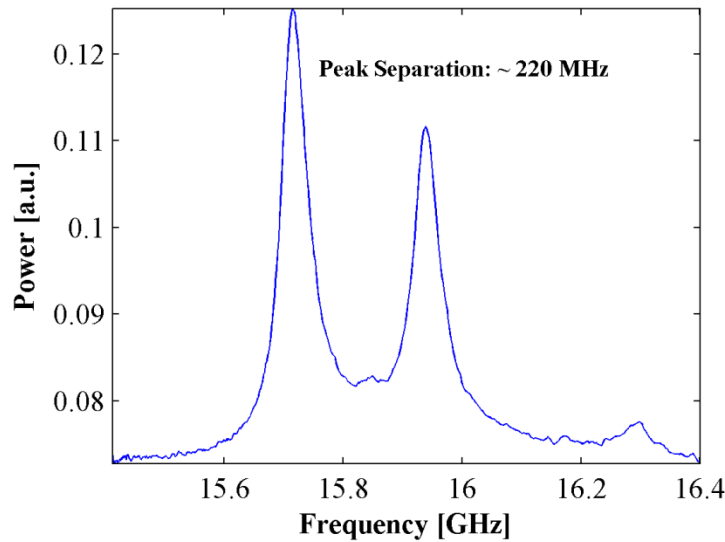


Figure 49: Brillouin gain spectrum for SAT fiber. Two Brillouin peak are shown with center shift frequency of 15.715 and 15.938 GHz, respectively. Each peak has a Brillouin gain bandwidth of ~50 MHz. The high shift frequency side shows an increased Brillouin gain, similar to previous PCF measurements.

The SAT fiber does indeed show two distinct Brillouin gain spectrum peaks, which are associated with the intended transverse variation in acoustic velocity. The dopant specification for the fiber core estimated 250 MHz separation between the two peaks. This was successfully achieved, showing a peak separation of 220 MHz. Each peak has a Brillouin gain bandwidth of ~50 MHz. The largest peak is associated with Stokes light generated in the outer ring of the fiber core which has a smaller acoustic velocity than the central segment of the core. Ideally, one would prefer the two peaks to be of equal height. This discrepancy is explained through the nonlinear effective area, defined by Eq. (3.5). The optical mode field diameter is slightly larger than expected, giving rise to an increased overlap between the optical mode and outer ring core segments. As such, the effective Brillouin gain associated with the outer ring will dictate the SBS threshold of a fiber amplifier. This prediction is predicated on the assumption

that a longitudinal thermal gradient does not provide sufficient shift for cross-talk between the two peaks. As will be shown in section 3.7, thermally induced cross-talk between two peaks can improve SBS suppression. A comparison between the SAT and reference PCF will allow for an estimation of the effective Brillouin gain coefficient for the largest peak. Figure 50 is a direct comparison of the BGS for the SAT and reference fiber.

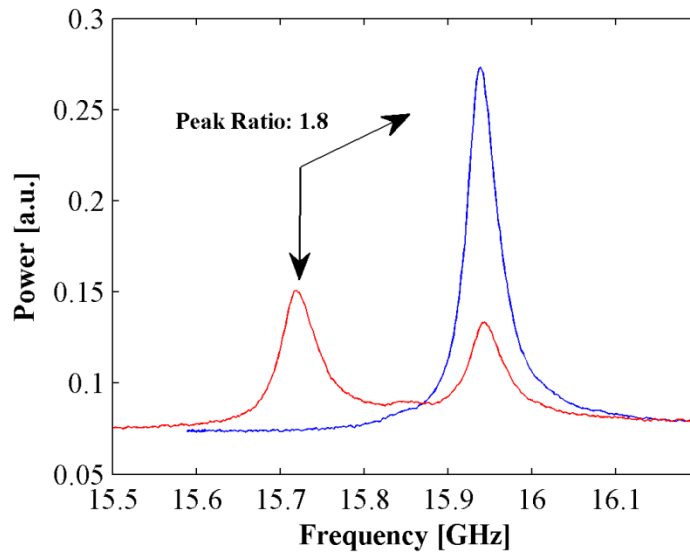


Figure 50: SAT(red) and reference PCF(blue) BGS comparison. The ratio of peaks in the reference and SAT fiber is approximately 1.8.

The BGS comparison shown above was taken with identical experimental conditions for both measurements. Pump and probe powers of 6 W and 100 mW, respectively, were used. The fiber length was 10.16 meters. The Brillouin gain coefficient for the reference PCF was estimated to be $\sim 2.3 \times 10^{-11}$ m/W. Using the peak ratio of 1.8, the largest peak Brillouin gain coefficient is estimated to be $\sim 1.2 \times 10^{-11}$ m/W.

In order to demonstrate further suppression using the thermal gradient, approximately one half of the fiber length was placed in an oven with a temperature of

80 °C as shown in Figure 51. Also, shown in the figure is an idealized depiction of the resultant temperature.

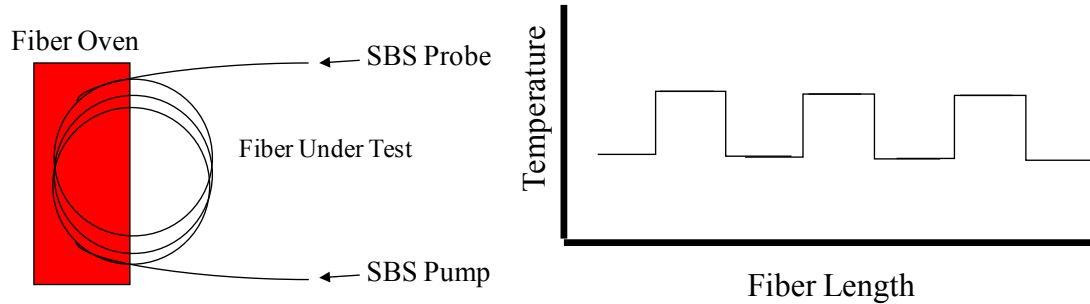


Figure 51: (left) Experimental setup to study SBS mitigation of acoustically tailored fiber in conjunction with the thermal gradient. (right) The idealized temperature profile in the fiber for the experimental arrangement.

As mentioned above, the Brillouin shift due to temperature variation is approximately 2 MHz/ °C. Since the separation in the acoustically tailored fiber between the two primary peaks is approximately 220 MHz, the temperature difference among the hot and cold regions in the fiber is sufficient to prevent any overlap in the SBS gain bandwidth. As a result, four primary peaks were obtained as shown in Figure 52. The variation in the peak heights is attributed to the less than ideal heating conditions in the fiber oven.

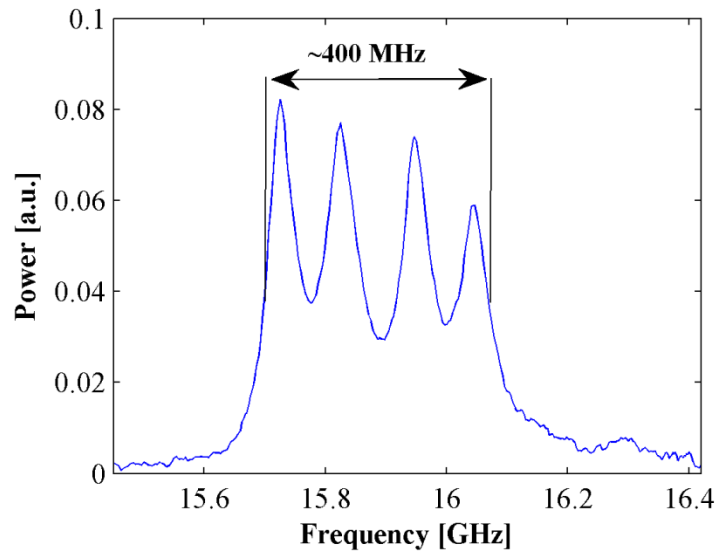


Figure 52: BGS for acoustically segmented fiber with step temperature profile applied leading to four primary peaks. The differences in relative gain among the peaks are attributed to non-ideal heating conditions in the fiber oven.

The shift in Brillouin gain frequency with respect to temperature was measured to be 1.7 MHz/ °C. This number is reasonable, however, the fiber oven used for fiber heating produced less than ideal conditions. The FWHM of the BGS shown in Figure 52 is ~400 MHz, which is to be expected given the 220 MHz peak separation. The thermal gradient in a fiber amplifier, generated through quantum defect heating, would be continuous. Thus a more uniformly broadened BGS would be expected. The measurement above shows this acoustically tailored fiber, used in conjunction with a thermal gradient, may approach the SBS suppression realized in the Corning fiber.

3.7. SAT and Reference PCF Single-Frequency Fiber Amplifier

The reference PCF was utilized in the initial fiber amplifier experiments to create a baseline by which the SAT fiber may be compared. The fiber has a nominal core diameter and mode field diameter (MFD) of 39.5 and 30 μm , respectively, and numerical aperture of 0.03. Stress inducing rods composed of borosilicate and running along the fiber axis ensured that the fiber was polarization maintaining. The inner cladding had a diameter of 329 μm with a numerical aperture of 0.6. The diameter of the air holes in the cladding were approximately 2 μm with a pitch of 10 μm and extended to approximately 55 μm from the center of the fiber. The outer cladding was 580 μm in diameter and was surrounded by a high temperature acrylate that was approximately 61 μm in thickness. The small signal absorption was measured to be 4.2 dB/m for a pump wavelength of 976 nm.

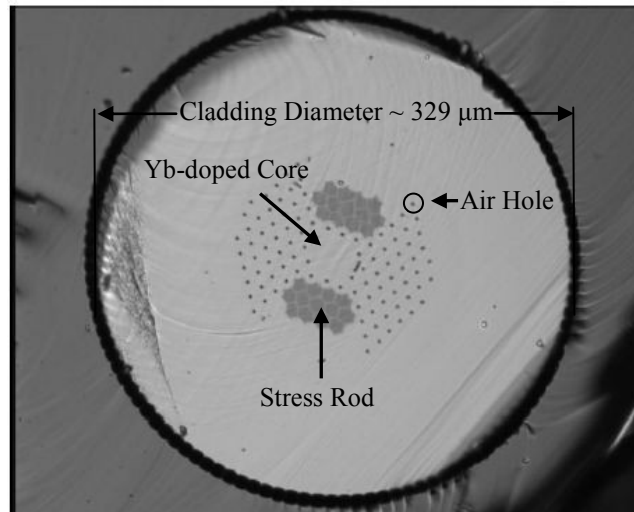


Figure 53: Microscope end view of the reference PCF. The two dark regions next to the core are stress applying parts for PM operation. The thin dark circle defines the pump clad region.

The numerical model shows this amplifier should be capable of significant output powers, before reaching the SBS threshold, with a fiber length of 5 meters and input pump wavelength near 976 nm. The reduced pump cladding diameter not only increases pump absorption, allowing for reduced fiber length, but also increases quantum defect heating for the generation of a substantial thermal gradient. Initially, however, the SBS threshold relative to the SAT fiber should be demonstrated. To that end, an amplifier was constructed with the intent of reaching the SBS threshold in an output power regime of 100-300 W. The motivation to make an amplifier with reduced SBS threshold will become clear in later sections, as issues not related to SBS limit power scaling.

A counter-propagating scheme was used as shown in Figure 21. The master oscillator was a non-planar-ring oscillator (NPRO) from JDSU and provided a maximum single frequency output power of 700 mW. However, only 20 mW were required to saturate the gain fiber in the first stage of the monolithic three-stage fiber amplifier shown in Figure 18. This fiber amplifier served as the seed source for the PCF amplifier. The photonic crystal fiber used in the experiment was ~10 meters in length and was coiled at a diameter of 53 cm. An aluminum ring affixed with water cooled plates was used to hold the fiber, as shown in Figure 54. A chiller, operating at 14°C, supplied water to the cold plates in an attempt to further suppress a thermal gradient. Approximately 2.5 meters of fiber, near the seed input end, was taken off the ring and suspended in air. Each end of the fiber was held in a water cooled chuck, which was mounted on a 5-axis translation stage. The location of each stage was fixed on the optical table. The section of fiber left in the air was required to allow the fiber to conform to the input and output chuck positions.

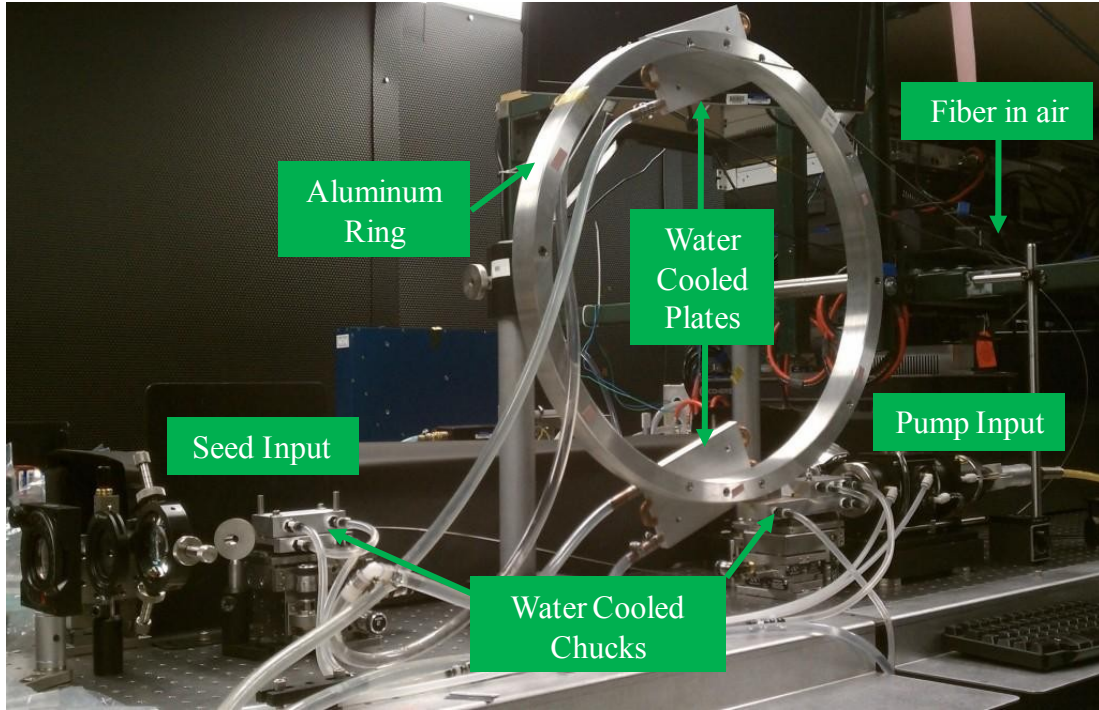


Figure 54: Configuration of photonic crystal fiber in experimental setup. Seed laser is input from the left, where the fiber is held in a water-cooled chuck. Approximately 2-2.5 meters of fiber is left in air before it is spooled on the aluminum holding ring. Cold plates are affixed to the aluminum ring on the top and bottom to improved conductive cooling of the fiber. The end of the fiber comes off the aluminum ring and held in the pump input side water cooled chuck.

Dichroic mirrors on both ends of the fibers were used to separate the pump and signal beams. The fiber ends were thermally collapsed, and angle cleaved to greater than 4 degrees to prevent parasitic oscillations. Approximately 30 W of seed light was coupling into core. The Laserline diode laser was used to pump the reference photonic crystal fiber. The laser was temperature tuned to operate at approximately 972 nm. The gain for the pump diodes changes slightly with temperature, thus a characterization, shown in Figure 55, of the new operating regime was conducted.

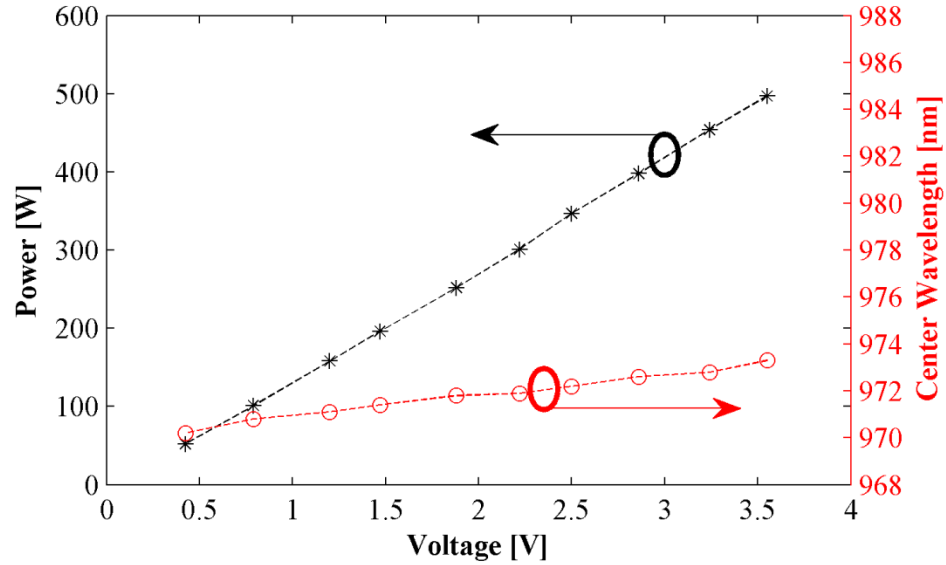


Figure 55: (black) Output power vs. voltage for Laserline Diode pump. (red) Center wavelength of pump diode laser output, which has been thermally detuned from operation at 976 nm.

The absorption of the reference fiber is such that the pump is operated off the Yb-absorption peak to reduce quantum defect heating, and accommodate inversion throughout the 10 meter length of fiber.

The SBS threshold was characterized with the standard technique of indentifying the departure of linear growth in backward power with increasing signal power. The numerical model was used to simulate the amplifier signal and backward power output. The experimental data and numerical results for the signal output power are shown in Figure 56 below.

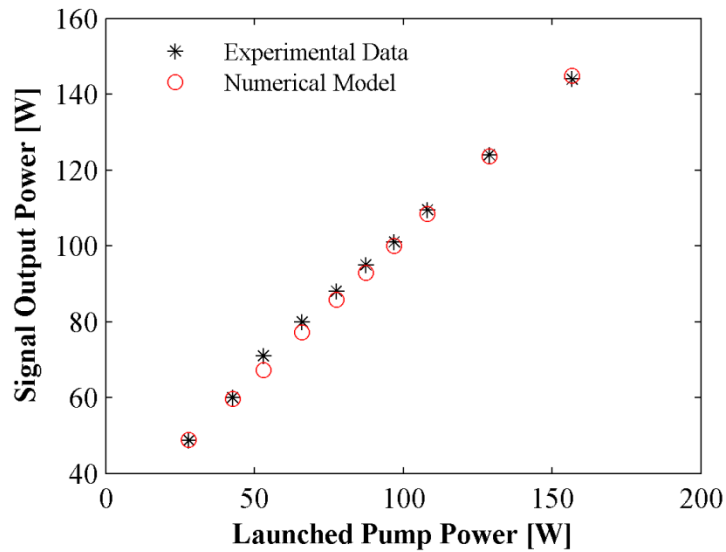


Figure 56: (black asterisk) Experimental data for signal output power vs. launched pump power from the 10 meter reference photonic crystal fiber amplifier. (red circle) The numerical model's prediction for output power of the amplifier.

A maximum output power of 154 W was achieved before the onset of SBS. The polarization extinction ratio was measured to be better than 17 dB for all output power levels. The numerical model is in very good agreement with the experimental data. The variation in center pump wavelength with increasing power, as shown in Figure 55, was input to the model with an absorption coefficient of 3.3 dB/m. The absorption coefficient differs from the quoted 4.2 dB/m, which is measured for small signal 976 nm pump light. This value was obtained experimentally by estimating coupled pump power and measuring unabsorbed pump.

Rayleigh light is not included in the numerical model, thus a direct comparison of the backward powers is not possible. In principal, the contribution of Rayleigh light in a backward power measurement should become negligible as the as the amplifier output nears the SBS threshold. This is demonstrated by the OSA spectrums shown in Figure

58. Thus, a reflectivity may be calculated for the amplifier, and be compared to the numerical model. Unfortunately, this idealized measurement did not translate to the experimental setup. Backscattered light, unrelated to Brillouin or Rayleigh scattering from the fiber, increased the total backward power measured beyond the required fidelity for accurate SBS threshold characterization. Consider a 100 W fiber amplifier operating near SBS threshold. The total backscattered Stokes light should be approximately 0.01% of the signal output power. This corresponds to ~ 10 mW of Stokes light. A number of techniques were implemented to remove unwanted light in the backward power measurement. The conclusion of these attempts identified a significant amount of light being scattered off the output facet of the fiber, and guided in the air-hole lattice surrounding the fiber core. This weakly guided light is also the source of pulsations in the COTS fiber amplifier described above. The effect can be reduced by creating a steeper angle on the fiber facet. This is achieved by angle cleaving, or polishing. An increase in cleave angle tends to reduce the quality of the fiber facet, due to non-uniformity of the facet surface. Fiber polishing allows for the creation of very flat fiber facets, but is subject to unwanted particle deposition in the facet surface. The cleanliness, or lack thereof, due to fiber polishing is difficult to characterize upon microscope inspection. However, when the amplifier is put into operation, absorption of light at the facet leads to catastrophic damage. The best solution would be an endcap, which is cleaved to create a pristine surface. Unfortunately, this is required of the output end of the fiber to mitigate the problem. In order to accommodate the high NA pump light, this endcap must be much larger in diameter than the photonic crystal fiber, or a smaller diameter and much shorter length. In practice, it is difficult to fusion splice fibers of

different diameters because each requires much different amounts of heat to reach a softening temperature. Successful end capping of this PCF was achieved with a 1.3 mm diameter glass rod, as shown in Figure 16. As previously stated, the endcapping process is optimized such that thermal collapse of the air-holes in the PCF is negligible. Attempts at splicing larger endcap diameters proved unsuccessful in this regard. The increased heat required to soften larger endcap diameters led to unsuitable thermal collapse of the PCF waveguide structure. The length of a 1.3mm endcap required for efficient coupling of the 0.6 NA pump light is $\sim 800 \mu\text{m}$. This stringent tolerance on endcap length makes the endcap solution difficult to reproduce experimentally.

The cleanest experimental data for backward power measurements was taken by imaging the PCF core into a $6 \mu\text{m}$, single-mode fiber, which is used as a spatial filter. In this way most of the unwanted backscattered light is removed. As a result, information regarding the reflectivity of the amplifier is lost, and a qualitative measurement of the backward power remains. The numerical model, backward power measurements, and OSA spectrums are all used to validate the reference PCF SBS threshold. Figure 57 shows the backward power measured, and the numerical model prediction.

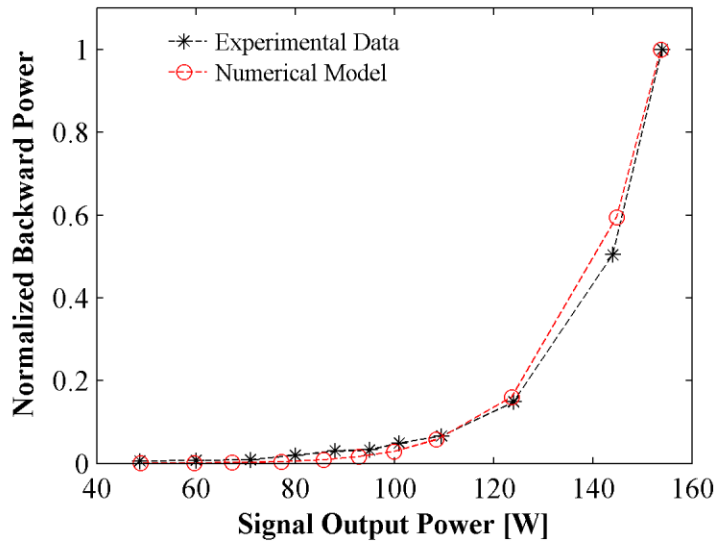


Figure 57: (black asterisk) Experimental data for backward power as a function of output signal power, showing a departure from linear growth. (red circle) The numerical models prediction for backward power.

The figure above clearly shows the backward power departs from linear growth above 120 W output power. This behavior is mirrored by the data from the numerical model. The model and experimental data are normalized to their respective maximum values for a qualitative comparison. Backward power measurements at the highest output power of 154 W were extremely unstable due to the onset of SBS. At the highest output power, the model showed a reflectivity of $\sim 0.05\%$, indicating the amplifier is operating at or near the SBS threshold. The backward power was sampled with a Faraday rotator and a polarization beam splitting cube, similar to the technique used for the pump-probe BGS measurement. The sampled light was imaged into the core of a single mode delivery fiber, which was then split by a 50/50 fused fiber coupler. A high resolution optical spectrum analyzer was used to capture the relative ratio between the Stokes and Rayleigh scattered light simultaneously with the backward power measurements shown above.

The OSA resolution was found to be ~ 1 GHz, which allows for sufficient distinction of the 16 GHz separation between the Stokes and Rayleigh frequency components. Three power levels are shown in Figure 58, which show a substantial growth in Stokes light relative to the linearly increasing Rayleigh scattered light.

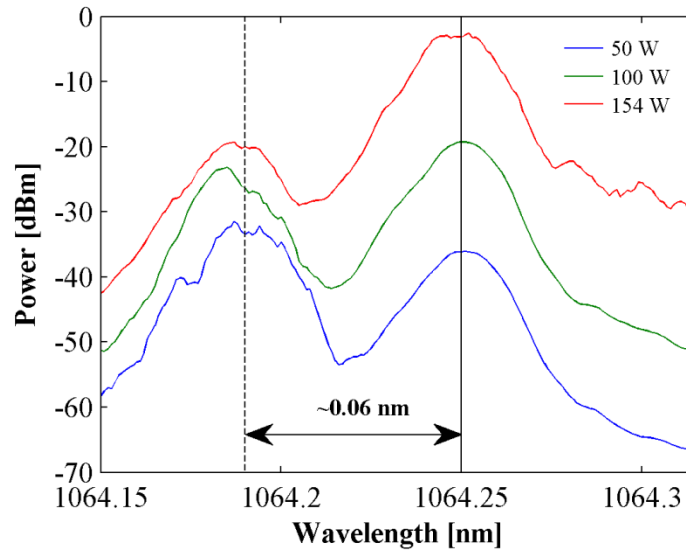


Figure 58: Optical spectrum analyzer data for reference PCF amplifier are three power levels. The peak associated with Rayleigh scattered light is indicated by the vertical dotted black line. The Stokes scattered light is indicated with the vertical solid black line. The peak separation is ~ 0.06 nm, corresponds to ~ 16 GHz at 1064 nm.

The OSA data is consistent with the backward power measurements shown in Figure 56 in that the Stokes scattered light begins to dominate the backward power at 100 W output power. The data also shows a distinct difference in the growth of Stokes power, which is characteristically exponential, relative to the Rayleigh light, which grows linearly.

The high resolution optical spectrum analyzer was also used to characterize amplified spontaneous emission in the amplifier output, and ensure all signal power measured was due to 1064 nm radiation, shown in Figure 59.

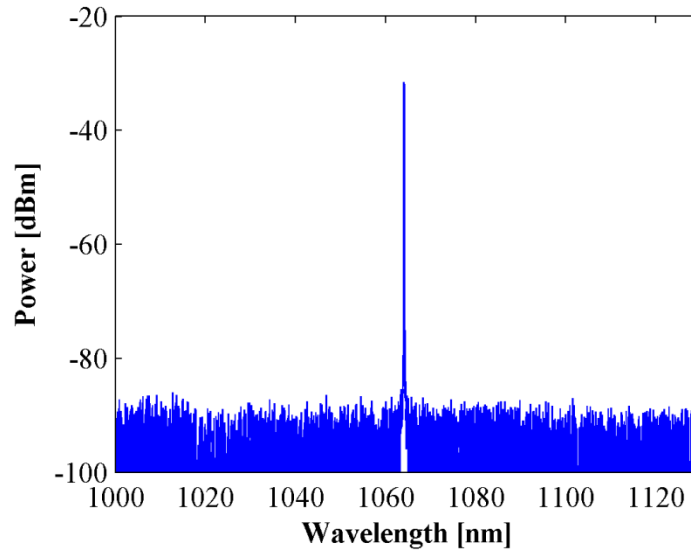


Figure 59: Optical spectrum analyzer data for reference PCF amplifier at 150 W output power. The single peak, at 1064 nm is over 40 dBm above the noise floor, indicating negligible amplified spontaneous emission.

The data shown in Figure 59 was obtained by imaging scattered light from the power meter, measuring the amplifier output, into a 50 μm core, multimode optical fiber. The large core diameter was required to obtain sufficient signal to noise ratio. The fiber was input to the optical spectrum analyzer for analysis. Clearly, the ASE is not a significant component of the output power. This is not particularly surprising, given the amplifier is operating at very low gain.

Beam quality measurements were made using a Spiricon M^2 beam analyzer. The values of M^2 were measured to be in the range of 1.1 to 1.2 depending on the measuring axis and output power. A plot of the beam profile from the highest output power is shown in Figure 60.

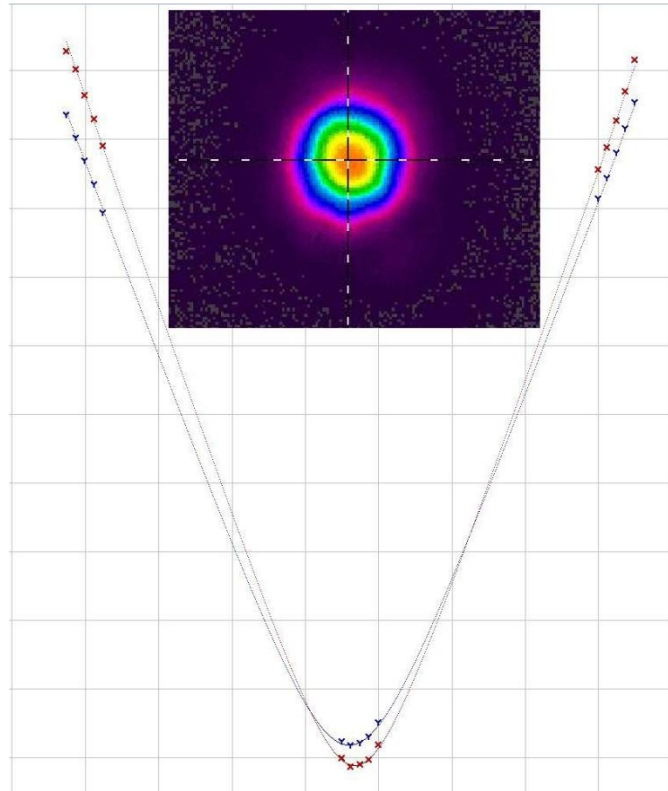


Figure 60: Beam quality measurement at 150 W output power, including an image of the fiber output imaged onto a camera. The M^2 was measured to be less than 1.2 for both axes.

The Stokes light was also characterized with a high resolution scanning Fabry-Perot (FP), manufactured by Toptica Photonics. Two measurements of particular interest are how the Stokes light narrows in high Brillouin gain situations and what the thermal gradient does to the BGS bandwidth. The etalon is a piezoelectrically scanned confocal Fabry-Perot interferometer, with finesse > 500 and a free spectral range of 1 GHz. The 2 MHz resolution is sufficient to characterize the bandwidth of the Brillouin gain spectrum.

Additionally, the FP was fiber coupled and affixed with a low noise amplified photo-detector for signal measurement. The single frequency NPRO seed laser was used to verify resolution limits and set the appropriate cavity spacing before backward power characterizations were made.

As can be seen from Figure 58, the Rayleigh light is a significant component of the backward light for nearly all amplifier output power levels. A free space solid etalon, having a free spectral range of 69 GHz and FWHM transmission bandwidth of 2.5 GHz, was used to dampen the Rayleigh light. The OSA was used to monitor the backward power spectrum while the solid etalon was angle tuned such that the peak transmission frequency coincided with the peak Stokes frequency of the amplifier. Minor adjustments were made, while the FP was in operation, to ensure the transmission bandwidth of the solid etalon did not modify the measured spectrum. However, this was not a significant concern, given the BGS spectrum was ~ 2 orders of magnitude narrower than the solid etalon FWHM. A typical output of the scanning Fabry-Perot is shown in Figure 61.

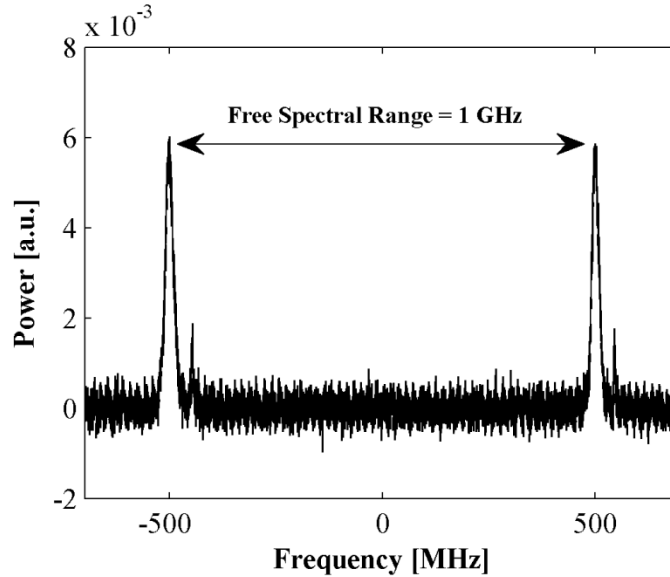


Figure 61: Scanning Fabry-Perot output data captured with an oscilloscope. The Fabry-Perot is adjusted such that two signal resonances are achieved over one scan range. The known cavity free spectral range is used to scale temporal data, given by the oscilloscope, to units of frequency.

The pump-probe BGS measurement showed the Brillouin gain bandwidths, for the reference PCF fiber, of ~ 59 MHz. However, as previously discussed, the SBS process is initiated from thermal noise in the fiber amplifier configuration. The photo-detector affixed to the Fabry-Perot used here requires at least $100 \mu\text{W}$ of signal light for measurements to be made. The losses incurred by the backward traveling light through the solid etalon, used to filter Rayleigh light, and coupling efficiency into the single mode delivery fiber, reduce the Stokes signal significantly. As such, measurements in the low gain regime were not possible and significant narrowing of the Brillouin gain bandwidth is realized in all BGS measurements. A single peak from the Fabry-Perot scan, shown in Figure 61, is shown below.

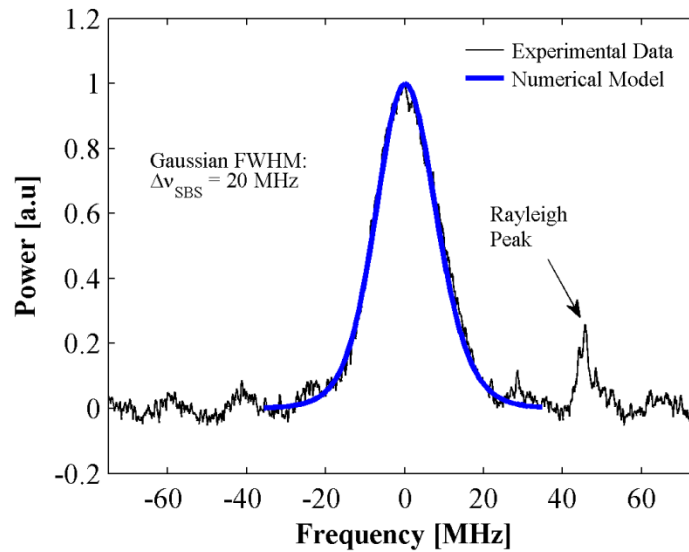


Figure 62: (black) Single Stokes peak as measured by the Fabry-Perot at an amplifier output of 50 W. (blue) The numerical model prediction of the Brillouin gain spectrum is in agreement with experimental data. A Gaussian fit best represents the data, thus it is used to characterize the Brillouin gain bandwidth at 20MHz.

High frequency noise, due to the scanning Fabry-Perot photo-detector, was removed from the data presented in Figure 62 with a simple averaging box filter. This was done to improve visualization of the Gaussian and Lorentzian fits applied, and did not significantly modify the calculated bandwidth. The fiber was held in the water cooled aluminum ring described above, in an attempt to remove any thermal gradient. The amplifier was seeded with 30 W of signal. Approximately 15 W of pump power was input to the amplifier such that the Stokes resonance in the Fabry-Perot was sufficiently above the noise floor of the photo-detector. As expected, the narrowed Brillouin gain bandwidth is best represented by a Gaussian function. The fitting function provides an FWHM bandwidth of 20 MHz, which is significantly smaller than the estimated spontaneous bandwidth of 59 MHz. Additionally, a small amount of Rayleigh light is input to the Fabry-Perot, resulting in the narrow secondary peak indicated in the figure.

The spontaneous bandwidth was estimated with the application of a linear fit to the measured pump-probe Brillouin gain spectrum data. This approximation is sufficient in low Brillouin gain regimes, but does not adequately describe the narrowing as SBS gain increases. In the high gain limit, the FWHM of the Brillouin gain spectrum for a passive fiber is given by [111]

$$\Delta \nu_{SBS} = \frac{\Gamma_B}{2\pi} \sqrt{\ln(2)/G} \quad (3.19)$$

where Γ_B is the spontaneous Brillouin gain bandwidth and G is the product of the peak Brillouin gain, intensity of signal light, and fiber length; $G = g_{SBS} I_L L$.

Experimental data from the pump-probe and Fabry-Perot measurements are combined and compared to the numerical model in Figure 63.

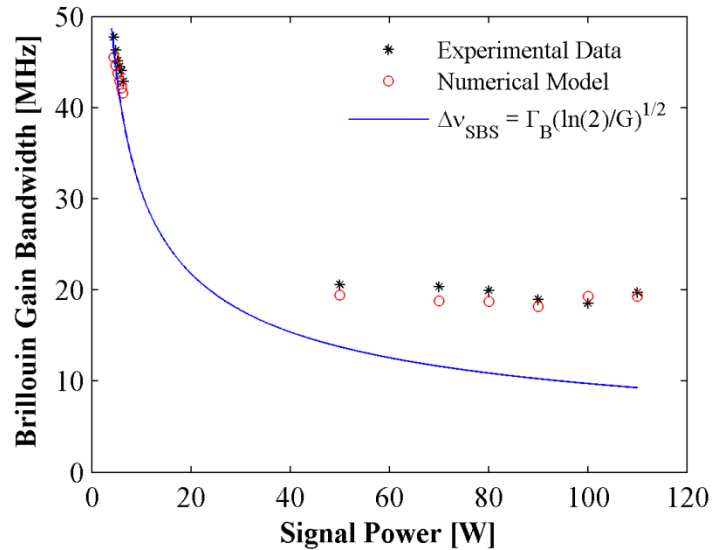


Figure 63: (black asterisk) Experimental measurement of Brillouin gain spectrum as a function of signal power. (red circle) Numerical models prediction. (blue line) A fitting function, which estimates Brillouin gain bandwidth in the high gain regime is plotted to give the general trend of bandwidth narrowing.

The experimental and numerical data is not expected to fit the simple equation since the intensity and the effective Brillouin gain in an amplifier is not uniform along the length of the fiber as it is in a passive fiber. Rather, it is used here to show the general trend of bandwidth narrowing. The experimental and numerical data for BGS bandwidth at high signal powers are in fairly good agreement at high signal powers. Both the model and the Fabry-Perot measurements show negligible thermal gradient over the range of output powers measured. Brillouin gain spectrum measurements at 110 W confirm negligible broadening due a thermal gradient, as shown in Figure 64.

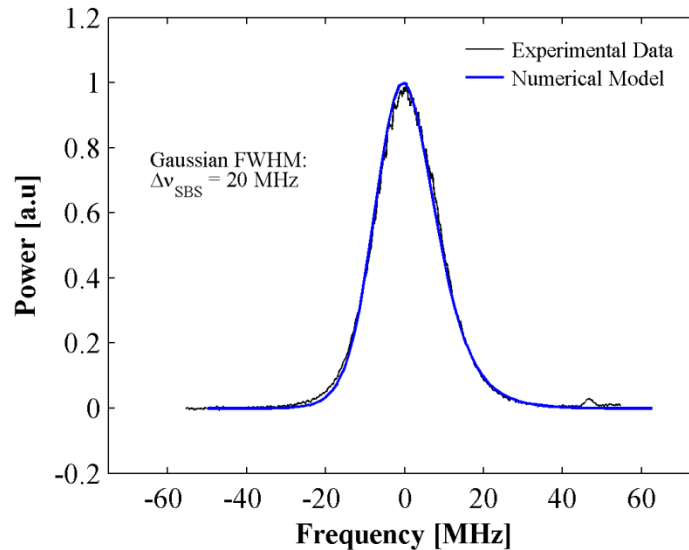


Figure 64: (black) Experimental data for the Brillouin gain spectrum out of the amplifier operating at 110 W output, as measured by the Fabry-Perot. (blue) Numerical model prediction for the same output power.

The Brillouin gain spectrum at 110 W is, again, consistent with the numerical simulation. As the backward power and OSA spectrum plots above indicate, the Stokes light begins to dominate the Rayleigh light, resulting in a small peak to the right of the BGS spectrum. The experimental data shown in Figure 64 was obtained with the

averaging function on the oscilloscope. A single trace corresponded to ~ 100 ms, and 16 traces were averaged to reduce noise in the data. This same technique was used in characterizing the NRPO seed laser, which requires the Fabry-Perot to operate at the resolution limit, to ensure frequency drift over the measurement time did not artificially broaden the spectrum.

Under the conditions described above, the reference PCF showed an SBS threshold of ~ 150 W. This is the baseline, by which the SAT fiber will now be judged. An amplifier, having the same parameters as those described for the reference PCF was made, using the SAT gain fiber.

The SAT fiber is similar to the reference PCF with a nominal core diameter and mode field diameter (MFD) of 39.5 and 30 μm , respectively and numerical aperture of 0.03. Stress inducing rods composed of borosilicate and running along the fiber axis ensured that the fiber was PM. The inner cladding had a diameter of ~ 329 μm with a numerical aperture of 0.6. The diameter of the air holes in the cladding were approximately 2 μm with a pitch of 10 μm and extended to approximately 55 μm from the center of the fiber. The outer cladding was 580 μm in diameter and was surrounded by a high temperature acrylate that was approximately 61 μm in thickness. The small signal absorption, which is slightly lower than the reference fiber, was measured to be 3.9 dB/m for a pump wavelength of 976 nm. This is due to the modifications in dopant levels, particularly aluminum. NKT Photonics requires a specific ratio of ytterbium to aluminum for the mitigation of photodarkening. As described in a previous section, the SAT design calls for variation of aluminum concentration in the central segment and outer ring regions. A reduction of aluminum concentration in the outer ring dictates a

comparable reduction in ytterbium concentration. The difference in absorption is negligible under the experimental conditions of this test, as the 10 meter fiber length provides efficient pump absorption. One might claim the difference in pump absorption would change to dynamics of signal growth in the fiber. However, a reduction in pump absorption would tend to decrease the naturally imposed thermal gradient ultimately reducing the SBS threshold. This effect is also negligible and for all intents and purposes, the two fibers are considered identical, save the acoustic tailoring. As was done for the reference PCF amplifier, the SBS threshold was characterized with the standard technique of identifying the departure of linear growth in backward power with increasing signal power. The numerical model was used to simulate the amplifier signal and backward power output. The experimental data and numerical results for the signal output power are shown in Figure 65 below.

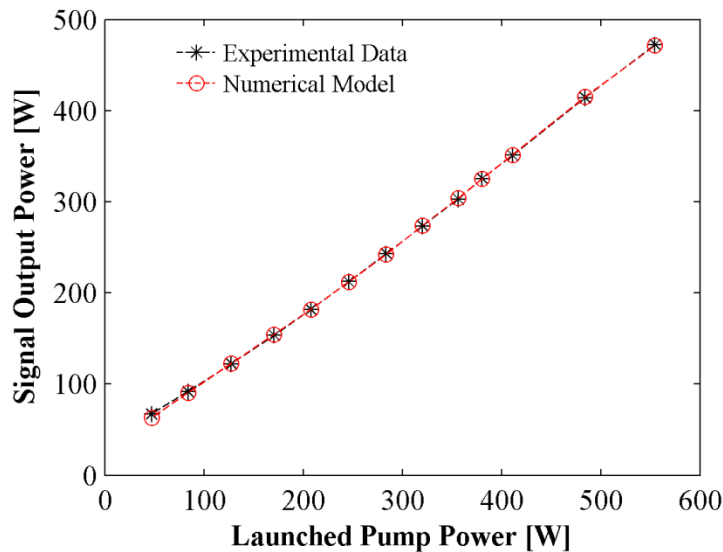


Figure 65: (black asterisk) Experimental data for signal output power vs. launched pump power from 10 meter reference photonic crystal fiber amplifier. (red circle) The numerical model prediction for output power of the amplifier.

An output power of 470 W was achieved, which was not limited by SBS. The polarization extinction ratio was measured to be better than 17 dB at all power levels up to 395 W. The numerical model is in very good agreement with the experimental data. The variation in center pump wavelength with increasing power, as shown in Figure 55, was input to the model along with an absorption coefficient of 3.1 dB/m. As was seen in the reference PCF, the absorption coefficient differs from the quoted 3.9 dB/m, which is measured for small signal 976 nm pump light. This value was obtained experimentally by estimating coupled pump power and measuring unabsorbed pump.

The backward power was measured by imaging the PCF core into a 6 μm , single-mode fiber, which is used as a spatial filter. The numerical model, backward power measurements, and OSA spectrums are all used to validate the qualitative increase in Stokes light for the SAT PCF amplifier. Figure 66 shows the backward power measured, and the numerical model prediction.

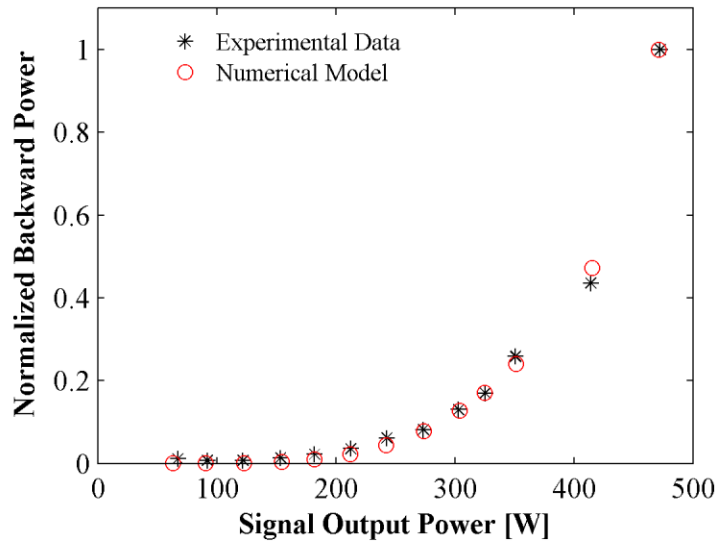


Figure 66: (black asterisk) Experimental data for backward power as a function of output signal power, showing a departure from linear growth. (red circle) The numerical model prediction for backward power.

Measurements from the SAT amplifier do not show a rapid increase in backward power, as was seen in the reference fiber. Rather, a more gradual increase over $\sim 200\text{W}$ range of signal output power is observed. Again, this behavior is mirrored by the data from the numerical model. The model and experimental data are normalized to their respective maximum values for a qualitative comparison. At the highest output power, the model showed a reflectivity of $\sim 0.005\%$, indicating the amplifier is not operating near the SBS threshold.

The backward power was sampled with a Faraday rotator and polarization beam splitting cube, similar to the technique used for the pump-probe BGS measurement. The sampled light was imaged into the core of a single mode delivery fiber, which was then split by a 50/50 fused fiber coupler. A high resolution optical spectrum analyzer was used to capture the relative ratio between the Stokes and Rayleigh scattered light

simultaneously with the backward power measurements shown above. Three power levels are shown in Figure 67, which show a substantial growth in Stokes light relative to the linearly increasing Rayleigh scattered light up to ~200 W output power. The growth in Stokes light is inhibited beyond 200 W output power due to the introduction of a quantum defect induced thermal gradient.

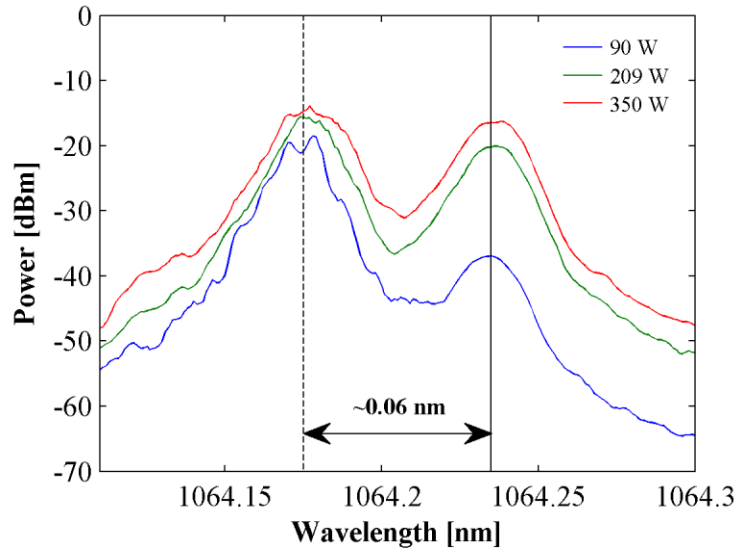


Figure 67: Optical spectrum analyzer data for reference PCF amplifier at three power levels. The peak associated with Rayleigh scattered light is indicated by the vertical dotted black line. The Stokes scattered light is indicated with the vertical solid black line. The peak separation is ~ 0.06 nm, corresponds to ~ 16 GHz at 1064 nm.

The OSA data is consistent with the backward power measurements shown in Figure 66 in that the Stokes scattered light grows relatively slowly over the range between 200 and 350 Watts. At low pump powers, e.g. 90 – 200 W, a significant growth in Stokes light is realized. In this pump power regime, as seen in the reference fiber, the thermal gradient is insignificant. However, the Stokes light dominated the Rayleigh light at 100 W output for the reference fiber amplifier. The SBS suppressive nature of the acoustically tailored core, relative to the reference PCF, allows for operation beyond

power levels where the thermal gradient is insignificant; i.e. the acoustically tailored core and thermal gradient work in conjunction to increase the SBS threshold of the amplifier.

Fabry-Perot measurements of the Brillouin gain spectrum are more telling, regarding the nature of the thermal gradient at different output powers of the amplifier. In all measurements, the fiber was held in the water cooled aluminum ring described above, in an attempt to remove any thermal gradient. The amplifier was seeded with 30 W of signal. Approximately 120W of pump power was input to the amplifier such that the Stokes resonance in the Fabry-Perot was sufficiently above the noise floor of the photo-detector. The signal to noise was also improved by using the averaging function on the oscilloscope. Figure 68 is a Fabry-Perot measurement taken for the SAT amplifier operating at 120 W output power. As seen in the reference fiber, negligible broadening due to a thermal gradient is observed at this power level.

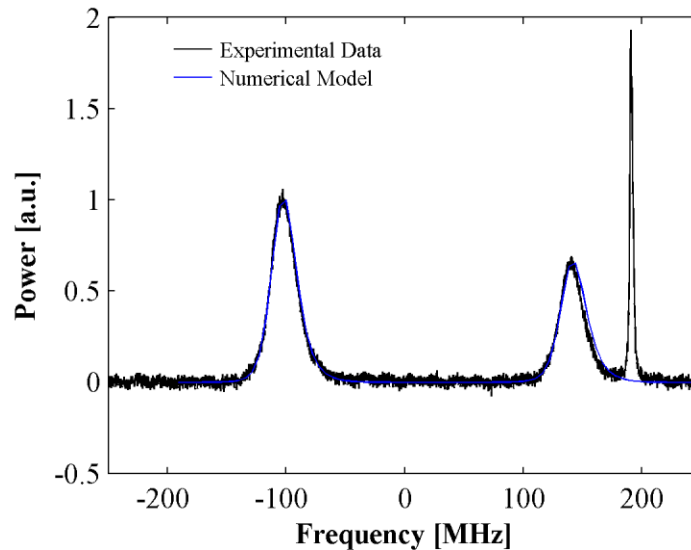


Figure 68: (black) Experimental data for the Brillouin gain spectrum out of the amplifier operating at 110 W output, as measured by the Fabry-Perot. (blue) Numerical model prediction for the same output power.

As expected, the narrowed Brillouin gain bandwidth results in two distinct Brillouin peaks of Gaussian lineshape. The ratio of peak heights is similar to that measured by the pump-probe, at approximately 0.7, where the larger peak is attributed to the outer ring of the SAT fiber core, and the smaller peak is associated with the central segment. The backward power is dominated by Rayleigh light at the amplifier output power, thus a large Rayleigh peak is also measured by the Fabry Perot. Each peak bandwidth is approximately 24 MHz. The Rayleigh peak is ~ 2 MHz, which is the resolution limit of the Fabry-Perot. The separation between the peaks is approximately 240 MHz, which is ~ 20 MHz larger than the pump-probe BGS measurements. One potential explanation for this is small variations in core dopant concentration between the fiber draws provided by NKT photonics. The pump-probe measurements were made on a pilot fiber draw, provided by NKT photonics for testing, before the final draw. The BGS measurements shown above were made on the final fiber draw which was made 3 months later. It should be noted that the pump-probe and Fabry-Perot measurements shown here are done on the final draw of the reference fiber. Recall from the pump-probe measurements, the BGS peak attributed to the central segment in the SAT fiber was consistent, in shift frequency, to that measured for the reference fiber. This is also observed in the Fabry-Perot measurements by using the Rayleigh light as a benchmark. The free spectral range of the Fabry-Perot (1 GHz) is not large enough to measure the separation between the Stokes and Rayleigh peaks (~ 16 GHz). However, the confocal Fabry-Perot will resonate frequencies meeting the criteria, $\nu = Nc/4d$, where d is the spacing between the cavity mirrors, N is an integer, and c is the speed of light. The proximity of the reference fiber and smaller SAT fiber BGS peaks to the Rayleigh peak

indicate they are similar in frequency. It is reasonable, therefore, to assume the discrepancy in pump-probe and Fabry-Perot BGS measurements is due to small variations in the dopants used in the outer ring of the SAT fiber core. As previously shown, the acoustic velocity is much more sensitive to variations in dopant concentration than optical index of refraction. A change in Brillouin shift frequency of 20 MHz corresponds to ~0.2% change in acoustic velocity. The dopant configuration in the outer ring involves germanium, aluminum, fluorine, and ytterbium. There are numerous combinations of these dopants which could produce such a small change in acoustic velocity, while maintaining optical uniformity. Therefore, it is not surprising to see slight variations in fibers drawn at different times.

Despite the attempt at cooling the fiber, a significant thermal gradient is induced along the length of the fiber as pump power was increased. In principle the numerical model should be able to account for the thermal broadening of the Brillouin gain spectrum. However, the experimental conditions are such that two distinct cooling regions exist along the fiber length. One region of the fiber is suspended in air, subject to free convective cooling. The rest of the fiber is conductively cooled by the aluminum ring. This complicates the theoretical analysis as the numerical model does not consider conductive cooling. The conductive cooling was approximated by creating an effective cooling coefficient for the length of fiber held by the aluminum ring. It is well known, free convection supplies a cooling coefficient in the range $h = 5-25 \text{ W/m}^2\text{K}$. The effective cooling coefficient of the aluminum ring was optimized by first characterizing the shift in Brillouin gain spectrum, as measured by the Fabry-Perot, for a range of fiber

amplifier output powers. Four Brillouin gain spectrums are shown in Figure 69, corresponding to a 360 W output power range.

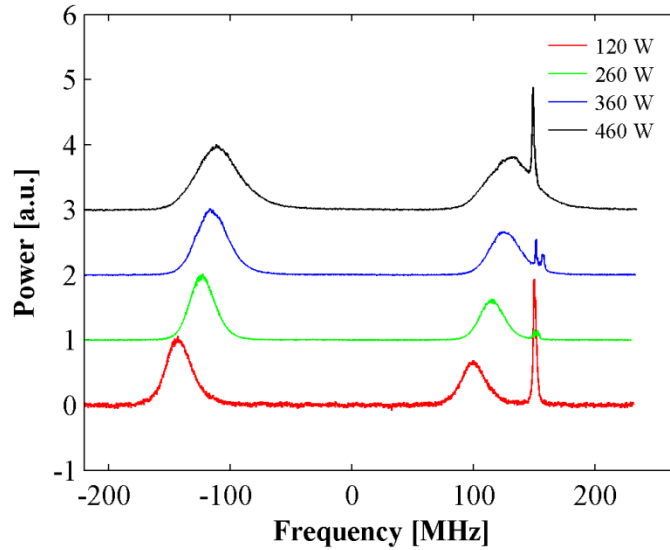


Figure 69: Brillouin gain spectrum for the segmented acoustically tailored fiber at various power levels. Each spectrum is referenced to the Rayleigh light peak to show shift due to the thermal gradient established in the fiber.

The Brillouin gain spectra above are referenced to the Rayleigh scattered light, which does not shift with temperature. In this way the shift with increasing power is better visualized. A large shift in frequency of the peak Brillouin gain is measured between 120 W and 260 W fiber amplifier output powers. As the power increases above 260 W, the shift in peak Brillouin gain reduces, and the Brillouin gain bandwidth of each peak is broadened. The optimized effective cooling coefficient for the aluminum ring was found to be in the range, $h_{eff} = 202\text{-}212$. Brillouin gain spectrum predictions from the numerical model for the same amplifier output powers are shown in Figure 70.

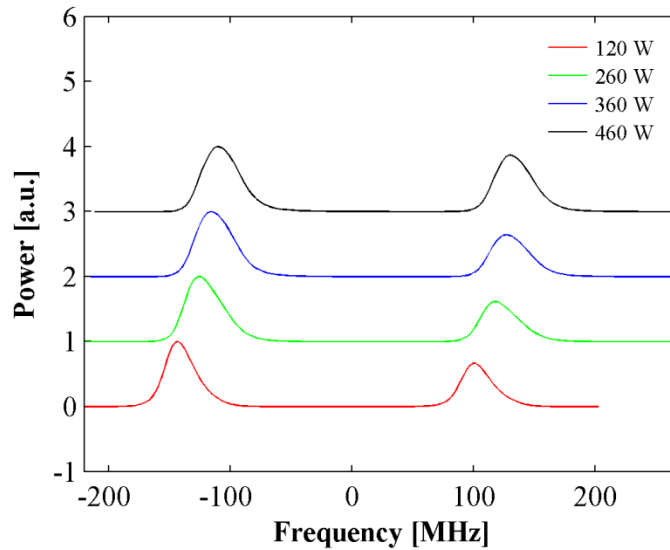


Figure 70: Brillouin gain spectrum prediction by the numerical model after optimization of the effective cooling coefficient for the aluminum ring. A free convection cooling coefficient, $h \approx 5 \text{ W/m}^2\text{K}$, was used for the fiber suspended in air. An effective cooling coefficient, $h_{\text{eff}} \approx 200 \text{ W/m}^2\text{K}$, was used for the fiber held in the aluminum ring.

Using the optimized effective cooling coefficient for the fiber held in the aluminum ring reproduces the qualitative behavior of the experimental data. It is difficult to make accurate measurements of the fiber core temperature experimentally. However, the numerical model provides some insight into how and why this behavior is observed. Figure 71 shows the numerical model prediction for the average core temperature along the length of the fiber.

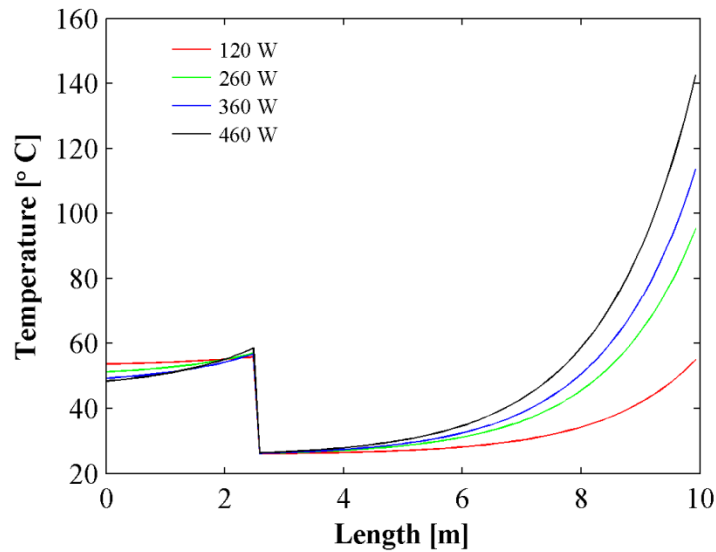


Figure 71: Average core temperature as a function of fiber length given by the numerical model. The fiber is cooled by free convection from 0-2.5 meters. The rest of the fiber, 2.5-10 meters, is cooled more efficiently by the aluminum ring.

The numerical model shows the effect of two distinct cooling regions having much different cooling coefficients. The fiber length left suspended in air (0-2.5 meters) is subject to free convective cooling with a cooling coefficient $h \approx 5 \text{ W/m}^2\text{K}$. The fiber held in the aluminum ring is conductively cooled with an effective cooling coefficient $h_{eff} \approx 200 \text{ W/m}^2\text{K}$. In the figure above, the pump is input from the right side. As such, absorption and subsequently quantum defect heat is highest in this region. Notice a significant increase in temperature between 120 W and 260 W output power near the end (10 meters) of the fiber. This is responsible for the large shift in peak Brillouin gain frequency observed in the Fabry-Perot measurements. As the signal power increases beyond 260W the model shows smaller jumps in maximum temperature, but an increase in $\Delta T/\Delta L$. This effect is responsible for broadening the Brillouin gain spectrum since the peak Brillouin gain is changing rapidly in the longitudinal direction. The pump

absorption in the fiber is substantial leading to negligible quantum defect heating in the first 2.5 meters of fiber.

The high resolution optical spectrum analyzer was also used to characterize amplified spontaneous emission in the amplifier output, and to ensure all signal power measured was due to 1064 nm radiation, shown in Figure 72.

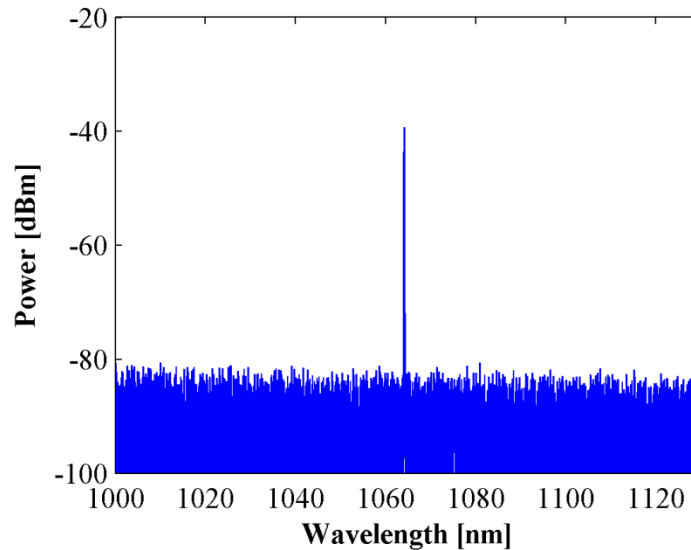


Figure 72: Optical spectrum analyzer data for reference PCF amplifier at 350 W output power. The single peak, at 1064 nm is over 40 dBm above the noise floor, indicating negligible amplified spontaneous emission.

The data shown in Figure 72 was obtained by imaging scattered light from the power meter, measuring the amplifier output, into a 50 μm core, multimode optical fiber. The large core diameter was required to obtain sufficient signal to noise ratio. The fiber was input to the optical spectrum analyzer for analysis.

3.7.1. Power Dependent Modal Instabilities

As power levels increased above 400 W, the beam quality began to degrade, with a final value of $M^2 = 1.5$ at 490 W output. This degradation in beam quality has been seen previously, in work presented here, but was attributed to non-optimal waveguide design. Upon further investigation, the transverse optical mode was found to hop between the fundamental (LP_{01}) and next higher order (LP_{11}) modes. Near field images of the optical mode above and below the mode hopping threshold are shown in Figure 73.

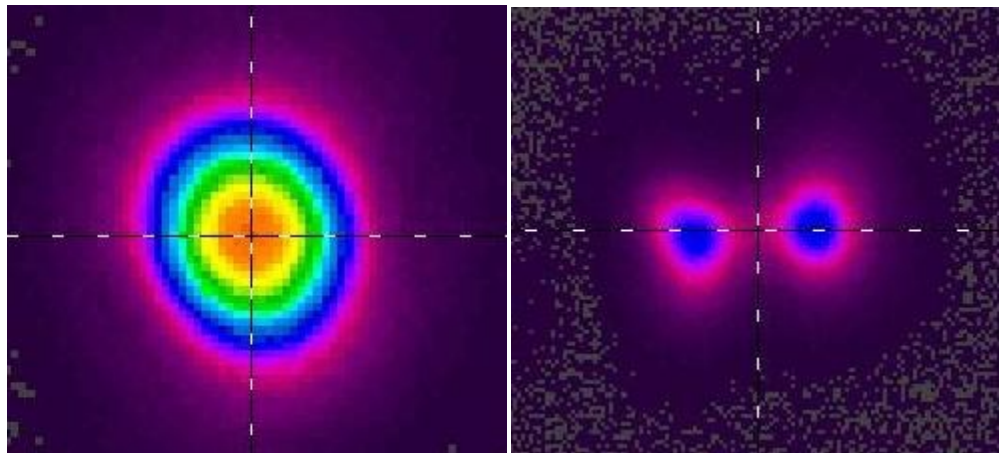


Figure 73: (left) Near field image of PCF amplifier operating at 300 W output power, leading to an $M^2 < 1.3$. (right) Near field image of PCF amplifier operating above 490 W, leading to $M^2 > 1.5$.

Recently, the same effect has been reported by groups operating narrow linewidth CW and pulsed PCF amplifiers in the kW average power regime.[62,112] In both cases, the authors attribute this effect to transverse spatial hole-burning. Within the context of a fiber amplifier, spatial hole-burning refers to a power dependent transverse saturation of the laser gain in the core. Assuming fundamental mode operation, the center of the core would tend to saturate first, due to the intensity profile of that particular optical mode. This gives rise to increased gain for higher order modes have better overlap with

unsaturated regions of the core. In Ref. [62], a CW narrow linewidth PCF amplifier was limited to ~ 1.2 kW by the onset of transverse mode hopping (TMH). Below the TMH threshold the beam quality was $M^2 < 1.3$. The fiber used in that demonstration was a Yb-doped photonic crystal fiber having a $42\ \mu\text{m}$ core diameter ($33\ \mu\text{m}$ MFD) and $500\ \mu\text{m}$ pump cladding diameter. The authors confirm the spatial hole-burning hypothesis by using higher seed power to shift the TMH threshold to 1.8 kW. The seed power was increased from ~ 30 W, which produced the 1.3 kW TMH limited output, to ~ 200 W, giving the 1.8 kW result. Increasing the seed power also required additional broadening of the seed laser linewidth in order to suppress SBS, since the average power in the fiber is significantly increased by a 200 W seed power. The linewidth at the 30 W seed level was measured to be ~ 25 GHz. The laser linewidth was not reported for the 200 W seed level.

Increasing the seed power is not a particularly attractive solution to the TMH issue, since it tends to reduce the SBS threshold of the amplifier. Additionally, it is peculiar the TMH threshold observed in this work is found at half the output power levels observed by other groups. Conventional thinking, regarding higher order mode content in fiber amplifiers, would dictate a decrease in coil diameter and/or modification to the free space seeding conditions. It is conceivable the fiber is not inherently single mode, and a small fraction of the coupled seed light is guided in the higher order mode. These parameters were modified, and proved to have negligible effect on the TMH threshold. Having ruled out issues with amplifier design, a comparison of the photonic crystal gain fiber used here and that presented in Ref. [62] is made. The fibers are similar in most ways except pump cladding diameter. The fiber used here has a $\sim 320\ \mu\text{m}$, while the fiber

used in Ref. [62] had a 500 μm cladding. This difference results in much different pump absorptions, and subsequently, different thermal loading due to quantum defect heating.

3.7.2. Transverse Mode Hopping: Thermal Dependence

An experimental investigation was conducted to see if the TMH threshold was related to fiber temperature. A fiber amplifier was constructed and operated under two cooling conditions. In one test, the fiber was suspended in air, such that the fiber was subject to convective cooling of air. This experimental condition corresponds to a convective cooling coefficient in the range of $h = 5\text{-}25 \text{ W/m}^2\text{K}$. The second test made use of the aluminum ring, which provided conductive cooling to the fiber, with an effective cooling coefficient in the range of $h_{\text{eff}} = 202\text{-}212 \text{ W/m}^2\text{K}$. Cold plates were affixed to the aluminum ring, as was done in the amplifier demonstration described in the previous section. It has been shown above, as well as in the literature, heat transfer through conduction is a much more efficient means of cooling the fiber.[27] Figure 74 below, shows beam quality results for a PCF gain fiber which is conductively cooled, and left suspended in air.

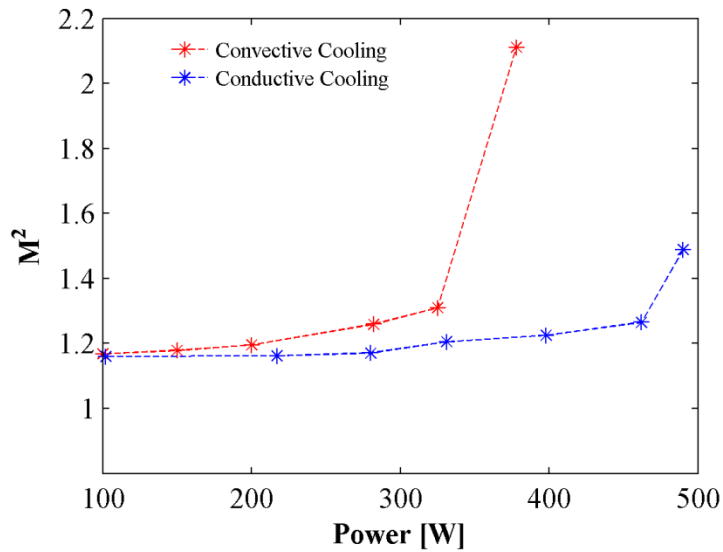


Figure 74: Beam quality as a function of output power for a PCF amplifier which is (blue asterisk) conductively cooled and (red asterisk) left suspended in air, with no external cooling applied.

Cooling the fiber does appear to have a significant impact on the beam quality at increasing power levels. However, as discussed previously, some amount of thermal gradient along the length of the fiber is desirable for SBS mitigation. The results presented here represent a relatively inefficient attempt at cooling the fiber. The cold plates affixed to the top and bottom of the aluminum ring did not provide the most efficient means of transferring heat from the aluminum. Heat generated by the fiber amplifier in extended high power operation was sufficient to raise the temperature of the aluminum ring by as much as 20° C above room temperature, despite the cooling supplied by the cold plates.

Clearly the transverse mode hopping issue is more complicated than the simple explanation of spatial hole-burning. The work presented here, and in the literature shows a distinct power dependent regime where TMH is observed. At low powers, the amplifier

appears to be operating primarily in the fundamental mode. Thus, the mode hopping observed at higher powers, must be the result of scattering from the fundamental mode to higher order modes. Since the fundamental mode is assumed to be azimuthally symmetric, scattering to a higher order mode may only be achieved when the transverse optical index of refraction is azimuthally asymmetric. Consider the nonlinear wave equation for an arbitrary refractive index distribution:

$$\nabla^2 E - \frac{n(x, y, z)^2}{c^2} \frac{\partial^2}{\partial t^2} E = \frac{1}{\epsilon_0 c^2} \frac{\partial^2}{\partial t^2} P^{(nl)} \quad (3.20)$$

where the index of refraction is assumed to be composed of the background refractive index, n_0 , plus some change Δn , such that, $n^2 = (n_0 + \Delta n)^2 \approx n_0^2 + 2n_0\Delta n$. Assuming the wave equation has solutions of the form:

$$E(\vec{r}, t) = \sum_j (1/2) A_j(z) \phi_j(x, y) \exp[i(\beta_j z - \omega t)] + c.c \quad (3.21)$$

where ϕ , A , and β are the transverse profile, amplitude, and propagation constant of the j^{th} optical mode. The amplitude equation for the j^{th} mode is represented as:

$$\frac{dA_j}{dz} = \frac{in_0\omega^2}{c^2\beta_j} \sum_i A_i \exp[i(\beta_i - \beta_j)z] \kappa_{\Delta n} + \frac{1}{2} \sum_i A_i \exp[i(\beta_i - \beta_j)z] \kappa_{LG} \quad (3.22)$$

Here the coupling coefficients $\kappa_{\Delta n}$ and κ_{LG} are defined as overlap integrals of the form,

$$\kappa_{\Delta n} = \frac{\iint \phi_j^* \Delta n(x, y, z) \phi_i dx dy}{\iint |\phi_j|^2 dx dy} \quad (3.23)$$

$$\kappa_{LG} = \frac{\iint \phi_j^* (N_2(x, y, z) \sigma^e - N_1(x, y, z) \sigma^a) \phi_i^* dx dy}{\iint |\phi_j|^2 dx dy} \quad (3.24)$$

The general formulation of the amplitude equation above describes the mechanism by which light may be scattered between optical modes. The scattering is manifest as a coupling between modes due to laser gain, which is described by the coupling coefficient κ_{LG} , or through non-uniform optical index of refraction, described by $\kappa_{\Delta n}$. Spatial hole-burning is accounted for in Eq. (3.24) when $i = j$, i.e. a consideration of the radial laser gain profile experienced by a single optical mode. The optical modes which satisfy the wave equation form a complete orthogonal set, thus the coupling coefficients are only non-zero if the laser gain or refractive index break the symmetry of the overlap integral. In principal, there are a number of physical phenomena through which this may be accomplished. This formulation of the problem is sufficiently generic to capture a number of these mechanisms including spatial hole-burning and temperature related changes in the optical index of refraction. However, this analysis is left for future work for researchers in the field of high power fiber amplifiers.

CHAPTER 4

Conclusion

4.1. Summary of Results

This dissertation presents experimental and theoretical studies of high power, single-frequency, ytterbium-doped photonic crystal fiber amplifiers. The objective of this effort is to identify issues which limit power scaling and develop novel techniques to overcome these limitations. Historically, stimulated Brillouin scattering has been the primary obstacle in the realization of high power single-frequency fiber amplifiers. To address this issue, a novel segmented acoustically tailored (SAT) photonic crystal fiber was designed to increase the SBS threshold beyond commercially available fibers. The fiber design is such that it may be used in conjunction with other SBS mitigation techniques, which increases the nonlinear threshold beyond the current state of the art. A pump-probe Brillouin gain spectrum measurement was performed on the SAT fiber and compared to a commercially available photonic crystal fiber as a baseline reference. A peak Brillouin gain coefficient of 1.2×10^{-11} was observed for the SAT fiber, which approximately 1.8 times lower than that measured in the reference fiber.

The SAT and reference fibers were then implemented in an amplifier configuration to investigate the improvement in SBS threshold due to the acoustically tailored core. The amplifier design called for a 10 meter gain fiber, which was seeded at approximately 30 W. The diode laser used to pump the photonic crystal fiber amplifier

was thermally detuned off the 976 nm Yb absorption peak to ~972 nm. This was done to reduce pump absorption, resulting in a more uniform longitudinal thermal profile.

Additionally, attempts were made to cool the fiber which limited the longitudinal thermal gradient, due to quantum defect heating, established in the fiber. Under these conditions, the reference fiber was found to be limited by SBS at an output power of 150 W. The SAT fiber was scaled to 490 W output power, with near diffraction limited beam quality. Power scaling beyond this resulted in beam quality degradation, manifesting as mode hopping between the two lowest order transverse modes. Based on the Brillouin gain coefficient measurements, one would expect the SAT fiber to be SBS limited at ~300 W, i.e. twice the threshold observed for the reference fiber. High resolution Fabry-Perot measurements of the SAT fiber amplifier Brillouin gain spectrum showed the increased threshold was due to the introduction of a thermal gradient at power levels above 250 W. The introduction of a thermal gradient at increasing output powers complicates a quantitative comparison between the SAT fiber and reference fiber. However, the acoustically tailored core clearly shows SBS suppression in that the SAT fiber operated above the power limit of the reference fiber.

4.2. Future Work

In the successful suppression of SBS, a new regime of single-frequency photonic crystal fiber amplifier power scaling is explored. A new phenomenon, transverse mode hopping, is observed at increasing output powers. Mitigation of this effect is demonstrated experimentally by reducing the fiber temperature. This empirical data is

used as the basis for a theoretical framework with which the problem may be analyzed. This theoretical treatment, based on coupled mode theory, shows transverse mode hopping may only occur if the optical index of refraction develops asymmetry relative to the fundamental optical mode. For now, power scaling single-frequency fiber amplifiers to the kW regime requires analysis and solution of this limitation.

REFERENCES

1. D. J. Richardson, J. Nilsson, W. A. Clarkson, "High power fiber lasers: current status and future perspectives," J. Opt. Soc. Am. B **27**, B63-B92 (2010).
2. E. Snitzer, "Proposed fiber cavities for optical masers," J. Appl. Phys. **32**, 39-39 (1961)
3. H. W. Etzel, H. W. Gandy, R. J. Ginther, "Stimulated emission of infrared radiation from ytterbium activated silicate glass," Appl. Opt. **1**, 534-536 (1962).
4. E. Snitzer, "Optical maser action of Nd³⁺ barium crown glass," Phy. Rev. Lett. **7**, 444-446 (1964).
5. K. C. Kao, G. A. Hockham, "Dielectric-fibre surface waveguides for optical frequencies," Proc. IEEE, **133**, 191-198 (1966).
6. F. P. Kapron, D. B. Keck, R. D. Maurer, "Radiation losses in glass optical waveguides," Appl. Phys. Lett. **17**, 423-425 (1970).
7. H. Kanamori, H. Yokota, G. Tanaka, M. Watanabe, Y. Ishiguro, I. Yoshida, T. Kakii, S. Itoh, Y. Asano, S. Tanaka, "Transmission characteristics and reliability of pure silica-core single mode fibers," IEEE J. Lightwave Tech. **LT-4**, 1144-1150 (1986).
8. R. J. Mears, L. Reekie, I. M. Jauncey, and D. N. Payne, "Low-noise erbium doped fiber amplifier operating at 1.54 um," Electron. Lett. **23**, 1026-1028 (1987).
9. L. Jeunhomme, M. Monerie, "Polarisation-maintaining single-mode fibre cable design," Electron. Lett. **16**, 921-922 (1980).
10. J. Noda, O. Katsunari, Y. Sasaki, "Polarization-maintaining fibers and their applications," J. Lightwave Tech. **LT-4**, 1071-1089 (1986).
11. Y. Sasaki, K. Okamoto, T. Hosaka, N. Shibata, "Polarization-maintaining and absorption-reducing fibres," in *Optical Fiber Communication*, OSA Technical Digest, paper ThCC6, (1982).
12. Y. Sasaki, T. Hosaka, J. Noda, "Low-loss polarization maintaining optical fibre with low crosstalk," Electron. Lett. **21**, 156-157 (1985).
13. E. Snitzer, "Rare earth fiber lasers," J. Less-Common Metals **148**, 45-58 (1989).
14. E. Snitzer, H. Po, F. Hakimi, R. Tumminelli, B. C. McCollum, "Double clad, offset core Nd fiber laser", in *Optical Sensors Conf. (OFC)*, paper PD5, (1988).
15. M. L. Osowski, W. Hu, R. M. Lammert, S. W. Oh, P. T. Rudy, T. Stakelon, J. E. Ungar, "Advances in high-brightness semiconductor lasers," Proc. SPIE **6876**, 68761E1 (2008).
16. D.W. Hughes, J.R.M Barr, "Laser diode pumped solid state lasers," J. Phys. D: Appl. Phys. **25**, 563-586 (1991).

17. I. M. Jauncey, J. T. Lin, L. Reekie, R. J. Mears, "Efficient diode-pumped cw and q switched single-mode fibre laser," *Electron. Lett.* **22**, 198-199 (1986).
18. T. J. Whitley, "Laser diode pumped operation of Er³⁺-doped fibre amplifier," *Electron. Lett.* **24**, 1537-1539 (1988).
19. L. F. Mollenauer, E. Lichtman, G. T. Harvey, M. J. Neubelt, B. M. Nyman, "Demonstration of error free soliton transmission over more than 15,000 km at 5 Gbit/s, single channel, and over 11,000km at 10 Gbit/s in a two channel WDM," *Electron. Lett.* **28**, 792-794 (1992).
20. W. J. Miniscalco, "Erbium-doped glasses for fiber amplifiers at 1500 nm," *J. Lightwave Tech.* **9**, 234-250 (1991).
21. M. J. F. Digonnet, *Rare-Earth-Doped Fiber Lasers and Amplifiers, 2nd Edition* (Marcel Dekker 2001).
22. E. Desurvire, C. R. Giles, J. R. Simpson, J. L. Zyskind, "Efficient erbium-doped fiber amplifier at a 1.53- μ m wavelength with a high output saturation power," *Opt. Lett.* **14**, 1266-1268 (1989).
23. P. Blixt, J. Nilsson, T. Carlnäs, B. Jaskorzynska, "Concentration-dependent upconversion in Er³⁺-doped fiber amplifiers: experiments and modeling," *IEEE Trans. Photon. Tech. Lett.* **3**, 996-998 (1991).
24. J. Nilsson, P. Blixt, B. Jaskorzynska, J. Babonas, "Evaluation of parasitic upconversion mechanisms in Er³⁺-doped silica-glass fibers by analysis of fluorescence at 980 nm," *J. Lightwave Tech.* **13**, 341-349 (1995).
25. F. Auzel, "Upconversion processes in coupled ion systems," *J. Lumin.* **45**, 341-345 (1990).
26. J. F. Massicott, R. Wyatt, B. J. Ainslie, S. P. Craig-Ryan, "Efficient, high power, high gain Er³⁺-doped silica fibre amplifier," *Proc. SPIE* **1373**, 93-102 (1990).
27. V. Kuhn, D. Kracht, J. Neumann, P. Weßels, "67 W of output power from an Yb-free Er-doped fiber amplifier cladding pumped at 976 nm," *IEEE Photon. Tech. Lett.* **23**, 432-434 (2011).
28. Y. Jeong, J. K. Sahu, D. B. S. Soh, C. A. Codemard, J. Nilsson, "High-power tunable single-frequency single-mode erbium:ytterbium codoped large-core fiber master-oscillator power amplifier source," *Opt. Lett.* **30**, 2997-2999 (2005).
29. D. C. Hanna, R. M. Percival, I. R. Perry, R. G. Smart, P. J. Suni, J. E. Townsend, A. C. Tropper, "Continuous-wave oscillation of a monomode ytterbium-doped fibre laser," *Electron. Lett.* **24**, 1111-1113 (1988).
30. H. M. Pask, R. J. Carman, D. C. Hanna, A. C. Tropper, C. J. Mackechnie, P. R. Barber, J. M. Dawes, "Ytterbium-doped silica fiber lasers: versatile sources for the 1-1.2 μ m region," *IEEE J. Select. Topics Quantum Electron.* **1**, 2-13 (1995).
31. R. Paschotta, J. Nilsson, A. C. Tropper, D. C. Hanna, "Ytterbium-doped fiber amplifiers," *IEEE J. Quantum Electron.* **33**, 1049-1056 (1997).
32. J. J. Koponen, M. J. Söderlund, H. J. Hoffman, S. K. T. Tammela, "Measuring photodarkening from single-mode ytterbium doped silica fibers," *Opt. Express* **14**, 11539-11544 (2006).
33. N. Edagawa, K. Mochizuki, H. Wakabayashi, "1.2 Gbit/s, 218 km transmission experiment using inline Er-doped optical fibre amplifier," *Electron. Lett.* **25**, 363-364 (1989).

34. K. O. Hill, Y. Fujii, D. C. Johnson, B. S. Kawasaki, "Photosensitivity in optical fiber waveguides: Application to reflection filter fabrication," *Appl. Phys. Lett.* **32**, 647-649 (1978).
35. E. J. Friebele, D. L. Griscom, "Color centers in glass optical fiber waveguides," *Mat. Res. Soc. Symp. Proc.* **61**, 319-331 (1986).
36. L. J. Poyntz-Wright, P. St. J. Russell, "photochromic dynamics and nonlinear transmission at modulated cw blue/green wavelengths in germanosilicate optical fibers," *Electron. Lett.* **24**, 1054-1055 (1988).
37. M. M. Broer, J. R. Simpson, D. J. DiGiovanni, "studying pump light-induced darkening in erbium-doped fiber amplifiers with optical time domain reflectometry," *IEEE Photon. Tech. Lett.* **4**, 1264-1266 (1992).
38. C. A. Millar, S. R. Mallinson, B. J. Ainslie, S. P. Craig, "Photochromic behaviour of thulium-doped silica optical fibres," *Electron. Lett.* **24**, 590-591 (1988).
39. G. R. Atkins, A. L. G. Carter, "Photodarkening in Tb³⁺-doped phosphosilicate and germanosilicate optical fibers," *Opt. Lett.* **19**, 874-876 (1994).
40. M. M. Broer, R. L. Cone, J. R. Simpson, "Ultraviolet-induced distributed-feedback gratings in Ce³⁺-doped silica optical fibers," *Opt. Lett.* **16**, 1391-1393 (1991).
41. E. G. Behrens, R. C. Powell, D. H. Blackburn, "Characteristics of laser induced gratings in Pr³⁺- and Eu³⁺-doped silicate glasses," *J. Opt. Soc. Am. B* **7**, 1437-1444 (1990).
42. R. Paschotta, J. Nilsson, P. R. Barber, J. E. Caplen, A. C. Tropper, D. C. Hanna, "Lifetime quenching in Yb-doped fibres," *Opt. Comm.* **136**, 375-378 (1997).
43. V. Dominic, S. MacCormack, R. Waarts, S. Sanders, S. Bicknese, R. Dohle, E. Wolak, P. S. Yeh, E. Zucker, "110 W fibre laser," *Electron. Lett.* **35**, 1158-1160 (1999).
44. K. Arai, H. Namikawa, K. Kumata, T. Honda, "Aluminum or phosphorus co-doping effects on the fluorescence and structural properties of neodymium-doped silica glass," *J. Appl. Phys.* **59**, 3430-3436 (1986).
45. B. J. Ainslie, "A review of the fabrication and properties of erbium-doped fibers for optical amplifiers," *J. Lightwave Tech.* **9**, 220-227 (1991).
46. F. Azuel, D. Meichenin, F. Pellé, P. Goldner, "Cooperative luminescence as a defining process for RE-ions clustering in glasses and crystals," *Opt. Mat.* **4**, 35-41 (1994).
47. J. J. Koponen, M. J. Söderlund, S. K. T. Tammela, H. Po, "Photodarkening in ytterbium-doped silica fibers," *Proc. SPIE* **5990**, 599008 (2005).
48. S. Yoo, C. Basu, A. J. Boyland, C. Sones, J. Nilsson, J. K. Sahu, D. Payne, "Photodarkening in Yb-doped aluminosilicate fibers induced by 488 nm irradiation," *Opt. Lett.* **32**, 1626-1628 (2007).
49. L. B. Glebov, "Linear and nonlinear photoionization of silicate glasses," *Glasstech. Ber. Glass Sci. Technol.* **75**, 1-6 (2002).
50. T. Kitabayashi, M. Ikeda, M. Nakai, T. Sakai, K. Himeno, K. Ohashi, "population inversion factor dependence of photodarkening of Yb-doped fibers and its suppression by highly aluminum doping," in *Optical Fiber Communication Conference*, OSA Technical Digest, paper OThC5, (2006).

51. K. E. Mattsson, "Photo darkening of ytterbium fiber lasers and amplifiers," in *Conference on Lasers and Electro-Optics*, paper CMGG1, (2010).
52. F. Auzel, P. Goldner, "Towards rare-earth clustering control in doped glasses," *Opt. Mat.* **16**, 93-103 (2001).
53. H. Kogelnik, C. K. N. Patel, "Mode suppression and single frequency operation in gaseous optical masers," *Proc. IRE (Correspondence)* **50**, 2365-2366 (1962).
54. E. I. Gordon, A. D. White, "Single frequency gas lasers at 6328 Å," *Proc. IEEE* **52**, 206-207 (1964).
55. J. R. Leger, J. Nilsson, J. P. Huignard, A. P. Napartovich, T. M. Shay A. Shirakawa, "Laser beam combining and fiber laser systems," *IEEE J. Sel. Top. Quantum Electron.* **15**, 237-239 (2009).
56. E. Rochat, K. Haroud, R. Dändliker, "High-power Nd-doped fiber amplifier for coherent intersatellite links," *IEEE J. Quantum Electron.* **35**, 1419-1423 (1999).
57. D. Kracht, R. Wilhelm, M. Frede, C. Fallnich, F. Seifert, B. Willke, K. Danzmann, "High power single-frequency laser for gravitational wave detection," in *Advanced Solid-State Photonics*, OSA Technical Digest, paper WE1, (2006).
58. S. Höfer, A. Liem, J. Limpert, H. Zellmer, A. Tünnermann, S. Unger, S. Jetschke, H.-R. Müller, I. Freitag, "Single-frequency master-oscillator fiber power amplifier system emitting 20 W of power," *Opt. Lett.* **26**, 1326-1328 (2001).
59. T. J. Kane, R. L. Byer, "Monolithic, unidirectional single-mode Nd:YAG ring laser," *Opt. Lett.* **10**, 65-67 (1985).
60. A. Liem, J. Limpert, H. Zellmer, A. Tünnermann, "100-W single-frequency master-oscillator fiber power amplifier," *Opt. Lett.* **28**, 1537-1539 (2003).
61. R. W. Boyd, *Nonlinear Optics* (Academic Press 1992).
62. C. Wirth, T. Schreiber, M. Rekas, I. Tsybin, T. Peschel, R. Eberhardt, A. Tünnermann, "High-power linear-polarized narrow linewidth photonic crystal fiber amplifier," *Proc. SPIE* **7580**, 75801H (2010).
63. J. Edgecumbe, D. Björk, J. Galipeau, G. Boivin, S. Christensen, B. Samson, K. Tankala, "Monolithic, turn-key, 1-kW Yb-doped fiber master oscillator power amplifier," in *Solid State and Diode Laser Technology Review*, 193-199 (2008).
64. J. P. Koplow, D.A.V. Kliner, L. Goldberg, "Single-mode operation of a coiled multimode fiber amplifier," *Opt. Lett.* **25**, 442-444 (2000).
65. J. M. Fini, "Bend-resistant design of conventional and microstructured fibers with very large mode area," *Opt. Express* **14**, 69-81 (2006).
66. B.G. Ward, C. Robin, M. Culpepper, "Photonic crystal fiber designs for power scaling of single polarization amplifiers," *Proc. SPIE* **6453**, 645307 (2007).
67. M-J. Li, X. Chen, A. Liu, S. Gray, J. Wang, D. T. Walton, L. A. Zenteno, "Effective area limit for large mode area laser fibers," in *Optical Fiber Communication Conference (OFC)*, OSA Technical Digest, paper OTuJ2, (2008).

68. J. Limpert, O. Schmidt, J. Rothhardt, F. Röser, T. Schreiber, A. Tünnermann, "Extended single-mode photonic crystal fiber lasers," *Opt. Express* **14**, 2715-2720 (2006).
69. J. Limpert, A. Liem, M. Reich, T. Schreiber, S. Nolte, H. Zellmer, A. Tünnermann, J. Broeng, A. Petersson, C. Jakobsen, "Low-nonlinearity single-transverse-mode ytterbium-doped photonic crystal fiber amplifier," *Opt. Express* **12**, 1313-1319 (2004).
70. J. Pelous, R. Vacher, "Thermal Brillouin scattering measurements of attenuation of longitudinal hypersounds in fused quartz from 77 to 300 K," *Solid State Comm.* **16**, 279-283 (1978).
71. V. I. Kovalev, R. G. Harrison, "Suppression of stimulated Brillouin scattering in high-power single-frequency fiber amplifiers," *Opt. Lett.* **31**, 161-163 (2006).
72. C. Robin, I. Dajani, C. Vergien, C. Zeringue, T. M. Shay, "Experimental and theoretical studies of single frequency PCF amplifier with output of 400 W," *Proc. SPIE* **7580**, 75801I (2010).
73. T. Horiguchi, T. Kurashima, M. Tateda, "Tensile strain dependence of Brillouin frequency shift in silica optical fibers," *IEEE Photon. Tech. Lett.* **1**, 107-108 (1989).
74. J. E. Rothenberg, P. A. Thielen, M. Wickham, C. P. Asman, "Suppression of stimulated Brillouin scattering in single-frequency multi-kilowatt fiber amplifiers," *Proc. SPIE* **6873**, 68730O (2008).
75. I. Dajani, C. Zeringue, T. M. Shay, "Investigation of nonlinear effects in multitone-driven narrow linewidth high-power amplifiers," *IEEE J. Sel. Top. Quantum Electron.* **15**, 406-414 (2009).
76. C. Zeringue, C. Vergien, I. Dajani, "Pump-limited, 203 W, single-frequency monolithic fiber amplifier based on laser gain competition," *Opt. Lett.* **36**, 618-620 (2011).
77. B. Ward, J. Spring, "Finite element analysis of Brillouin gain in SBS-suppressing optical fibers with non-uniform acoustic velocity profiles," *Opt. Express* **17**, 15685-15699 (2009).
78. R. H. Stolen, "Polarization effects in fiber Raman and Brillouin lasers," *IEEE J. of Quantum Electron.* **QE-15**, 1157-1160 (1979).
79. N. Shibata, R. G. Waarts, R. P. Braun, "Brillouin-gain spectra for single-mode fibers having pure-silica, GeO₂-doped, and P₂O₅-doped cores," *Opt. Lett.* **12**, 269-271 (1987).
80. N. Shibata, K. Okamoto, Y. Azuma, "Longitudinal acoustic modes and Brillouin-gain spectra for GeO₂-doped-core single-mode fibers," *J. Opt. Soc. Am. B* **6**, 1167-1174 (1989).
81. P. D. Dragic, C-H. Liu, G. C. Papen, A. Galvanauskas, "Optical fiber with an acoustic guiding layer for stimulated Brillouin scattering suppression," in *Conference on Lasers and Electro-Optics (CLEO)*, OSA Technical Digest, paper CThZ3, (2005).
82. M-J. Li, X. Chen, J. Wang, S. Gray, A. Liu, J. A. Demeritt, A. B. Ruffin, A. M. Crowley, D. T. Walton, L. A. Zenteno, "Al/Ge co-doped large mode area fiber with high SBS threshold," *Opt. Express* **15**, 8290-8299 (2007).
83. S. Gray, A. Liu, D. T. Walton, J. Wang, M-J. Li, X. Chen, A. B. Ruffin, J. A. DeMeritt, L. A. Zenteno, "502 Watt, single transverse mode, narrow linewidth, bidirectionally pumped Yb-doped fiber amplifier," *Opt. Express* **15**, 17044-17050 (2007).
84. D. Walton, S. Gray, J. Wang, M-J. Li, X. Chen, A. Liu, L. Zenteno, A. Crowley, "Kilowatt-level, narrow- linewidth capable fibers and lasers," *Proc. SPIE* **6453**, 645314 (2007).

85. M. D. Mermelstein, M. J. Andrejco, J. Fini, A. Yablon, C. Headley, D. J. DiGiovanni, "11.2 SBS gain suppression in a large mode area yb-doped optical fiber," Proc. SPIE **6873**, 68730N (2008).
86. Y. Jeong, J. Nilsson, J. K. Sahu, D. B. S. Soh, C. Alegria, P. Dupriez, C. A. Codemard, D. N. Payne, R. Horley, L. M. B. Hickey, L. Wanzcyk, C. E. Chryssou, J. A. Alvarez-Chavez, P. W. Turner, "single-frequency, single-mode, plane-polarized ytterbium-doped fiber master oscillator power amplifier source with 264 W of output power," Opt. Lett. **30**, 459-461 (2005).
87. C. Robin, I. Dajani, F. Chiragh, "Experimental studies of segmented acoustically tailored photonic crystal fiber amplifier with 494 W single-frequency output," Proc. SPIE **7914**, 79140B (2011).
88. Y. Jeong, J. Nilsson, J. K. Sahu, D. N. Payne, R. Horley, L. M. B. Hickey, P. W. Turner, "Power scaling of single-frequency ytterbium-doped fiber master-oscillator power-amplifier sources up to 500 W," IEEE J. Sel. Top. Quantum Electron. **13**, 546-551 (2007).
89. I. Dajani, C. Vergien, C. Robin, C. Zeringue, "Experimental and theoretical investigations of photonic crystal fiber amplifier with 260 W output," Opt. Express **17**, 24317-24333 (2009).
90. P. C. Becker, N. A. Olsson, J. R. Simpson, *Erbium-doped fiber amplifiers: Fundamentals and Technology* Academic Press, (2001).
91. R. G. Smith, "Optical power handling capacity of low loss optical fibers as determined by stimulated Raman and Brillouin scattering," Appl. Opt. **11**, 2489-2494 (1972).
92. C. T. Hsu, P. Cheng, K. W. Wong, "A lumped-parameter model for stagnant thermal conductivity of spatially periodic porous media," J. Heat Transfer **117**, 264-269 (1995).
93. D. J. DiGiovanni, "Fabrication of rare earth doped optical fiber," Proc. SPIE **1373**, 2-8 (1990).
94. <http://www.nktphotonics.com/>
95. A. E. Siegman, "New developments in laser resonators," Proc. SPIE **1224**, 2-14 (1990).
96. J. B. Spring, T. H. Russell, T. M. Shay, R. W. Berdine, A. D. Sanchez, B. G. Ward, W. B. Roh, "Comparison of stimulated Brillouin scattering thresholds and spectra in non-polarization-maintaining and polarization-maintaining passive fibers," Proc. SPIE **5709**, 147-156 (2005).
97. A. A. Hardy, R. Oron, "Amplified spontaneous emission and Rayleigh backscattering in strongly pumped fiber amplifiers," J. Lightwave Tech. **16**, 1865-1873 (1998).
98. D. Baney, W. Sorin, "High resolution optical frequency analysis," in *Fiber Optic Test and Measurement*, edited by D. Derickson (Prentice-Hall, 1998).
99. M. Hildebrandt, S. Büsche, P. Weßels, M. Frede, D. Kracht, "Brillouin scattering in high power single-frequency ytterbium doped fiber amplifiers," Opt. Express **16**, 15970-15979 (2008).
100. G. P. Agrawal, *Nonlinear Optics*, Third Edition, Academic Press (2001).
101. D. Cotter, "Observation of stimulated Brillouin scattering in low-loss silica fibre at 1.3 μm ," Electron. Lett. **18**, 495-496 (1982).

102. R. G. Waarts, R. P. Braun, "Crosstalk due to stimulated Brillouin scattering in Monomode fibre," *Electron. Lett.* **21**, 1114-1115 (1985).
103. M. Niklès, L. Thévenaz, P. A. Robert, "Brillouin gain spectrum characterization in single-mode optical fibers," *J. Lightwave Tech.* **15**, 1842-1851 (1997).
104. V. Lanticq, S. Jiang, R. Gabet, Y. Jaouën, F. Taillade, B. Moreau, G. P. Agrawal, "Self-referenced and single-ended method to measure Brillouin gain in monomode optical fibers," *Opt. Lett.* **34**, 1018-1020 (2009).
105. JDS Uniphase, *Diode-Pumped Nd:YAG Non-Planar Ring Laser*, Users Manual, (2008).
106. P. Dainese, P. St. Russel, N. Joly, J. C. Knight, G. S. Wiederhecker, H. L. Fragnito, V. Laude, A. Khelif, "Stimulated Brillouin scattering from multi-GHz-guided acoustic phonons in nanostructured photonic crystal fibers," *Nat. Phys.* **2**, 388-392 (2006).
107. J. C. Beugnot, T. Sylvestre, D. Alasia, H. Maillotte, V. Laude, A. Monteville, L. Provino, N. Traynor, S. F. Mafang, L. Thévenaz, "Complete experimental characterization of stimulated Brillouin scattering in photonic crystal fiber," *Opt. Express* **15**, 15517-15522 (2007).
108. K. Furusawa, Z. Yusoff, F. Poletti, T. M. Monro, N. G. R. Broderick, D. J. Richardson, "Brillouin characterization of holey optical fibers," *Opt. Lett.* **31**, 2541-2543 (2006).
109. L. Dong, "Formulation of a complex mode solver for arbitrary circular acoustic waveguides," *J. Lightwave Tech.* **28**, 3162-3175 (2010).
110. I. Dajani, C. Zeringue, T. J. Bronder, T. Shay, A. Gavrielides, C. Robin, "A theoretical treatment of two approaches to SBS mitigation with two-tone amplification," *Opt. Express* **16**, 14233-14247 (2008).
111. R. W. Boyd, K. Rzążewski, "Noise initiation of stimulated Brillouin scattering," *Phys. Rev. A* **42**, 5514-5521 (1990).
112. T. Eidam, S. Hanf, E. Seise, T. V. Andersen, T. Gabler, C. Wirth, T. Schreiber, J. Limpert, A. Tünnermann, "Femtosecond fiber CPA system emitting 830 W average output power," *Opt. Lett.* **15**, 94-96 (2010).